GLOBAL PERSPECTIVES ON THE PLANE-PARALLEL NATURE OF OCEANIC WATER CLOUDS USING DATA SYNERGY FROM MISR AND MODIS

BY

LUSHENG LIANG

DISSERTATION

Submitted in partial fulfillment of the requirements
for the degree of Doctor of Philosophy in Atmospheric Sciences
in the Graduate College of the
University of Illinois at Urbana-Champaign, 2009

Urbana, Illinois

Doctoral Committee:

Associate Professor Larry Di Girolamo, Chair
Professor Robert Rauber
Professor Greg McFarquhar
Assistant Professor Steve Nesbitt

ABSTRACT

The plane-parallel assumption is commonly used for solving radiative transfer problems in weather and climate research. While a plethora of observational and three-dimensional (3-D) radiative transfer simulations have revealed many shortcomings in the application of the plane-parallel assumption, less attention has been given to providing a global perspective on these shortcomings from observations. This thesis provides this perspective for oceanic water clouds based on data synergy from the Multiangle Imaging SpectroRadiometer (MISR) and the Moderate Resolution Imaging Spectroradiometer (MODIS). Eight years of data for the months of January and July were examined to determine (1) the angular anisotropy in the upwelling radiation captured by multi-angle observations and its departure from plane-parallel expectations, quantified by cloud view-angle consistency, and (2) the viewing zenith angle (VZA) dependence of plane-parallel retrieved cloud optical thickness (τ).

Cloud view-angle consistencies, relative to their plane-parallel expectations, were defined in bidirectional reflectance factor (BRF), cloud optical thickness and spherical albedo metrics. The probability distribution functions of these metrics reveal that clouds are angularly consistent in BRF, cloud optical thickness and spherical albedo to within 5% of their plane-parallel value 67.6%, 23.0%, and 72.0% of the time, respectively, for January and 61.0%, 23.7%, and 61.3% of the time, respectively, for July. Global maps of these metrics show large spatial variability and solar zenith angle (SZA) dependence, with stratiform regions being more plane-parallel like than cumuliform regions and stratiform regions being less plane-parallel-like when the SZA is greater than 60º. We establish a relationship between the cloud view-angle consistency metrics and a cloud

spatial heterogeneity metric (H_σ) that allows us to potentially identify, with a prescribed confidence level, which MODIS microphysical retrievals meet the plane-parallel assumption to within any desired range in view-angle consistency. For example, requiring 96% of the MODIS cloud microphysical retrievals to be angularly consistent in τ to within 15% of their plane-parallel value (i.e., optical thickness metric values < 15%) suggests performing retrievals only where $H_\sigma < 0.072$; 22.1% of the domains met this criterion.

The cloud view-angle consistency is further examined by the view-angle dependence of plane-parallel retrieved τ. With the unique near-simultaneous multiangle observations from MISR, we are able to overcome many shortcomings in previous observational studies on τ-VZA relationships derived from wide-swath, single-view scanning instruments. Unlike previous studies, we are able to exclude cloud seasonal and latitudinal invariant assumptions, eliminate inconsistency in cloudy scene identification across multiple view-angles and minimize the impact of pixel expansion with viewing obliquity on τ retrievals. Our analysis qualitatively confirms many τ-VZA relationships found in previous studies, while able to characterize these relationships regionally over the globe. However, quantitative comparisons are hard to interpret, given many variables that the bias in plane-parallel retrieved τ depends on, and the different sampling characteristics of the various dataset. Our results show that, under oblique Sun, for example, τ is biased low relative to nadir in the mean by 73% at a VZA = 70.5º in the forward-scatter directions at 47.5ºS-50ºS latitude (SZA = 75º) in July, and τ is substantially biased high in the backscatter directions only for VZA = 70.5º, with a bias as high as 83%.

Examining our data for large SZAs (SZA > 68º in January and SZA > 73º in July) and up to VZA = 70.5°, and stratifying the analysis by nadir-τ and cloud spatial heterogeneity, reveal additional complexities not observed before. When VZA = 70.5º, τ is biased higher than nadir in both forward-scatter and backscatter directions even under high Sun (SZA < 40° in both January and July). Under very low Sun (SZA > 68° in January and SZA > 73° in July) and in the forward-scatter direction, optically thinner clouds and heterogeneous clouds are less negatively biased or even positively biased at small VZAs as compared to optically thicker clouds and homogeneous clouds, resulting in a slight τ peak at VZA = 26° when averaged over all clouds. Additionally, stratifying the data by nadir-τ reveals additional 3-D and non-3-D radiative transfer effects that determine the τ-VZA relationships. We demonstrated that to understand the complexity in the τ-VZA relationships requires carefully considering (1) the various 3-D radiative transfer pathways, (2) the increased viewing of more cloud-sides with viewing obliquity, (3) the relative azimuth angle between sun and view, (4) the change in concavity of the radiance-τ non-linear relationship with view-angle, and (5) other non-3-D radiative transfer effects, such as sunglint.

Given that a large fraction of water clouds are not plane-parallel to within any reasonable degree in view-angle consistency, and given the great complexity in which the bias in plane-parallel retrieved τ depends on sun-view geometry and other factors, we call to the research community to develop new retrieval paradigms for cloud microphysical properties that can properly account for the 3-D radiative transfer found in nature.

ACKNOWLEDGMENTS

My deepest gratitude is to my advisor, Professor Larry Di Girolamo, for his indispensable and insightful guidance, continuous encouragement and everlasting patience throughout my Ph.D. study and research. His never-ending enthusiasm, meticulous attitude toward the research work, and second-to-none excellence toward scientific achievement have kept me motivated for the last seven years. He reminded me to occasionally look ahead beyond pursuing 99.999% perfectness, given that the conclusions would remain unchanged. All these will certainly be carried on to my research and life in the future. I especially would like to express my deepest thanks to him for his patience in teaching me how to write a good paper and for his care in reading, commenting and all the hard work he put into helping me finish this thesis. For everything you have done for me, Dr. Di Girolamo, I thank you.

I would like to thank Professors Robert Rauber, Greg McFarquhar and Steve Nesbitt for serving on my thesis committee and their comments and critics of my research. Many thanks go to many officemates, especially Guangyu Zhao, Yuekui Yang, Mike Wilson and Eric Snodgrass for their joyful and colorful friendship. Special acknowledgments are extended to Dr. Steven Platnick for providing the MODIS one-dimensional plane-parallel radiative transfer model and Dr. Frank Evans for providing the Mie scattering calculation code.

I would like to acknowledge the NASA Earth and Space Science Fellowship program for granting me a three-year research fellowship between 2005 and 2008. Additional support from the MISR project through the Jet Propulsion Laboratory of the

California Institute of Technology is also gratefully acknowledged. In addition, the MISR data were obtained from NASA Langley Research Center Atmospheric Sciences Data Center. The MODIS data were obtained through the Level 1 and Atmosphere Archive and Distribution System of NASA Goddard Space Flight Center.

Finally, my deepest gratitude goes to my parents for their endless and greatest support throughout my life.

TABLE OF CONTENTS

CHAPTER 1: INTRODUCTION

1.1 Motivation

Clouds, covering ~70% of the globe, play important roles in the Earth's climate system by regulating the hydrological, dynamical and radiative processes. A consensus has long been reached that the role of clouds remains a major source of uncertainty in the projections of future climates [e.g., *Colman,* 2003; *Potter and Cess*, 2004; *Solomon et al.* 2007]. To reduce the uncertainty, a better understanding of cloud processes and properties over all scales is required.

The problems relating to the radiative transfer through clouds can be classified into two categories: inverse problem and forward problem. Within the scope of this thesis, the inverse problem is to infer cloud optical properties, such as cloud optical thickness (τ) and effective radii (r_e) of the cloud drop size distribution, using visible to near-infrared radiance measurements from satellites. The forward problem is to calculate radiance fields given cloud optical properties. Undoubtedly, a well-established measurement of cloud microphysical properties, at least in terms of their accuracies, is critical to climate research. For example, it can be used to monitor long-term climate changes, to evaluate and improve cloud parameterization in Global Climate Models (GCMs), to validate model performances, and to assess cloud feedbacks due to changes in other key climate variables such as cloud radiative susceptibilities to droplet number perturbations [*Platnick and Oreopoulos,* 2008; *Oreopoulos and Platnick,* 2008]. It is equally important to accurately compute radiative transfer from retrieved cloud optical

properties [*e.g., Rossow et al.,* 2002*, Rossow and Zhang,* 1995*; Zhang et al*., 2004] or from diagnostic variables produced by GCMs to further compute radiative heating rates.

However, producing accurate solutions to the inverse and forward problem is challenging because clouds in nature are heterogeneous in both horizontal and vertical directions over a wide range of time and space scales [*Rossow and Cairns*, 1995]. The key challenge lies in the continued, ubiquitous application of one-dimensional (1-D) radiative transfer theory, often referred to as the plane-parallel assumption, whereby cloud optical properties are assumed to be homogenous in the horizontal direction within vertically finite layers, but can vary in the vertical direction. Such simplification reduces radiative transfer from 3-D to 1-D so that inverse problems are solvable and forward radiative transfer calculations are computationally fast using numerical techniques (e.g., discrete ordinate method and adding-doubling method) or analytical solutions (e.g., two-stream method). However, a simple look at clouds, either from the surface, aircraft or spacecraft, reveals that they are by no means plane-parallel homogeneous.

Numerous studies have demonstrated that the plane-parallel assumption for solving both inverse and forward problems is problematic for real clouds [*e.g., Kobayashi,* 1993; *Loeb and Davies,* 1996, 1997; *Di Girolamo et al.,* 1998; *Loeb and Coakley,* 1998; *Fu et al.,* 2000; *Genkova and Davies,* 2003; *Horvath and Davies,* 2004; *Kato et al.,* 2006; *Kato and Marshak,* 2009]. However, the following questions remain: **how often and to what degree is the plane-parallel assumption valid for any given application requirement for real clouds from regional to global scales? Is there a way to identify cloud heterogeneity conditions under which the valid application of the plane-parallel assumption occurs?** One of the goals of this thesis is to address these

two questions via detailed examination of cloud angular anisotropy in the upwelling radiation observed by the Multi-angle Imaging SpectroRadiometer (MISR) [*Diner et al.,* 1998].

It will be shown in this thesis that a large fraction of water clouds are not valid for the application of the plane-parallel assumption over a large fraction of ocean (Chapter 4). Many studies have long revealed that inferring τ of heterogeneous clouds from satellite measurements of reflected solar radiation with the plane-parallel assumption carry systematic errors that depend on both solar and view geometries [e.g., *Kobayashi,* 1993; *Loeb and Davies,* 1996, 1997; *Loeb and Coakley,* 1998; *Zuidema and Evans,* 1998; *Kato et al.,* 2006; *Kato and Marshak,* 2009]. However, our knowledge of this issue over the globe is still very limited. With multi-angle observations of clouds from MISR, two questions can be asked: **how will 1-D retrieved τ change with view-angle over the globe and how does it vary with cloud properties, such as thickness and heterogeneity, and what new knowledge can we learn from such multi-angle observations over what we have learned from observations by conventional wide-swath, single-view scanning instruments?** Such knowledge obtained here may help eliminate any view-angle-induced retrieval bias in the future, not only in τ, but also in other products that depend on it, such as albedo and liquid water path.

Motivated by answering these questions, two objectives are established and elaborated below along with original contributions.

1.2 Objectives with Background Information

1.2.1 Plane-parallel Nature of Oceanic Water Clouds

The first objective of this thesis is to examine how often and to what degree the plane-parallel assumption for oceanic water clouds is valid for any given application requirement over the globe, as well as to find a way to identify cloud heterogeneity conditions under which this occurs.

The valid use of the plane-parallel assumption can be examined from aspects of the inverse problem. Using the retrieval of τ as an example, numerous studies have shown that 1-D retrieved τ is a function of sun-view geometry, but it should be independent of sun-view geometry. As demonstrated by 3-D radiative transfer model simulations [*e.g., Kobayashi,* 1993; *Zuidema and Evans*, 1998; *Kato et al.,* 2006; *Kato and Marshak,* 2009], τ at nadir for horizontally heterogeneous clouds is biased low for overhead Sun. The negative bias is mitigated or even a positive bias appears when the Sun elevation becomes lower, as revealed by observational studies [*e.g., Loeb and Davies,* 1996] and model simulations [*Zuidema and Evans*, 1998; *Várnai and Davies,* 1999; *Kato et al.,* 2006]. Moreover, clouds could appear either thicker or thinner in both backscatter and forward-scatter directions for low Sun [*Kobayashi, 1993*; *Loeb and Coakley*, 1998; *Kato et al.,* 2006; *Várnai and Marshak,* 2007; *Kato and Marshak*, 2009], which could be attributed to the difference in relative azimuth angle (RAZ) among the observational studies [e.g., *Loeb and Coakley*, 1998; *Várnai and Marshak,* 2007] or to the large variations arising from simulating only a few cloud scenes [*Kato et al.,* 2006]. Besides depending on sun-view geometry, the biases of retrieved τ also depend on cloud

optical thickness, internal heterogeneity and external heterogeneity [*Loeb and Várnai,* 1997; *Várnai and Davies,* 1999; *Várnai*, 2000].

The valid use of the plane-parallel assumption can also be examined from the aspect of the forward problem. Such examinations have to be on the basis of a "known" cloud field, which can be specified from cloud models or observations. Usually, radiative fluxes or cloud albedos calculated with 1-D radiative transfer models on the "known" cloud field are evaluated directly against 2-D/3-D radiative transfer model calculations that are taken to be the truth [*e.g., Cahalan, et al.,* 1994; *Barker*, 1996; *O'Hirok and Gautier,* 1997; *Zuidema and Evans*, 1998; *Fu et al*., 2000; *Cole et al*., 2005]. Alternatively, to mimic 1-D radiative transfer calculations with satellite retrievals, 1-D calculations are obtained from 1-D retrieved cloud optical properties based on simulated 3-D radiative fields [*e.g., Kato et al*., 2006]. For the purpose of evaluating the plane-parallel assumption in GCMs, domain averages are used for compassion with a domain size comparable to that of GCM grids. Three key findings are summarized as follows:

(1) Generally, 1-D radiative transfer calculations are accurate for stratiform clouds, but not for cumuliform clouds;

(2) The albedo or flux biases depend on solar zenith angle (SZA): negative biases (1-D calculation minus 2-D/3-D calculations) are found for overhead Sun; bias magnitudes are reduced when the Sun becomes oblique; and biases could be positive when the SZA is very large;

(3) No consensus was reached regarding bias magnitude. It ranges from marginal to severe depending on cloud fields simulated and other assumptions used, e.g., domain

size (several hundred to a few kilometers), cloud resolution (couple of tens of meters to several kilometers), SZA, etc.

Despite much knowledge gained in the valid use of the plane-parallel assumption, we must be aware of some weaknesses:

(1) Only a handful of observational studies have been conducted for evaluating 1-D radiative transfer theory on certain cloud types over specific areas and all results were derived from observations of wide-swath, single-view scanning instruments. Some uncertainties arising from several intrinsic assumptions and limitations of these instruments undermine the extraction of true retrieval biases that depend on such factors as sun-view geometries, thickness of clouds and cloud-top heterogeneity. Clearly, this lowers our confidence in the evaluation of the plane-parallel assumption due to the limitations of the instruments. In Chapter 5, we will discuss these assumptions and limitations in detail;

(2) Model simulations for evaluating the plane-parallel assumption were based on a very limited number of cloudy scenes; they are not globally representative. We continue to face two difficulties to reach our global perspective: (1) we need to know the true 3-D cloud properties globally, which we do not have; and (2) it is still not feasible to perform expensive 3-D radiative transfer simulations on spatially resolved cloud properties on the globe scale at high resolution, say, few tens of meters, owing to the enormous computational demands.

These limitations all point to the fact that we continue to lack a global perspective of the applicability of the plane-parallel assumption for clouds. The only reasonable way to gain such knowledge is through satellite observations. As we lack a globally

representative dataset of true cloud optical properties, we must seek alternative ways to reach our global perspective.

Two notable attempts were made to reach this perspective. *Genkova and Davies* [2003] examined the spatial heterogeneity of the MISR red band (677 nm) bidirectional reflectance factor (BRF) at a given view direction and concluded that only a small fraction of clouds were homogeneous below a spatial BRF contrast threshold. But, the following question remained: how smooth in cloud BRF is "good enough" for the application of the plane-parallel assumption? *Horvath and Davies* [2004] constructed a view-angle consistency test and found that ~30% of cloudy pixels at 3.3 km resolution had 1-D radiative transfer modeled radiances to agree within ±5% of MISR observed radiances for all MISR view-angles. However, there was no tie to cloud spatial heterogeneity of the scene and SZA, and only one threshold (5%) was used to separate plane-parallel clouds from the non-plane-parallel clouds regardless of applications. In addition, their results are far from globally representative since only a few days of observations were used and no regional context was provided.

In this thesis (Chapter 3 and 4), we extended the approach of *Horvath and Davies* [2004] and examined angular anisotropy in the upwelling radiation of oceanic water clouds observed by MISR. Three view-angle consistency metrics were developed to quantify the angular anisotropy of clouds, namely, the departures of 1-D simulated BRFs from observed BRFs at cloud-tops and variations in 1-D retrieved cloud optical thickness and cloud spherical albedo across MISR multiple view-angles. The examination was performed over the globe based on cloud observations for the months of January and July

between 2001 and 2008. Three main **original contributions** are briefly summarized as follows:

(1) For the first time, the probability distribution functions of view-angle consistency relative to plane-parallel in the upwelling radiation were derived from globally representative observations;

(2) The regional distributions over the globe of the cloud view-angle consistency were presented for the first time, representing the regional distributions of the applicability of the plane-parallel assumption. Global maps of cloud view-angle consistency occurrences showed large spatial variability and SZA dependence. A large fraction of oceanic water clouds over a large fraction of the ocean are not valid for the application of the plane parallel assumption by any reasonable criterion, thus lowering our confidence in the application of the plane-parallel assumption in remote sensing and climate modeling. As such, over regions where the plane-parallel assumption is likely not applicable, care must be taken to solve both inverse and forward radiative problems by special treatment of 3-D radiative transfer effects and to properly interpret the existing scientific results that were derived with the plane-parallel assumption.

(3) We related the view-angle consistency to the cloud spatial heterogeneity, which allows us to potentially identify, with a prescribed confidence level, which microphysical retrieval and associated retrieval uncertainty by the Moderate Resolution Imaging Spectroradiometer (MODIS) within the MISR swath meet the plane-parallel assumption to within any desired range in view-angle consistency.

1.2.2 Viewing Zenith Angle Dependence of Oceanic Water Cloud Optical Thickness

The second objective of this thesis is to provide the most comprehensive and reliable estimation of viewing zenith angle (VZA) dependence of 1-D retrieved τ under various SZAs, RAZ, cloud thickness, and cloud heterogeneity with a globally representative dataset.

The knowledge of VZA dependence of τ on a global scale can not be obtained from model simulations, simply because of the computational constraints and the lack of a globally representative true cloud dataset. The only way to gain such knowledge is from satellite observations. Only two studies with satellite observations are available.

Loeb and Coakley [1998] examined the Advanced Very High Resolution Radiometer (AVHRR) observations of marine stratus off the coasts of California, Peru, and Angola. They showed that while 1-D inferred τ was less sensitive to VZA in backscatter directions, an appreciable VZA dependence of τ was found in forward-scatter directions, with a decreasing mean τ with viewing obliquity by as much as 40% for $\mathrm{VZA} \approx 60^\circ$ as compared to that at nadir. These VZA dependences were later attributed to sub-pixel geometrical heterogeneity at cloud-tops [*Loeb et al.,* 1998]. *Várnai and Marshak* [2007] examined one year of globally retrieved τ from MODIS and found that the mean τ increases as VZA increases in both forward-scatter and backscatter directions. The authors proposed that 3-D radiative transfer effects, viewing of cloud-sides, and MODIS observing clouds predominantly from near-side-scatter directions. Why these two studies do not agree is not fully understood.

Common to these two studies is the use of "sun-synchronous", "single-view" scanning satellite instruments. However, uncertainties arising from some intrinsic assumptions and limitations of "sun-synchronous" and "single-view" prevent us from obtaining a true τ-VZA and, thus, limiting the usefulness of these results.

One of the limitations in using "single-view" instruments lies in that cloudy scenes identified across multiple view-angles are not consistent in their properties. "Single-view" means that a cloud scene can only be observed once from a given view-angle at a time. As a result, comparing mean τ for cloudy scenes for one view-angle to that for another view-angle implicitly requires that the two sets of cloudy scenes are the same. However, this is not true. For example, a partially cloudy scene identified in the nadir direction could be identified in an oblique direction as a fully cloudy scene, as suggested by the fact that cloud fraction increases with VZA [*Minnis,* 1989; *Zhao and Di Girolamo,* 2004]. Another limitation of using "single-view" instruments lies in that the pixel's Ground Instantaneous Field of View (GIFOV: the area covered by a pixel) of a single-view instrument expands with viewing obliquity. Given the fact that the magnitude of retrieved τ is a function of pixel size [*e.g., Zuidema and Evans,* 1998*; Várnai and Marshak,* 2001], such pixel expansion impacts the retrieved τ-values as a function of view-angle.

Because 1-D retrieved τ is a function of SZA [*e.g., Loeb and Davies,* 1996], the VZA dependence of τ usually is examined for a specified SZA. When "single-view" meets "sun-synchronous", the cloud latitudinal invariant assumption must be invoked. A "sun-synchronous" satellite always passes a location beneath it on the Earth at the same local time, which implies that the solar geometries of observations in one orbit are nearly

the same to that in another orbit within a short period of time. As discussed further in Chapter 5, the SZA-isolines intersect a large range of latitudes except regions over high latitudes, where they are roughly aligned. Such Sun-Earth-satellite sun-view geometry for a sun-synchronous single-view satellite, such as MODIS, means that for most regions the SZA-binned mean τ for one view-angle and another are derived from clouds over different latitudes. Therefore, τ-VZA obtained in this way is inescapably coupled with natural cloud latitudinal variations in τ. This is also an example of the inconsistency in cloudy-scene sampling across multiple view-angles.

With a sun-precessing satellite instrument, such as Earth Radiation Budget Satellite (ERBS)**,** the cloud latitudinal invariant assumption can be avoided. This is because a sun-precessing satellite, unlike sun-synchronous satellites, has slightly different local equator-crossing time from one orbit to another. Thus, a region on the Earth observed in one viewing direction for a SZA can be observed in a different viewing direction for the same SZA. With one year of ERBS observations, *Loeb and Davies* [1997] examined departures of the observed radiances from 1-D radiative transfer simulated radiances as a function of VZA between 30ºN to 30ºS. Unfortunately, no analysis was performed on τ. Apparently, the analysis with ERBS is also limited by the aforementioned limitations associated with "single-view." Also, it takes a long time to achieve significant sampling for the analysis, thus requiring cloud property invariance over the long time scale.

In this thesis, the SZA-binned VZA dependence of τ was examined with multi-angle observations of clouds from MISR, whereby we were able to overcome many shortcomings in wide-swath, single-view scanning satellite, for the following reasons:

(1) Simultaneous multiangle views of the same scene from MISR allows us to examine the SZA-binned VZA dependence of τ without invoking the cloud seasonal and latitudinal invariant assumption. Examinations can be done for clouds observed at the same time for the same SZA over the same region anywhere over the globe;

(2) The small expansion of MISR pixel GIFOV with viewing obliquity reduces the impact of pixel size expansion with viewing obliquity on developing τ-VZA relationships;

(3) Given the small expansion of MISR pixel GIFOV with viewing obliquity, observing a cloud at multiple view-angles from MISR automatically eliminates errors associated with the inconsistency in cloudy scene identification across multiple view-angles.

In this thesis (Chapter 5), we show results that corroborated many of the observed behaviour of mean τ measurements with sun-view geometry found in previous studies, while revealing additional complexities. Four major **original contributions** are briefly summarized as follows:

(1) Our results provided the most reliable estimation of VZA dependence of 1-D retrieved τ over the globe;

(2) Examining our data for large SZA and VZA and stratifying the analysis by nadir-τ and cloud spatial heterogeneity revealed additional complexities not observed in any existing observational study or model simulation. The cloud angular anisotropy in the upwelling radiation is augmented when clouds are viewed in a very larger VZA even when SZA is high. Under very low Sun, our observed τ-VZA relationships demonstrates

that the τ-VZA relationship depend on RAZ, which when taken into account, explains the differences in τ-VZA relationship amongst various studies;

(3) Stratifying our analysis by nadir-τ revealed additional 3-D and non-3-D radiative transfer effects that determine the behavior of τ as a function of VZA, such as sunglint and inconsistency in cloudy scene identification in wide-swath, single-view scanning instruments.

(4) Extracted from our observations, we demonstrated that the complex dependence of 1-D retrieved τ on sun-view geometry requires considering, at least, (1) various 3-D radiative transfer pathways, (2) the increased viewing of more cloud-sides with viewing obliquity, (3) RAZ between sun and view, (3) the change in concavity of the radiance-τ non-linear relationship with view-angle, and (4) other non-3-D radiative transfer effects, such as sunglint.

CHAPTER 2: DATA FUSION

This chapter describes the Multiangle Imaging SpectroRadiometer (MISR) and the Moderate Resolution Imaging Spectroradiometer (MDOIS) instruments and the dataset used in this thesis, followed by algorithms for fusing cloud observations by MISR and MODIS. The fusion of the observations of a cloud element by MISR and MODIS includes projecting MODIS-retrieved cloud optical thickness (τ), effective radii (r_e) and phase on the MISR grids (Section 2.2); and registering a cloud element at cloud top across all MISR multi-angle camera images to obtain radiances measured by the MISR cameras in multiple view-angles (Section 2.3). Part of the contents of this chapter is extracted from an article of *Liang et al.* [2009] published in *Geophysical Research Letters* and has been modified to maintain the flow of this thesis.

2.1 Instruments and Dataset

MISR, onboard the Terra satellite, provides nine views of the same scene on the Earth within seven minutes from its multi-camera pushbroom design. Details of the instrument and instrument performance are described in *Diner et al.* [1998]. In brief, one camera views at nadir (nominal viewing zenith angle of 0°) and is designated the AN-camera; four cameras, designated AF, BF, CF and DF, point forward along the orbital track at viewing zenith angles of 26.1°, 45.6°, 60.0° and 70.5°, respectively; four other cameras, designated AA, BA, CA, and DA, point aft along the orbital track at viewing zenith angles of 26.1°, 45.6°, 60.0° and 70.5°, respectively. MISR measures radiance in 4

narrow-band spectral channels (446 nm, 556 nm, 667 nm, 866 nm) over a swath of ~400 km and overlaps with the center portion of the MODIS swath. The measured radiances are re-sampled and projected in the predefined Space-Oblique Mercator (SOM) grids on the World Geodetic System 1984 ellipsoid surface by using a distance-weighted averaging algorithm [*Jovanovic et al.,* 1999]. The reported radiances for a grid have a resolution varying from 275 m to 1.1 km, depending on the channel and camera. For 866 nm (near-infrared) radiance, the resolution is 1.1 km for all MISR oblique cameras and 275m for the MISR AN-camera. The radiances for the AN-camera at 1.1 km resolution are just the average of 4×4 275 m radiances. Version 24 of the MISR 866 nm radiances are converted to bidirectional reflectance factors (BRFs) using

$$BRF = \frac{\pi L_{866}}{\cos(SZA) F_0}, \tag{1}$$

where L_{866} is the spectral radiance in the near-infrared band (866 nm) at the top of the atmosphere and F_0 (reported along with MISR radiance measurements) is the solar irradiance corrected to the Sun-Earth distance at the top of the atmosphere.

The sun-view geometries at 17.6 km resolution, including solar zenith/azimuth angles and view zenith/azimuth angles, are linearly interpolated to 1.1 km resolution from Version 13 of the MISR Geometric Parameters product. Only clouds over ocean are considered based on Version 24 of the MISR Ancillary Geographic Product (AGP). The AGP file also provides the latitude and longitude for each 1.1-km pixel. Clouds over sea-ice are removed based on the sea-ice flags in Version 3 of the MISR Terrestrial

Atmosphere and Surface Climatology data. MISR data are available through http://l0dup05.larc.nasa.gov/MISR/cgi-bin/MISR/main.cgi.

MODIS [*Barnes et al.* 1998], also onboard the Terra satellite, measures radiance (MOD02 product) in 36 spectral channels, ranging in wavelength from 0.4 μm to 14.4 μm. MODIS archives the radiance measurements and other derived product into granules. Each granule covers 5-minute measurements over an area with ~2300 km in the cross track direction and ~2000 km in the along-track direction. The ground sampling resolution in near nadir directions ranges from 250 m to 1 km, depending on the spectral channel. The Ground Instantaneous Field of View (GIFOV) of a pixel expands by a factor of ~4.8 in the cross track direction and ~2.0 in the along track direction for VZA=~55º [*Nishihama et al.,* 1997]; within the center portion of the swath that overlaps with the MISR swath, it expands by a factor of ~1.2 in the cross track direction and ~1.1 in the along track direction.

The cloud microphysical properties, τ and r_e (MOD06 product), are retrieved through daytime multi-spectral reflected solar radiances [*Platnick et. al.,* 2003]. Only water clouds are considered in this thesis based on the cloud thermodynamic phase (part of the 1-km pixel-level Quality Assessment in the MOD06 product), which is retrieved through shortwave infrared radiances and cloud-top temperature retrievals and specifically is used for τ and r_e retrieval algorithm [*Platnick et al.,* 2003]. Brightness temperature at the cloud-top is calculated from 11 μm thermal emission (MOD02 product) to characterize the cloud-top height heterogeneity (Chapter 5). All product mentioned above have a ground resolution of 1 km in the near nadir direction. The geodetic locations for 1-km-resolution products, expressed in latitude and longitude on

the Earth ellipsoid surface, are given in the MOD03 product. In conjunction with the MISR latitude and longitude, they are used for projecting MODIS 1-km-resolution products to the MISR SOM grids at 1.1 km resolution on the ellipsoid surface. Collection 5 MODIS products are used in this study and are available through http://ladsweb.nascom.nasa.gov/data/.

Terra is in a sun-synchronous orbit with an equator-crossing time of ~10:30 AM LST. Thus, all results are valid for this time. In Chapter 3, a set of regional cloud observations over the northeastern Pacific from MISR and MODIS was used to test the viability of view-angle consistency to quantify cloud angular anisotropy in the upwelling radiation. In Chapter 4, cloud observations over the globe for the months of January and July between 2001 and 2008 were used to examine the geophysical distributions of cloud angular anisotropy in the upwelling radiation, and the same global data were used to examine the view-angle dependence of τ in Chapter 5.

2.2 Projection of MODIS Product on the MISR SOM Grid

Given a 3×3 1.1-km-pixel domain prescribed in the MISR AN-camera image, we need to know its microphysical properties retrieved from MODIS, which requires projecting the MODIS product at ~1 km resolution on the MISR 1.1 km resolution SOM grid. Because the projection grid and resolution of MODIS are different from that of MISR, a MODIS 1-km pixel will never completely overlap with a MISR 1.1-km pixel, even if both observations are made in nearly the same view geometry (Figure 2.1). Given a 3×3 1.1-km-pixel domain in the MISR grid, if we simply match MODIS pixels using a nearest neighboring algorithm, it is possible that not all 9 matched-pixels would form a

3×3 pixel square, that is, the geophysical integrity is not held. In this thesis, we require that such integrity is maintained. This requirement is met as follows.

1. For each MODIS pixel within the overlapped swath of MODIS and MISR, its best match in the MISR SOM grid is first found with an implementation of the algorithm routines in the General Cartographic Transformation Package [*U.S. Geological Survey, 1993*]. That is, given the SOM grid projection parameters, the registration procedure transfers a MODIS pixel's latitude and longitude (reported in MOD03) to MISR SOM grid coordinates.
2. This matching information equally tells us which MODIS pixel is the best match for a MISR grid. If two or more MODIS pixels point to the same MISR grid, the nearest one to that MISR grid is kept. Given two points on the Earth spherical surface with the latitude and longitude of (ϕ_1, λ_1) and (ϕ_2, λ_2), respectively, the distance between them is given by the Haversine formula:

$$dis. = 2 * R * \arcsin\left(\sqrt{\sin^2\left(\frac{\phi_1 - \phi_2}{2}\right) + \cos\phi_1 \cos\phi_2 \sin^2\left(\frac{\lambda_1 - \lambda_2}{2}\right)}\right), \qquad (2)$$

   where R is the radius of Earth.
3. With the results obtained by following Step 2, for a 3×3 1.1-km-pixel domain in the MISR grid, a 3×3 1-km-pixel domain in a MODIS image matches the domain in the MISR grid if and only if the center pixels of both domains match to each other. As such, each pixel in the domain in the MISR grid matches to one in the

domain in the MODIS image, thus maintaining the geophysical integrity of the data.

The MODIS 866 nm BRF, τ, r_e and cloud phase for a registered domain are obtained, and only fully water cloudy domains having τ and r_e retrievals for all 9 pixels are used in our analysis.

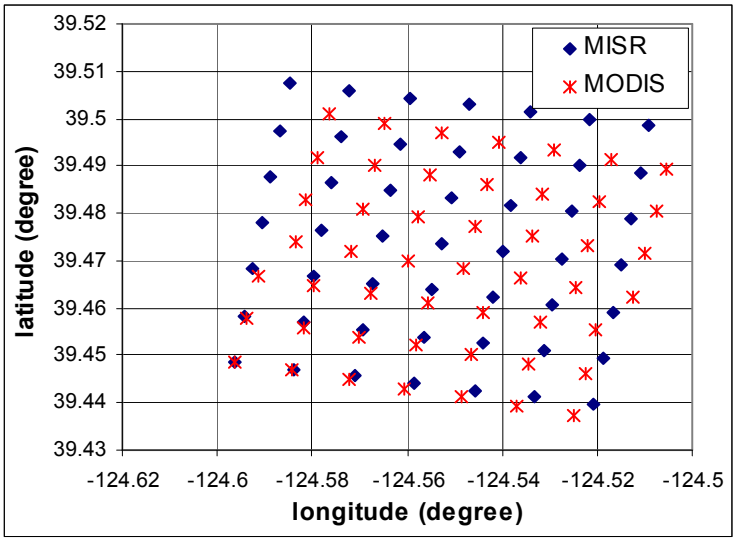

Figure 2.1. *Latitudes and longitudes of a group MODIS 1 km-pixels and MISR 1.1 km-pixels. Markers show the center of each pixel. The data are extracted from MISR block 60, orbit 2118, collected on 11 May, 2005.*

2.3 Registrations in MISR Images

For a fully cloudy water domain successfully identified in the MISR grid, we need to find its radiance measurements in the MISR multiple view-angles. Because MISR observes a cloud element in different viewing directions, it may project the cloud to different SOM grid locations on the Earth ellipsoid surface for different viewing cameras. As illustrated in Figure 2.2, the projected position of the cloud is not the location right beneath the cloud, instead, it refers to the location on the Earth ellipsoid surface by extending the line which connects the satellite and the cloud to the surface. The difference in the projections is often called parallax and is generally a function of view-angles of two cameras, and the altitude and wind vector of cloud. The task here is to find the parallax of a domain between MISR AN-camera image and each oblique-camera image.

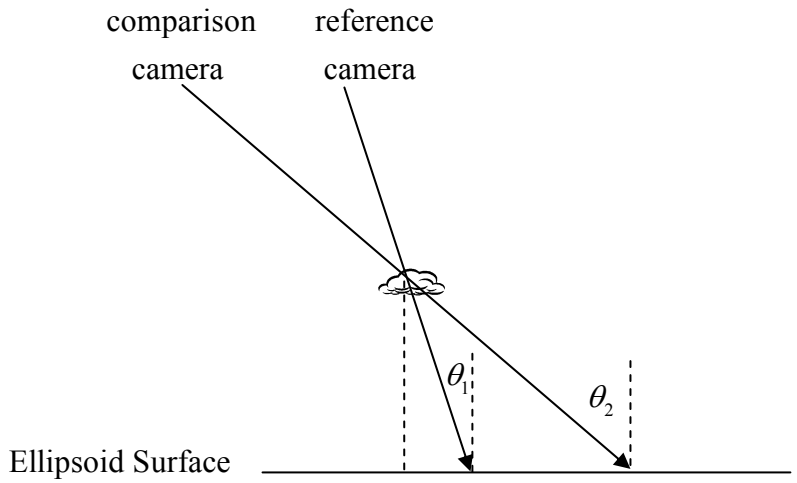

Figure 2.2. *Illustration of projections of a cloud by two MISR cameras on the Ellipsoid surface.*

2.3.1 Pixel-level Registration Technique

Let us first describe the registration technique at the pixel-level (hereafter, referred to as the single-pixel-registration algorithm) that uses the MISR area-matching algorithm M2 [*Muller et al.,* 2002]. The M2 algorithm is one of the MISR operational algorithms used for retrieving cloud-top stereo heights. As compared to ten other stereo matching algorithms [*Diner et al.,* 1999], it is fast, accurate and reliable.

As illustrated in Figure 2.3, given a target pixel (shaded pixel in red) in the reference image (Figure 2.3a), we need to find its best match (shaded pixel in green) somewhere in the comparison image (Figure 2.3b). A target patch (i.e., a pixel patch consisting of 7×11 pixels) centered by the target pixel is prescribed in the reference image. A set of comparison patches (with the same size as that of the target patch) in the comparison image are cut by iterating each pixel in the search window. A S_{M2} metric value is calculated when paring each comparison patch and the target patch. The best matched comparison patch to the target patch is the one with the minimal S_{M2} value and the pixel centered on the comparison patch is registered to the target pixel. The formula to calculate S_{M2} is given as follows, which measures the degree of similarity between two patches with the same size,

$$S_{M2} = \frac{\sum_{i,j} \left| \left[\frac{R_{i,j} - \langle R \rangle}{R_{\max} - R_{\min}} \right] - \left[\frac{C_{i,j} - \langle C \rangle}{C_{\max} - C_{\min}} \right] \right|}{\sigma_{M2}}, \tag{3}$$

where $R_{i,j}$ is the BRF value in the target patch at position (i, j), i and j are the location indexes in the patch, $\langle R \rangle$, $R_{\max}$ and $R_{\min}$ are the mean, maximum and minimum BRF over the patch, and $C_{i,j}$, $\langle C \rangle$, $C_{\max}$ and $C_{\min}$ are the corresponding values for the comparison patch. The calculation of σ_{M2} is given as

$$\sigma_{M2} = \sum_{i,j} \left\| \left[\frac{R_{i,j} - \langle R \rangle}{R_{\max} - R_{\min}} \right] \right\|. \tag{4}$$

A large search window must be set to ensure it contains the best matching pixel for the target pixel. Its size is set by the largest possible cloud-top height, the maximum cloud speed, the cloud motion direction, the satellite speed and moving direction, and view-angles of the comparison and reference cameras. Where to put the search window depends on if the reference camera points more forward or aftward than the reference camera. In the case of the comparison camera pointing "more forward" than the reference camera (Figure 2.4a), if a cloud moves in the same direction as the satellite (Figure 2.5), the parallax in the along track direction, expressed as the number of 1.1-km-pixels, should be less than $U_c + \frac{h_{\max}}{1100m} \left| \tan\theta_2 - \tan\theta_1 \right|$, where U_c is an estimate of the largest travel distance of the cloud. Similar, if the cloud moves in the opposite direction as the satellite, the largest parallax in the along track direction should be less than U_c, but measured in the aftward direction to the target pixel. In the cross track direction, parallaxes caused by camera view-angles are much smaller than that by cloud motion and cloud-top height. Therefore, cross-track parallaxes should be safely bound by $\pm U_c$.

Following the above argument, the search window (Figure 2.4) can be placed in the comparison image with

$$\begin{aligned} U_a(trailing) &= U_c \\ U_a(leading) &= U_c + \frac{h_{\max}}{1100m}\left|\tan\theta_2 - \tan\theta_1\right| \\ U_c &= \frac{v_{\max}\Delta t}{1100m} + 4 \\ \Delta t &= t_{comparison} - t_{reference} \end{aligned}, \tag{5}$$

where, $v_{\max}$ is the maximum cloud speed and is set to 100 m/s, Δt is the time interval between two cameras (the typical values of Δt can be calculated from Table 2.1), and $h_{\max}$ is the cloud maximum height and is set to 20,000 m. An additional of four pixels is added to U_c to ensure the parallax is bound by the search window. Therefore, the height (H) and width (W) of the search window is given by

$$\begin{aligned} H &= U_a(leading) + U_a(trailing) + 1 \\ W &= 2U_c + 1 \end{aligned}. \tag{6}$$

In the case of the comparison camera pointing "more aftward" than the reference camera, the value of $U_a(leading)$ and $U_a(trailing)$ in Equation (4) are swapped. Because Terra travels westward as it flies from the north pole to south pole, a parallelogram shape of the search window should be more appropriate to reduce computational expenses. In this thesis, the search window is set to be rectangular for simplicity.

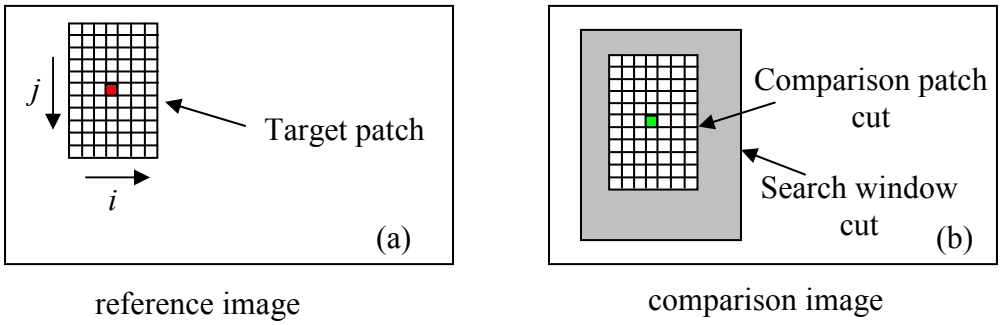

Figure 2.3. *Illustration of registering a target pixel within the reference image (a) in the comparison image (b).*

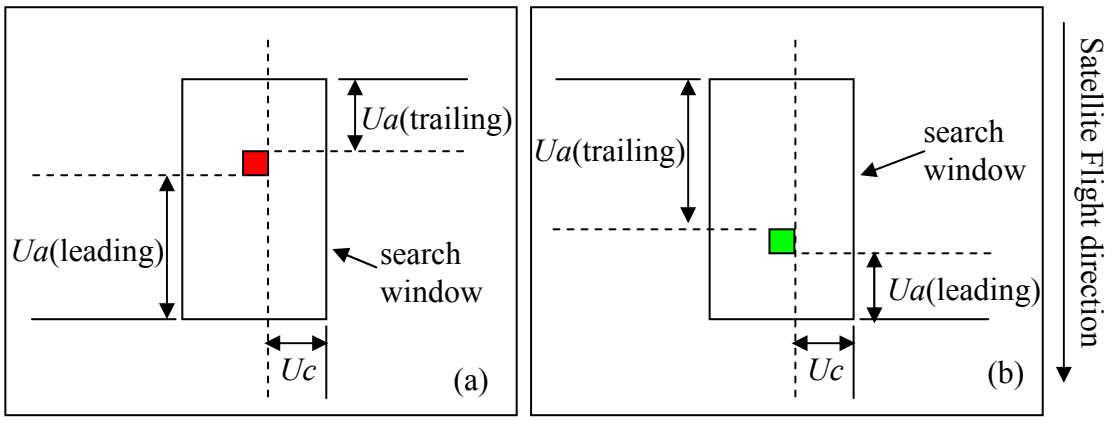

Figure 2.4. *Illustration of placing the search window in the comparison image for the case that (a) the comparison camera points more forward than the reference camera and (b) the comparison camera points more aftward than the reference camera.*

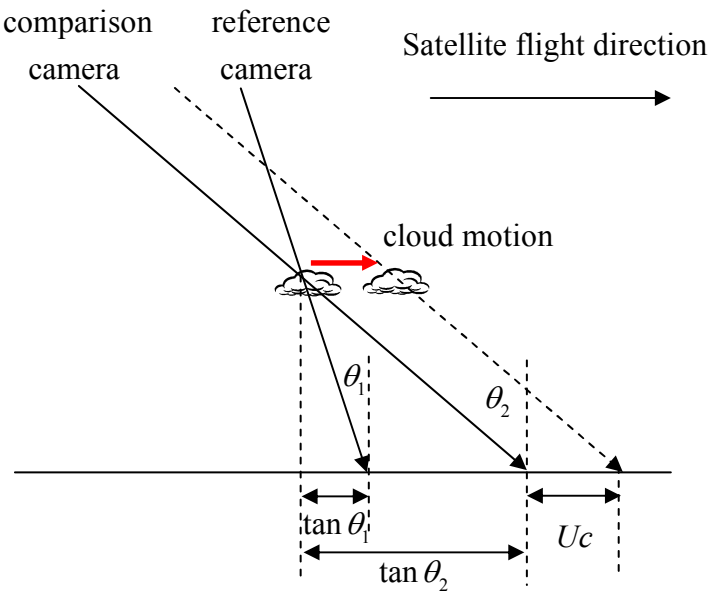

Figure 2.5. *Illustration of projections of a cloud by two MISR cameras for the case that clouds move in the same direction as that of the satellite.*

Table 2.1. *Nominal view zenith angles (θ) and typical camera travel times represented by the number of lines (n_i) at 275m resolution and by second (t_i) for each MISR camera to observe the same object on the Earth ellipsoid surface. The relationship between n_i and t_i is linear, expressed as t_i=0.0408*n_i. The value of n_i and the formula for t_i are from Diner [1999] .*

camera	***θ***	***n_i***	***t_i (sec)***
Df	70.5	0	0
Cf	60.0	1468	59.89
Bf	45.6	2760	112.61
Af	26.1	3887	158.59
An	0.0	5000	204.00
Aa	-26.1	6113	249.41
Ba	-45.6	7240	295.39
Ca	-60.0	8532	348.11
Da	-70.5	10000	408.00

2.3.2 Domain Registration Technique

In *Horvath and Davies* [2004], they registered radiances of a cloud element within a 70.4 km^2 domain measured by all MISR cameras at 275 m resolution based on the average parallax of clouds over the 70.4 km^2 domain; that is, radiances are registered at a constant altitude regardless of variations in motion and height of clouds within the coarse domain. It works well for stratiform clouds, but not cumuliform clouds. At the other extreme, if radiances are registered at the pixel-level, it is possible that a radiance measured from a cloud fully covering a single pixel in one camera image be split over two pixels in another camera image, and the radiances from a cloud fully covering M pixels in one camera is split over M+1 pixels in another camera [*Jovanovic et al.,* 1999]. In such case, averaging the radiances over a larger area helps alleviate this problem.

For these two reasons, we choose 3×3 1.1-km pixels as our domain size throughout our analysis and accordingly, the registrations of cloud element are performed for each identified fully cloudy water domain. Figure 2.6 shows the algorithm flow chart. At 1.1 km resolution, for every domain's pixel in the reference image, we register it in the comparison image at the pixel-level with a 7×11-pixel matching patch (Section 2.3.1). Because the magnitude and direction of the parallax will depend on the altitude and wind vector of the cloud, we require that all 9 pixels belonging to a domain return the same parallax. When this requirement is not met, a larger patch is used to yield more accurate registration (at the cost of more computation) as recommended by *Muller et al.* [2002]. Thus, we further increase the patch sizes from 7×11 pixels in increments of 2 pixels in both the along and cross track directions (i.e., 9x13, and up to 17×21) until the 9-pixel parallax agreement is met, otherwise, the domain is discarded from our analysis.

The domain registrations are performed between the MISR AN-camera image and each oblique camera image, namely, AN-AF, AN-BF, AN-CF, AN-DF, AN-AA, AN-BA, AN-CA and AN-DA camera pairs. The cloud texture similarity between the AN-camera image and an oblique-camera image decreases with camera obliquity. The AN-AF (AN-AA) image pair has the largest similarity among the four image pairs of the forward (aft) cameras and the AN-DF (AN-DA) image pair has the smallest similarity. The decrease in texture similarity will increase registration errors and lower our confidence in registration, making it more difficult to meet the 9-pixel parallax agreement and decreasing the number of successfully registered domains in the more oblique-camera image. However, the texture similarity among two neighboring cameras is less affected by camera obliquity. Based on this, the following algorithm is adopted to maintain registration reliability.

1. All 3×3 1.1-km-pixels fully cloudy water domains are identified in the MISR AN-camera image with all 9 pixels having τ and r_e retrievals after registration is performed between MODIS and MISR images (Section 2.2);
2. registrations for these domains are performed in the AN-AF;
3. for domains having successful registration in AN-AF, their registrations in AF-BF are performed and this information is used for placing the search windows of the registration in AN-BF. Because this information is a good estimate for registering a domain of the AN camera image in the BF camera image the search window size for registering in AN-BF does not need to be too large. In this algorithm, the search window size is set to 9×5 (along-track × cross track) pixels for registering in pairs of AN-BF, AN-CF and AN-DF;

4. following Step 3, registering in AN-CF are performed by taking the registrations in BF-CF as the estimates for placing the search windows. The registrations in AN-DF are performed in the same way.
5. repeating Steps 1 to 3, but it is for the registrations in AN-AA, AN-BA, AN-CA and AN-DA.

For clouds observed over the northeastern Pacific used in the analysis in Chapter 3, 65.4% of fully cloudy water domains have been successfully registered in all 9 cameras. Excluding the two 70.5° MISR cameras increases the registration rate to 76.1%. For clouds observed in the months of January and July between 2001 and 2008 over the globe (Chapter 4 and 5), Figure 2.7 also clearly shows that the number of fully cloudy water domains decreases when more oblique cameras are included. The impact of the decreasing successful registration with view obliquity on our results will be discussed in Chapter 3, 4 and 5.

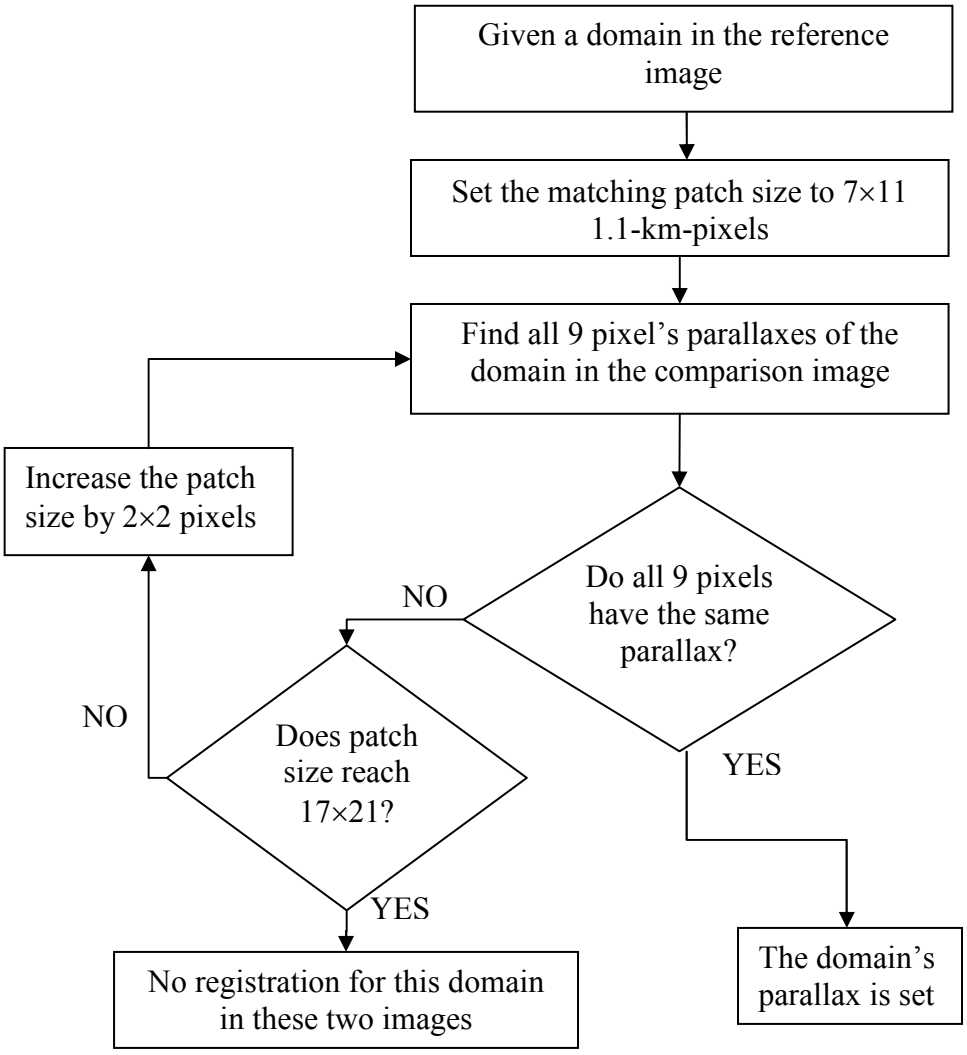

Figure 2.6. *Flow chart for registering a 3×3-1.1km-pixel fully cloudy water domain in two MISR camera images.*

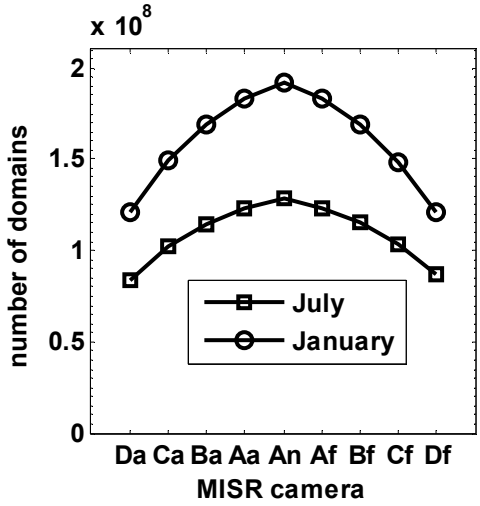

Figure 2.7. *Successful registration rates for fully cloudy water domains as a function of including more MISR oblique cameras for the group of the forward cameras and the group of aftward cameras, in the months of January and July between 2001 and 2008. A domain having a successful registration in an oblique camera will also have registrations in the less oblique cameras for the group of the forward cameras and the aftward cameras, respectively. For example, if a domain is registered in the Ca camera, it will also be registered in the Ba and Aa cameras.*

CHAPTER 3:QUANTIFICATION OF THE VIEW-ANGLE CONSISTENCY OF CLOUDS

This chapter presents the viability of using view-angle consistency to quantify cloud angular anisotropy in the upwelling radiation, and the degree to which the plane-parallel assumption is valid for any given application requirement. Three view-angle consistency metrics are defined from bidirectional reflectance factor (BRF), cloud optical thickness and cloud spherical albedo. The relationships between these view-angle consistency metrics and cloud-top spatial heterogeneity are also examined. The analysis was done with a fused dataset of 6 years of oceanic water cloud observations over an area of the northeastern Pacific from the Moderate Resolution Imaging Spectroradiometer (MODIS) and the Multiangle Imaging SpectroRadiometer (MISR). This chapter is nearly identical to an article published in *Geophysical Research Letters* by *Liang et al.* [2009] (Reproduced by permission of American Geophysical Union). The detailed description of the instruments, dataset, and method of data fusion are described in Chapter 2. However, a brief discussion is retained here to stay true to *Liang et al.* [2009]. Only minor text changes are done to keep in format with the flow of this thesis. Also, an additional Figure is added (Figure 3.3). On the basis of the approach described in this chapter, a global analysis of the geophysical distributions of oceanic water cloud view-angle consistency will be examined and presented in Chapter 4.

3.1 Abstract

View-angle consistency in bidirectional reflectance factor (BRF), optical thickness and spherical albedo is examined for marine water clouds over a region of the northeastern Pacific using six years of fused MODIS and MISR data. Consistency is quantified by the root-mean-square of relative differences between MISR-measured BRF and their plane-parallel values and variation of plane-parallel retrieved optical thickness and spherical albedo across multiple view-angles. Probability distribution functions of consistency show that, for example, these clouds are angularly consistent within 5% in BRF, optical thickness and spherical albedo 72.2%, 39.0% and 81.1% of the time, respectively. We relate angular consistency to the spatial variability of nadir-BRF, thus allowing us to potentially identify, with a prescribed confidence level, which MODIS microphysical retrievals within the MISR swath meet the plane-parallel assumption to within any desired range in view-angle consistency.

3.2 Introduction

All operational satellite retrievals of cloud optical properties from scattered solar radiances assume one-dimensional radiative transfer (1D-RT), whereby clouds and the imposed boundary conditions are treated as horizontally homogeneous (i.e., plane-parallel), with cloud layers usually assumed to be vertically homogenous. The applicability of this assumption has been examined through many observational [*e.g., Loeb and Davies,* 1996, 1997; *Loeb and Coakley,* 1998; *Genkova and Davies* 2003; *Horvath and Davies,* 2004; *Várnai and Marshak*, 2007] and three-dimensional radiative transfer modeling [*e.g., Loeb et al*., 1998*; Várnai and Davies,* 1999; *Kato et al*., 2006]

studies. However, the following fundamental question remains: how often is this assumption good enough? Clearly, "good enough" will depend on the application, and its answer will depend on, preferably, a globally representative dataset of true optical properties of clouds. Given the lack of such a dataset, we must seek alternative ways to answer this question. Two recent studies, *Genkova and Davies* [2003] and *Horvath and Davies* [2004] have made such attempts. *Genkova and Davies* [2003] examined the spatial contrast of MISR near-infrared BRF as a function of spatial scale and found that only a small fraction of the clouds were homogeneous for a range of spatial contrast thresholds. However, the spatial contrasts in BRF were not explicitly tied to the quality of cloud microphysical retrievals under the plane-parallel assumption. *Horvath and Davies* [2004] examined the anisotropy of water cloud BRF and found ~17% of cloudy pixels at 275 m resolution (~30% at 3.3 km resolution) had agreement between 1D-RT modeled BRFs and MISR-observed BRFs to within ±5% for all MISR view-angles (See Section 3.3.1 for MISR instrument description), when the views were coregistered to a constant altitude over 70.4 km^2 domains. However, there was no tie to the spatial heterogeneity of the scene, and it is not clear whether the ±5% threshold is appropriate for all applications.

In this study, we extend the *Horvath and Davies* [2004] approach in several ways. Our approach fuses the MISR multi-angle radiances with the MODIS cloud optical thickness (τ) and effective radii (r_e) retrievals. Fusion is done at cloud top and at pixel resolution (~1 km^2, rather than a 70.4 km^2 domain) using a new cloud element registration scheme (Section 3.3.2). Angular consistency metrics are defined (Section 3.3.3) for BRF, τ and cloud spherical albedo (β) to ascertain the appropriateness of the 1D-RT assumption on different properties of the cloud. The metrics are applied to water

clouds over a large region of the northeastern Pacific Ocean for data collected over six years, providing ample sampling to study the frequency of occurrence in the metric values and their relationship to cloud heterogeneity (Section 3.4).

3.3 Data and Methodology

3.3.1 Instruments and Dataset

MODIS, onboard the Terra and Aqua satellite platforms, retrieves τ and r_e across its 2330 km swath at a ground-resolution of 1 km at nadir [*Platnick et al.,* 2003]. MISR, also on Terra, provides nine views of the same scene on Earth within seven minutes from its multi-camera design, with viewing zenith angles of 0°, ±26.1°, ±45.6°, ±60.0°, and ±70.5° along the forward and aft directions of the orbital-track [*Diner et al.,* 1998]. BRFs are measured at 4 spectral channels (three visible and one near-infrared), with the ground resolution varying from 275 m to 1.1 km, depending on the channel, across a swath of ~ 400 km that falls near the center of the MODIS swath.

MISR and MODIS data were extracted from Path 47 and 48 of Terra within a region bound by 9.8°N to 40.3°N and 122.7°W to 137.4°W at approximately 10:30 am local time as defined by the sun-synchronous orbit of Terra. This region is dominated by stratus and stratocumulus to the north and transitions to trade wind cumuli and deeper cumuli to the south, although other cloud types are also noted [*e.g., Hahn and Warren,* 1999]. 302 orbits from May 2000 to April 2006 were used in this study. Version 24 of the MISR Level 1B2 georectified and calibrated near-infrared (0.86 μm) BRFs and the MODIS Collection 5 near-infrared (0.86 μm) BRF, MOD06 τ, r_e, and retrieval cloud phase flag were used in our analysis. Only water clouds were considered in our analysis

based on the cloud phase flag. The MODIS Collection 5 cloud retrieval algorithm does not process cloud edges (as determined from the MODIS cloud mask, MOD35). These edge pixels are therefore excluded from our analysis.

3.3.2 Cloud Element Registration

The MODIS BRF, τ and r_e reported at 1 km resolution on the MODIS swath are registered to the MISR 1.1 km resolution grid with the General Cartographic Transformation Package software [*U.S. Geological Survey,* 1993]. To reduce registration errors of cloud elements originating on different grids, we define a domain as a region consisting of 3×3 1.1-km pixels (justified in Chapter 2) with all nine pixels having successful τ and r_e retrievals. Our analysis shows that these domains contain 79.5% of all pixels having successful τ-r_e-retrievals, since not all successful τ-r_e-retrievals fall within 3×3 pixel domains that are fully cloudy. The relative difference between the BRF from the MISR nadir camera and from MODIS is given by

$$\delta_{OBS} = \frac{(\overline{R}_{MISR\_NADIR} - \overline{R}_{MODIS})}{(\overline{R}_{MISR\_NADIR} + \overline{R}_{MODIS})/2} \times 100\%,$$

where $\overline{R}_{MISR\_NADIR}$ and $\overline{R}_{MODIS}$ are average near-infrared BRFs for MISR-nadir camera and MODIS over a domain, respectively. When averaged over all domains in our dataset, $\overline{\delta_{OBS}}$ = 1.37% with a standard deviation (σ) of 4.74%. The non-zero value of $\overline{\delta_{OBS}}$ arises from differences in the spectral response function and radiometric calibration between MISR and MODIS, whereas registration errors also contribute to σ [*e.g., Lyapustin et al.,*

2007]. The impact of registration errors could be reduced by accepting only those domains having a δ_{OBS} within $\overline{\delta_{OBS}} \pm \sigma$; 78.8% of domains meet this criterion. We refer to this as the MODIS-MISR registration criterion (MMRC).

We also need to register cloud elements across MISR images acquired from multiple view directions (a complete description in a greater detail is presented in Chapter 2). Because of the way MISR projects and regrids its BRFs from all cameras to a common Space-Oblique Mercator (SOM) grid on the World Geodetic System 1984 ellipsoid surface, it is possible that a BRF from a cloud fully covering a single pixel in a nadir camera image be split over two pixels in an oblique camera image, and the BRFs from a cloud fully covering M pixels in the nadir camera is split over M+1 pixels [*Jovanovic et al*., 1999]. The same is also true when reprojecting MODIS data onto the MISR grid. Thus, averaging the BRFs over larger areas helps alleviate this problem. For this reason, we choose 3×3 1.1 km pixels as our domain size throughout our analysis.

Identifying the same cloud across MISR images from multiple views is equal to finding the cloud displacements (parallaxes) in the oblique images relative to the nadir image on the SOM grid. We use the MISR area-matching algorithm M2 [*Muller et al.,* 2002] and implement it as follows to increase reliability in the match (but at the expense of coverage). At 1.1 km resolution, for every pixel in the nadir image that belongs to a domain, we center a 7×11-pixel patch on it and compare the patch to all 7×11-pixel patches within a large search window in an oblique image. Where a patch in the oblique image best matches the nadir target patch based on the M2 criteria, the center pixel on the patch in the oblique image is registered to the target pixel in the nadir image. Because the magnitude and direction of the parallax will depend on the altitude and wind vector of the

cloud, we require that all 9 pixels belonging to a domain return the same parallax. When this requirement is not met, a larger patch is used to yield more accurate registration (at the cost of more computation) as recommended by *Muller et al.* [2002]. Thus, we further increase the patch sizes from 7×11 pixels in increments of 2 pixels in both the along and cross track directions (i.e., 9x13, and up to 17×21) until the 9-pixel parallax agreement is met, otherwise, the domain is discarded from our analysis.

Matching clouds in the oblique images to the target clouds in the nadir image becomes more difficult with view obliquity, largely because the texture of clouds change with view angle. For the domains that have passed through the MODIS-MISR registration criteria, 65.1% of the domains had all 9 MISR cameras meet our registration requirements. In this study, we exclude the two 70.5° MISR cameras, resulting in a registration rate for the remaining 7 cameras of 75.8%. Hereafter, the domains that have passed though the MODIS-MISR and 7-MISR-camera registration criteria are referred to as the qualified domains (~60% of all domains) and the others are the unqualified domains. Both qualified and unqualified domains will be examined in Section 3.4.

3.3.3 Angular Consistency Metrics

We first retrieve τ from the MISR nadir camera using the near-infrared BRF from the MISR nadir camera and r_e from MODIS, based on the same radiative transfer model used to construct the look-up tables in the MODIS τ and r_e retrievals [*King et al*., 1997]. The BRFs for the seven MISR view-angles are then simulated using the MISR τ and MODIS r_e. Within a domain, the observed MISR BRFs and simulated BRFs are averaged and designated $\overline{R}_i^{OBS}$ and $\overline{R}_i^{SIMU}$, respectively, where i is the MISR camera index (i = {1,

2, …, 7}). If clouds are truly plane-parallel and meet all assumptions used by the MODIS microphysical retrieval algorithm, then we would expect the relative difference between $\overline{R}_i^{OBS}$ and $\overline{R}_i^{SIMU}$, $\delta R_i = \frac{\overline{R}_i^{OBS} - \overline{R}_i^{SIMU}}{\overline{R}_i^{OBS}}$, to be close to zero for all values of *i*. The root-mean-square of the absolute value of δR_i from all chosen cameras defines the BRF angular consistency metric:

$$m_{BRF} = \sqrt{\frac{1}{n}\sum_{i=1}^{n}\left(\delta R_i\right)^2} \times 100\%, \tag{1}$$

where n=7 is the number of MISR cameras used in the calculation.

Alternatively, τ and β can be retrieved for all MISR cameras. Since τ and β should not be a function of viewing geometry for plane-parallel clouds, angular consistency metrics can be defined by the coefficient of variation of the retrieved τ or β:

$$m_x = \frac{1}{\langle \overline{x}_i \rangle}\sqrt{\frac{1}{n-1}\sum_{i=1}^{n}\left(\overline{x}_i - \langle \overline{x}_i \rangle\right)^2} \times 100\%, \tag{2}$$

where, x is either τ or β, $\overline{x}_i$ is the average τ or β over a domain in the i^{th} MISR camera and $\langle\ \rangle$ denotes averaging over the n cameras. We infer β from plane-parallel calculation using τ and r_e as input.

These metrics should not be interpreted as an estimation of the uncertainty in the MODIS microphysical retrievals. Rather, they simply quantify the angular consistency from BRF, τ and β. This is a self-consistency test of validation of plane-parallel

assumption. As such, the metrics point to the degree to which the plane-parallel assumption and other assumptions used by the MODIS retrieval algorithm are valid in a possibility sense. A lower metric value (a higher view-angle consistency) suggests that plane-parallel is appropriate with a higher chance from examinations in the available view-angles, which does not guarantee the cloud is view-angularly consistent for all view-angles. However, a larger metric value (a lower view-angle consistency) should go hand-in-hand with lower confidence in the validation of plane-parallel assumption, thus, the quality of the MODIS microphysical retrievals and the associated estimate of uncertainty [*Platnick et al.,* 2005] found in the product.

3.4 Results

As an example of the spatial characteristics of the metrics, Figure 3.1 shows $\bar{\tau}$ retrieved from nadir, m_{BRF}, m_{τ} and m_{β}, as well as a spatial heterogeneity metric, H_{σ}, defined below. This figure gives a sense that large values of the metrics occur for regions near cloud edges, small clouds and thin clouds, whereas small values of the metrics occur for central regions of thicker extensive clouds. This is consistent with the expectation that thick, extensive clouds should be the most appropriate clouds for the validity of the plane-parallel assumption and the least sensitive to the treatment of ocean reflectance in the retrieval.

Figures 3.2a, 3.2b and 3.2c show the probability distribution functions (PDF) and cumulative PDFs in the occurrence of m_{BRF}, m_{τ} and m_{β}. We see that clouds for the qualified MMRC+7MRC domains in our dataset are angularly consistent in BRF to within 5% of their plane-parallel value 78.5% of the time and are angularly consistent to

within 5% in τ and β 44.3% and 85.9% of the time, respectively. For metric values ≤ 10%, the angular consistency rates increase to 96.1%, 84.5% and 97.8% for m_{BRF}, m_τ and m_β, respectively. The angular consistency rate of 78.5% for the $m_{BRF} \leq 5\%$ is nearly three times as high as that shown in Figure 2 of *Horvath and Davies* [2004], where about 30% pixels are angularly consistent at 3.3 km resolution. Although the disagreement may be attributed to clouds over different regions as compared to their study (i.e., they used data between 60°N and 60°S from 28 MISR orbits collected in two days), the following additional differences are also relevant: (1) metrics defined here reflect the overall consistency at all chosen view-angles rather than any single view-angle, (2) we exclude the two most oblique cameras where confidence in the registrations is lower than in the less oblique cameras, (3) MISR cameras are registered at cloud tops rather than at a single altitude over 70.4 km^2 regions, and (4) cloud edge pixels, pixels not included in a domain and pixels in the unqualified domains are excluded from our analysis.

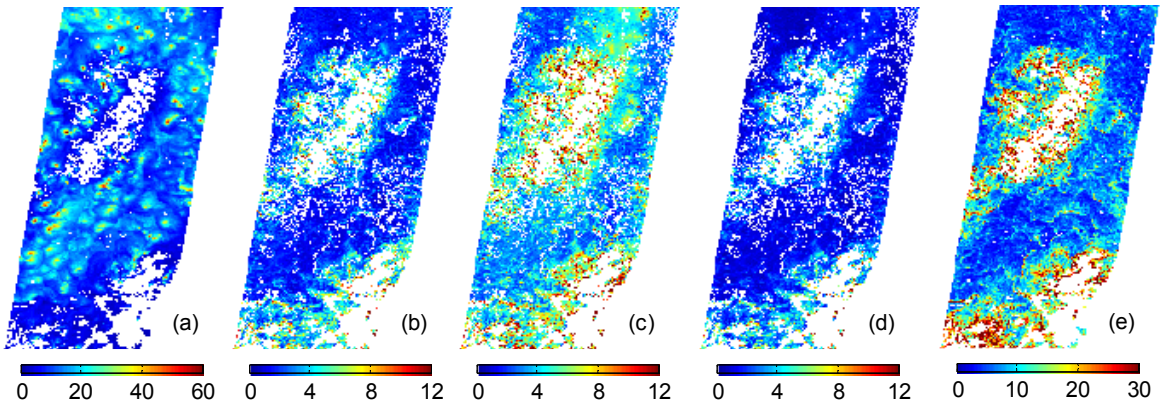

Figure 3.1. *Examples of (a) the mean cloud optical depth, (b) m_{BRF} metric, (c) m_τ, (d) m_β and (e) H_σ for domains composed of 3x3 1.1-km-pixels. The data are for MISR block 68 to 74, orbit 14700, collected on 22 September 2002 within 19.8°N to 21.1°N and 128.5°W to 133.8°W. White represents regions where domains do not meet the MODIS-MISR or 7-camera registration criterion.*

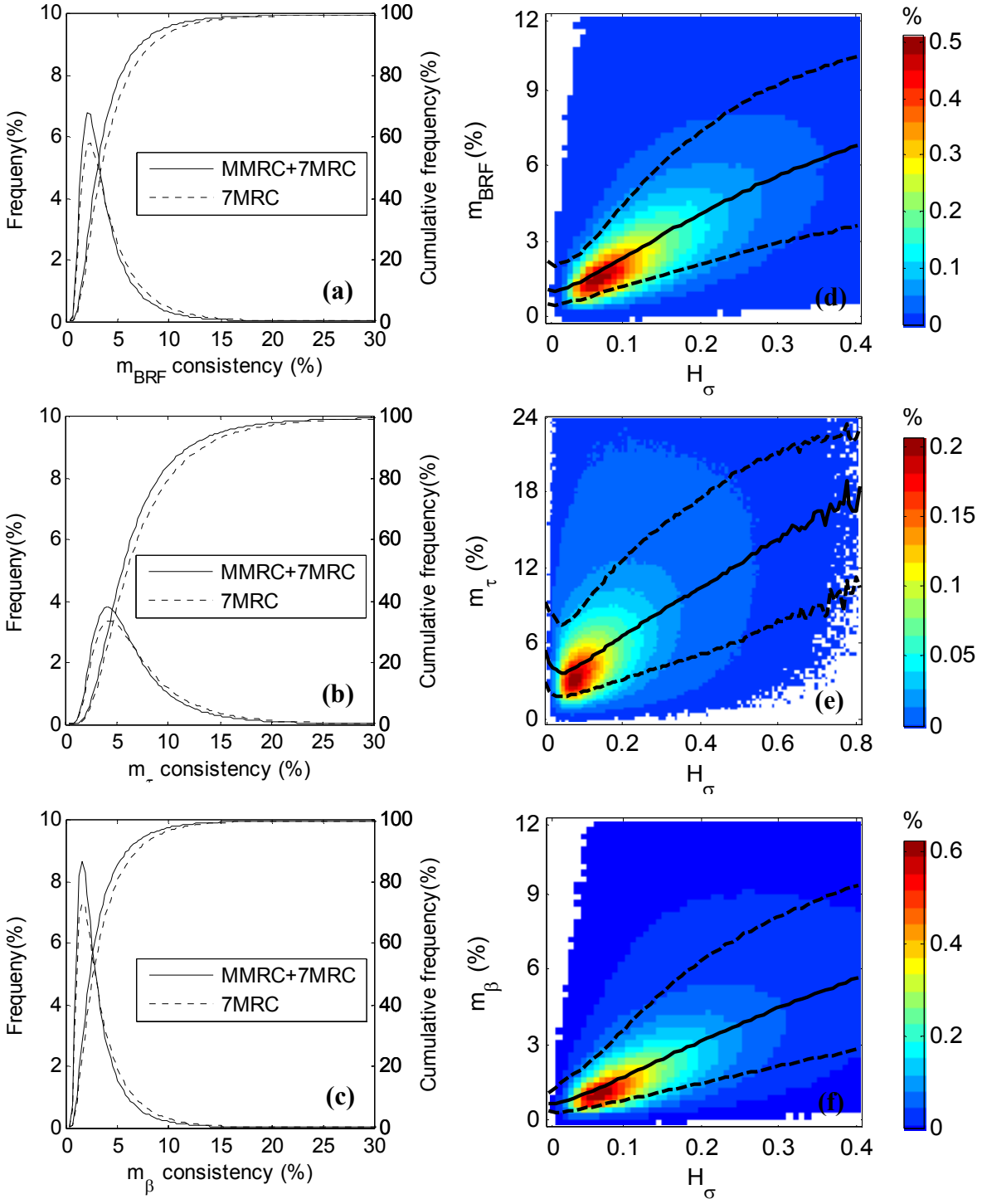

Figure 3.2. *(a), (b) and (c) Probability distribution functions (PDF) and cumulative PDFs in m_{BRF}, m_{τ}, and m_{β} metric, respectively, for qualified MMRC+7MRC and 7MRC domains. (d), (e) and (f) 2-D frequency distribution of H_{σ} versus m_{BRF}, m_{τ}, and m_{β} metric, for 7MRC domains. The median (solid thick line), 10th and 90th percentile (dotted lines) of the angular consistency metrics computed over H_{σ} bin intervals of 0.008 are also plotted.*

Since biases of the 1D-retrieved cloud optical properties depend on cloud spatial heterogeneity, so too must the angular consistency. We tested several spatial metrics and found that spatial metrics based on the high resolution (275m) BRFs from the MISR nadir camera provided the simplest and best single-variable relationships with the angular consistency metrics. One such heterogeneity metric is defined as:

$$H_\sigma = \frac{\sigma}{\overline{R}},$$

where $\overline{R}$ is the domain's mean BRF with a standard deviation of σ.

Recall that the unqualified MMRC+7MRC domains represent ~40% of all domains. The PDF of H_σ for the unqualified MMRC+7MRC domains (Figure 3.3) is skewed towards larger values compared to the qualified MMRC+7MRC domains. This is because the MMRC favors rejecting more heterogeneous clouds, while, to a lesser extent for the sampled clouds, the 7MRC favors rejecting more homogeneous clouds (Figure 3.3). If we assume that within a narrow H_σ-bin, the angular consistency metric PDFs are the same for both the qualified and unqualified MMRC+7MRC domains, then the angular consistency performance of the unqualified MMRC+7MRC domains can be predicted based on the PDF of H_σ. Following this method, we predict for metric values < 5%(10%) consistency rates of 73.0%(94.4%), 40.0%(81.1%) and 81.7%(96.8%) for m_{BRF}, m_τ and m_β, respectively, for all domains. Compared to angular consistency rates derived from the qualified MMRC+7MRC domains, the differences are within 6%.

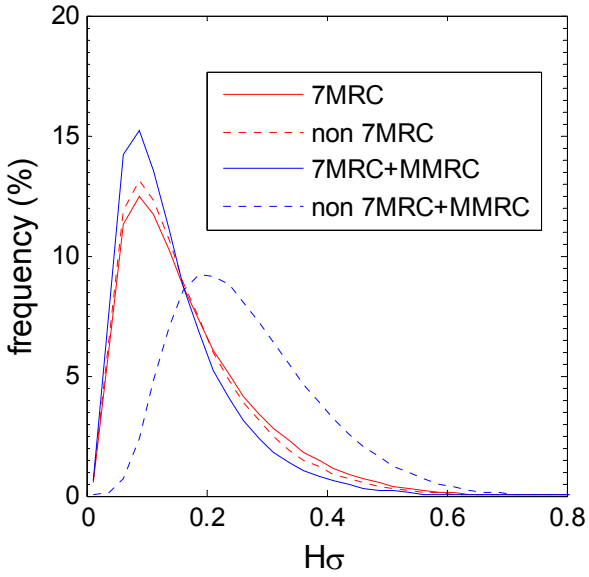

Figure 3.3. *Probability distribution functions for qualified and unqualified 7MRC domains (7MRC and non 7MRC, respectively) as well as qualified and unqualified 7MRC+MMRC domains (7MRC+MMRC and non 7MRC+MMRC, respectively).*

When MMRC is omitted (only 7MRC is applied), lower consistency rates are expected for metric value < 5%(10%) compared with those of qualified MMRC+7MRC domains, as showed in Figures 3.2a, 3.2b and 3.2c: they are 71.7%(94.1%), 38.7%(79.9%) and 80.7%(96.7%) for m_{BRF}, m_{τ} and m_{β}, respectively, for the qualified 7MRC domains. Consistency rates are estimated for the unqualified 7MRC domains using the method described in the paragraph above, leading to consistency rates for all fully cloudy domains of 72.2%(94.3%), 39.0%(80.2%) and 81.1%(96.8%) in m_{BRF}, m_{τ} and m_{β}, respectively, for metric value < 5%(10%). Note that the differences with the qualified-only 7MRC domains are less than 1%. The differences are also less than ~1% compared to the consistency rates estimated in the paragraph above for all domains using MMRC+7MRC. These small differences indicate that our analysis applied to the

qualified 7MRC domains alone produces essentially unbiased results relative to the population of all fully cloudy domains.

Figure 3.1 gives a clear sense that large values of H_σ are associated with large values of the angular consistency metrics. This is further quantified in Figures 3.2d, 3.2e and 3.2f , which shows the 2-D distribution between angular consistency metrics and H_σ for the qualified 7MRC domains. As the cloud becomes more spatially heterogeneous within the domain (i.e., as H_σ increases), the mode and spread of the angular consistency metrics become larger. Analyses based on Figures 3.2d, 3.2e and 3.2f show that for the 10% most spatially homogeneous domains, m_{BRF} and m_β are < ~2% and m_τ is < ~15% almost all the time. For the 10% most spatially heterogeneous domains, m_{BRF}, m_τ and m_β are < ~5% for ~32%, 8% and 49% of the time, respectively. The relationship between the angular consistency and cloud spatial heterogeneity suggests the viability of using a cloud spatial heterogeneity criterion, based on MODIS observations falling in the MISR swath, for identifying pixels that are not "good enough" for performing 1D-retrievals. For example, requiring 99% of the retrievals to be angularly consistent in BRF to within 5% of their plane-parallel value (i.e., $m_{BRF} \leq 5\%$; analogous to the 5% "good enough" criterion imposed by *Horvath and Davies* [2004] discussed in Section 3.2), suggests performing retrievals only where $H_\sigma < 0.08$; ~17.7% of domains met this criterion.

3.5 Discussion

We have examined the view-angle consistency in BRF, τ and β for marine water-clouds over the northeastern Pacific using six years of MISR and MODIS data. The clouds were sampled at the 10:30 am equator-crossing time of the Terra orbit. PDFs of

metrics defining angular consistency quantify the plane-parallel nature of these clouds, allowing one to set thresholds on what they would deem "good enough" to be plane-parallel. For example, setting thresholds for all metrics at 5%(10%), the clouds in our dataset are angularly consistent in MISR-observed BRF to their plane-parallel values 72.2%(94.3%) of the time and to within 5%(10%) in τ and β 39.0%(80.2%) and 81.1%(96.8%) of the time, respectively. The results for 5% consistency in m_τ (39.0%) and in m_{BRF} (81.1%) may seem inconsistent; however, this is likely attributed to the non-linear relationship between BRF and τ. The angular consistency metrics was also shown to be associated with spatial heterogeneity. This allows one to set thresholds in spatial heterogeneity to identify, at a prescribed confidence level, which domains are angularly consistent to within a desired range (e.g., requiring ~99% of the retrievals to be angularly consistent in BRF to within 5% of their plane-parallel value suggests performing retrievals only where H_σ is < 0.08).

Although the angular consistency depends, on average, on the spatial heterogeneity of the cloud field, it is by no means the only factor determining the magnitude of the angular consistency, as indicated by the spread of data in Figures 3.2d, 3.2e and 3.2f. For example, there are some very smooth clouds that have large angular consistency metrics. This can potentially arise from deviations from other assumptions/inputs used in the MODIS plane-parallel retrievals of cloud microphysical properties, such as an assumed vertically homogeneous distribution of cloud microphysical properties, an assumed lambertian surface, and a correct classification of cloud phase. There are also a small number of clouds that are spatially heterogeneous with small angular consistency metrics, which we are only able to attribute to chance.

Note that the results are derived for clouds observed and cloud optical properties retrieved at 1.1 km resolution only. *Horvath and Davies* [2004] demonstrated that angular consistency, akin to m_{BRF}, depends on resolution, with clouds appearing more plane-parallel with coarser resolution. We anticipate a similar behavior in our results, but this remains to be proven.

Finally, the approach we have taken to assess the validity of the plane-parallel and other assumptions used in the MODIS retrievals is not limited to clouds over the northeastern Pacific. In Chapter 4, we will apply our approach to a global dataset to provide a broader perspective on this problem.

CHAPTER 4: VIEW-ANGLE CONSISTENCY OF OCEAN WATER CLOUDS

Based on the technique developed in Chapter 3 for examining the cloud view-angle consistencies relative to their plane-parallel expectations using three metrics (m_{BRF}, m_{τ}, and m_{β}), this chapter presents a global analysis of these metrics to study their spatial distribution and how they depend on such factors as seasonal variation, cloud type and solar zenith angle (SZA). This chapter is compiled from an article in preparation for submission to *Science* magazine titled "*A global view on the plane-parallel nature of oceanic water clouds*". The detailed descriptions of the instruments, dataset, and method of data fusion are described in Chapter 2. Additional discussion, three figures and one table are added (Figures 4.5, 4.6 and 4.11, Table 4.1) beyond what is planned for the article in preparation.

4.1 Introduction

Solar radiation is the primary source of energy that drives our climate system. The solar radiation that is absorbed by the atmosphere and the surface causes heating and photochemical reactions that make life possible on Earth, whereas the solar radiation that is scattered back to space is exploited by satellites to remotely sense Earth's surface and atmospheric properties. Clouds, which cover about 70% of the globe [*Rossow and Schiffer,* 1999], modulates the incident solar radiation field in space and time more than any other atmospheric variable, and they act as the primary greenhouse constituent in our atmosphere [*Ramanathan et al*., 1989]. Therefore our ability to accurately compute the

interaction of the radiation field with clouds is of great importance in environmental research, including, for example, our ability to predict climate change based on global climate models [e.g., *Cess et al.,* 1989], to quantify the climate forcing by anthropogenic aerosols through its influence on cloud microphysics [*e.g., Charlson et al.,* 1992; *Barker,* 2000], to produce accurate predictions of biogeochemical cycles [e.g., *Sellers et al.,* 1997], and to monitor environmental change from space [*e.g., Wang and Key*, 2003].

Common to all these areas of research is the ubiquitous use of the plane-parallel assumption in calculating the radiative transfer needed in computing heating rates and photochemical reactions, and in constructing satellite remote sensing algorithms used in retrieving atmospheric properties. The plane-parallel assumption assumes that the medium and its radiative boundary conditions are horizontally homogeneous, thereby causing the horizontal radiative flux divergence to be zero. This greatly simplifies the radiative transfer to one-dimension (the vertical), making the radiative transfer calculations computationally fast and solutions to the inverse problem faced in satellite remote sensing tangible. However, a simple look at clouds, either from the ground, aircraft or spacecraft reveals that they are certainly not horizontally homogenous, thereby raising questions as to the degree to which the plane-parallel assumption is valid and its impact on radiative transfer calculations and remote sensing of optical properties for real clouds.

Many studies have given important insight into the applicability of the plane-parallel assumption and its impacts on calculating radiative fluxes or retrieving cloud properties [*e.g., Loeb et al.,* 1997, 1998; *Genkova and Davies*, 2003; *Horvath and Davies*, 2004; *Várnai and. Marshak,* 2007; *Cahalan*, 1994; *Zuidema and Evans,* 1998; *Fu*

et al., 2000; *Cole et al.,* 2005; *Kato et al.,* 2006; *Liang et al*., 2009]. Most of these have been either derived over a limited regional domain from observations or from computationally expensive 2- or 3-D radiative transfer calculations applied to a few heterogeneous cloud fields. While the impacts and implications range from marginal to severe, depending on which dataset are examined or the type of cloud fields being simulated, what we are lacking is a global perspective of the degree to which the plane-parallel assumption is valid for real clouds and its relationship to the heterogeneity of the cloud field. The only reasonable way to gain this global perspective is through the analysis of satellite data.

This chapter provides this perspective for global observations of marine water clouds using a novel approach that we recently developed and tested on a limited regional dataset [*Liang et al*., 2009]. The approach fuses the near-infrared (866 nm) radiances measured near-simultaneously from multiple directions from the Multi-angle Imaging SpectroRadiometer (MISR) [*Diner et al.,* 1998] with cloud microphysical properties retrieved from the Moderate Resolution Imaging Spectroradiometer (MODIS) [*Platnick et al*., 2003]. The valid use of the plane-parallel assumption is quantified by view-angle consistency in bidirectional reflectance factor (BRF), namely, the root-mean-square of relative differences between MISR-measured BRF and their plane-parallel values, designated as m_{BRF}, and by variation of plane-parallel retrieved optical thickness and spherical albedo across multiple view-angles, designated as m_{τ} and m_{β}, respectively.

4.2 Methodology

Oceanic water clouds observed by MISR and MODIS in the months of January and July between 2000 and 2008 are fused to provide an unprecedented accurate dataset for this study. Details of the data fusion are presented in Chapter 2. The fused data include cloud thermodynamic phase, cloud optical thickness, effective radius and radiance (that is converted to BRF via Equation 1 in Chapter 2). The degree of cloud view-angle consistency is defined in BRF, cloud optical thickness and spherical albedo in three quantities, m_{BRF}, m_{τ}, and m_{β}, given as:

$$m_{BRF} = \sqrt{\frac{1}{n}\sum_{i=1}^{n}\left(\frac{R_j^{sim} - R_j^{obs}}{R_j^{obs}}\right)^2} \times 100\%$$

and

$$m_x = \frac{1}{\langle x_i \rangle}\sqrt{\frac{1}{n-1}\sum_{i=1}^{n}\left(x_i - \langle x_i \rangle\right)^2} \times 100\%,$$

where, R_j^{sim} and R_j^{obs} represent the 3×3 1.1-km-pixel domain mean 866 nm channel BRF simulated for and observed by MISR, respectively, j is the MISR camera index (j = {1, 2, …, 7}), x_i is either the mean cloud thickness or spherical albedo over a domain in the i^{th} MISR camera, and $\langle\ \rangle$ denotes averaging over the seven MISR cameras. In this analysis, *as in Liang et al.* [2009], a 7-MISR-camera registration criterion (7MRC) is used to retain the well registered domains among the seven least oblique MISR images and the MODIS image (hereafter, we refer to these domains as 7MRC domains).

As stated in Chapter 2, such view-angle consistency tests are self consistency tests to examine if the plane-parallel assumption is valid for clouds. A larger (smaller) metric-

value indicates a larger (smaller) chance of the break down of the plane-parallel assumption in both the forward radiative transfer calculations and the inferences of cloud optical proprieties with shortwave radiance measured by a passive satellite instrument.

4.3 Results

Figure 4.1 shows the probability distribution functions (PDF) and cumulative PDFs in the occurrence of m_{BRF} , m_{τ}, and m_{β} for all oceanic water clouds. They reveal, for example, that clouds are angularly consistent in BRF, optical depth and spherical albedo to within 5% of their plane-parallel value 67.6%, 23.0%, and 72.0% of the time, respectively, for January and 61.0%, 23.7%, and 61.3% of the time, respectively, for July. For metric values < 10%, the angular consistency rates increase to 91.7%, 67.8%, and 92.9% for January and 90.0%, 58.9%, and 84.6% for July for m_{BRF}, m_{τ}, and m_{β}, respectively.

While Figure 4.1 shows close similarity for January and July, their regional distributions can be very large. Figures 4.2-4.4 show the frequency (passing rate) in which m_{BRF}, m_{τ} *and* $m_{\beta,}$ < 5% and < 10%, respectively, and Figure 4.5 shows the corresponding total number of the sampled domains. The SZAs at the time of observations, which are tied to the 10:30 AM equator crossing time of Terra's sun-synchronous orbit, are also shown in Figure 4.2. The cut off in data at high latitudes occur because only ice-free oceans are included in our analysis. Clearly, from Figures 4.2-4.4, the spatial distributions of the passing rates appear to be tied to two key factors: the spatial distribution of stratiform clouds and SZA. It has been known for some time that stratiform clouds appear frequently off the subtropical western coasts of continents,

particularly off the coast California, Peru, and Angola, as well as regions of mid- to high-latitude lows [*Warren et al., 2006*]. While high passing rates appear off the subtropical western coasts of continents in both January and July, the mid- to high-latitude lows have high passing rates only in the summer hemisphere, when SZAs are small. Evident is a transition in passing rates as we move from the subtropical stratus to mid-latitude stratus at a SZA ~ 60°. For SZAs > 60°, the passing rates drop to very low values, despite the stratiform nature of the clouds found at these latitudes. These two effects are consistent with known departures from plane-parallel theory, namely broken clouds or clouds with large cloud top height variability leads to enhanced 3-D radiative pathways (i.e., channeling, side illumination, shadowing and leakage), some of which (e.g., shadowing and side illumination) are further enhanced with an increase in SZA [*e.g., Várnai and Marshak,* 2003].

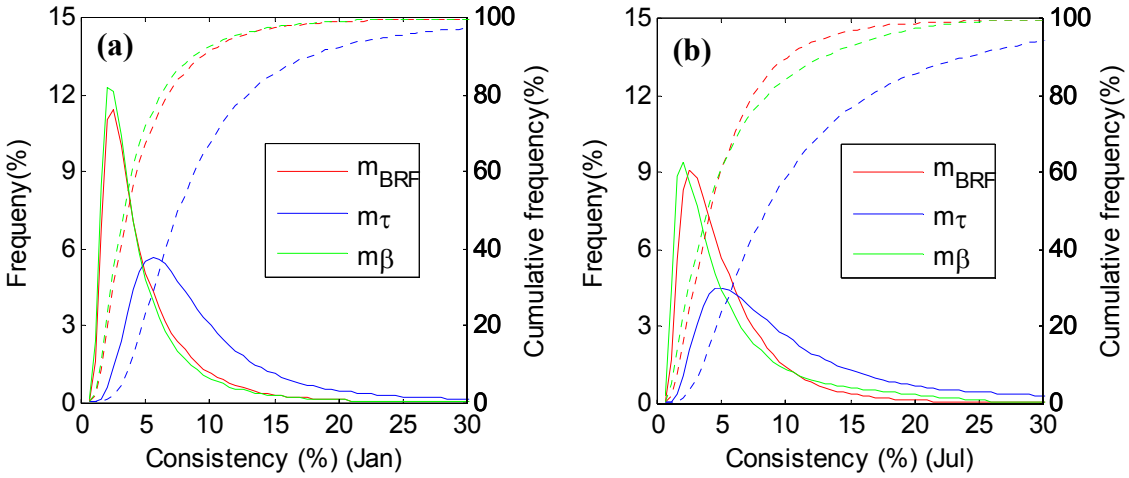

Figure 4.1. *Probability distribution functions (PDFs) and cumulative PDFs for m_{BRF}, m_{τ} and m_{β}, for (a) January and (b) July.*

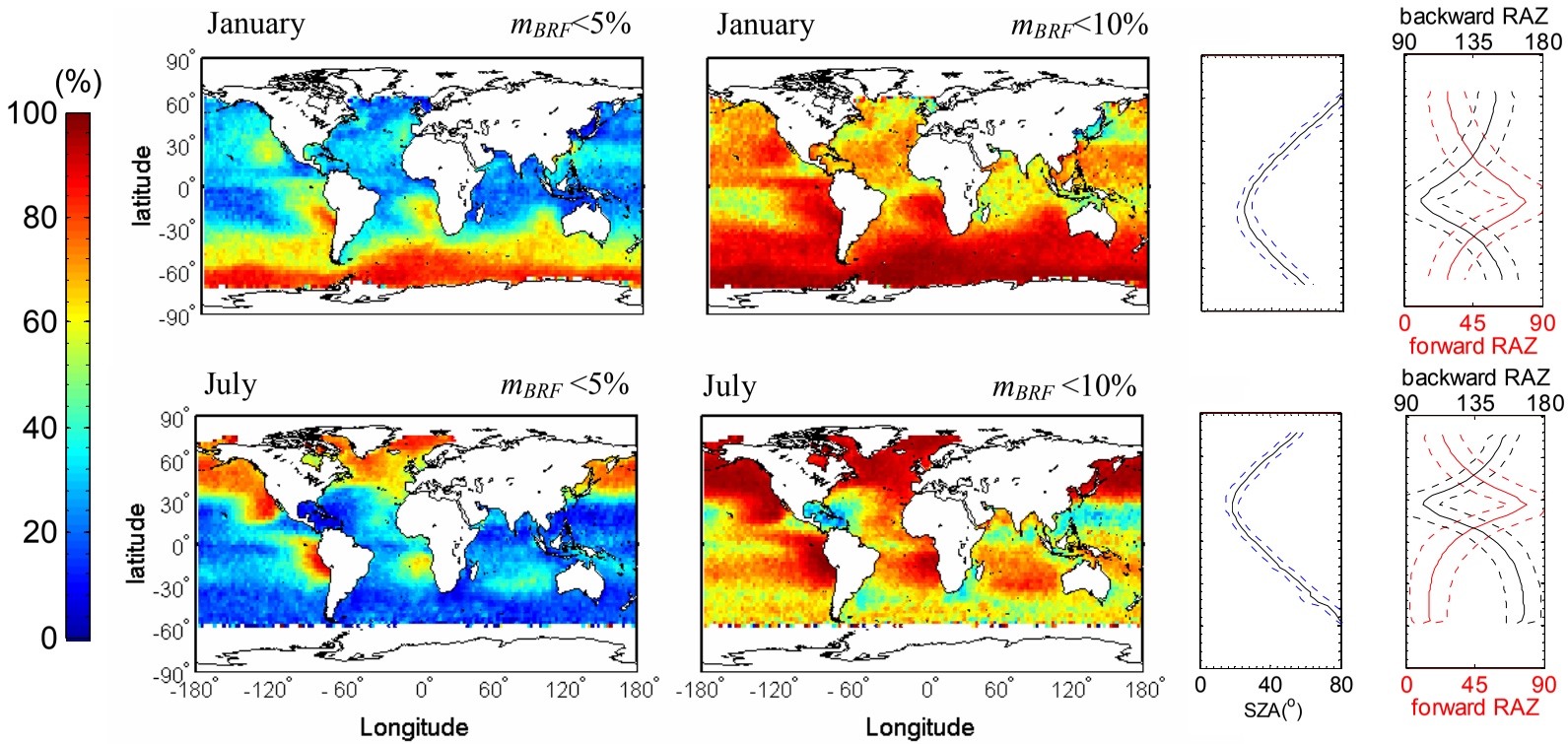

Figure 4.2. *(upper panel) From left to right, view-angle consistency passing rate for m_{BRF} < 5%, m_{BRF} < 10%, mean solar zenith angle (SZA) as a function of latitude (enveloped by the maximum and minimum SZA), and mean relative azimuth angle (RAZ) for the MISR C-cameras in the backward-scatter and forward-scatter directions (enveloped by the maximum and minimum RZA) for January. (lower panel) Same as upper panel but for July.*

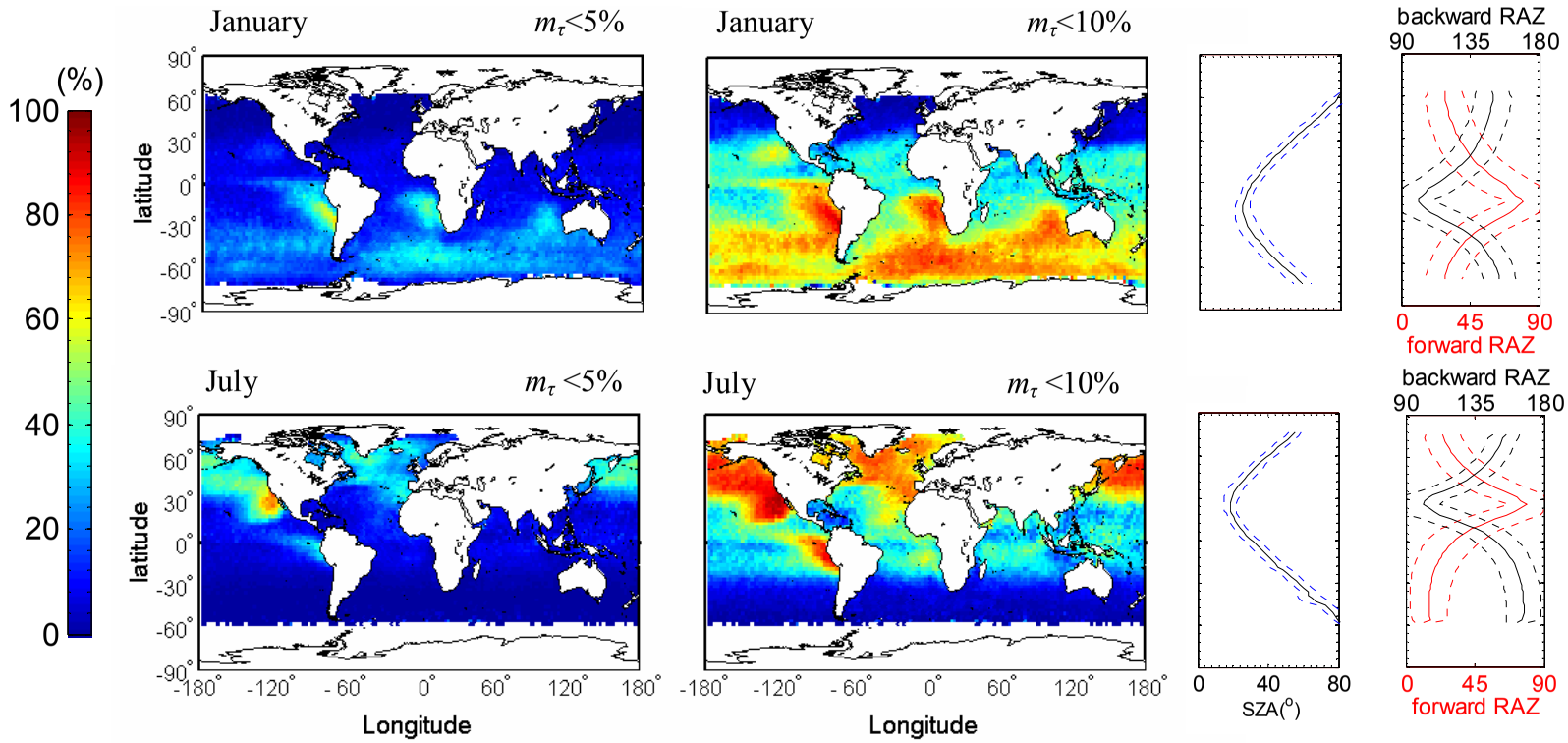

Figure 4.3. *Same as Figure 4.2 but for* m_τ.

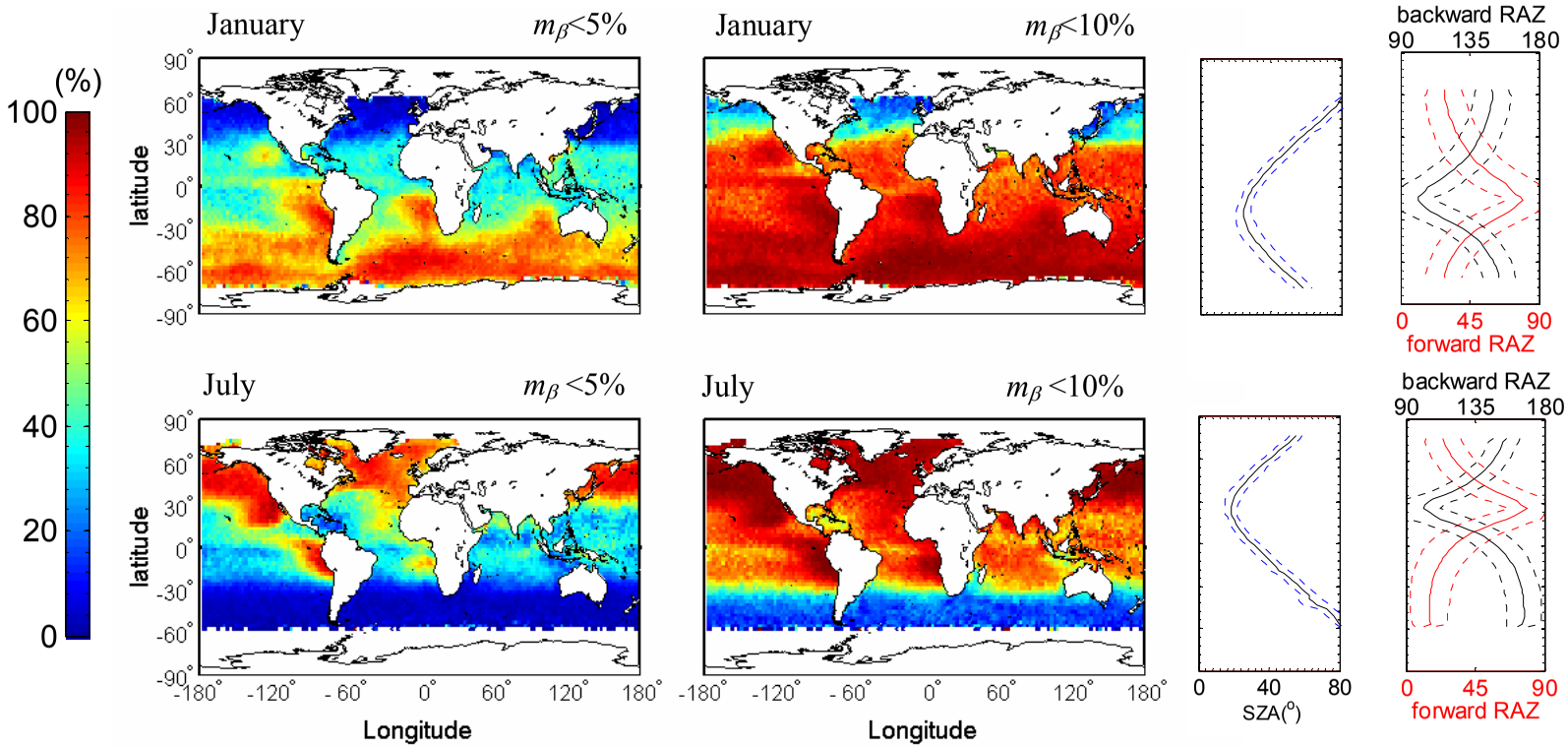

Figure 4.4. *Same as Figure 4.2 but for* m_β.

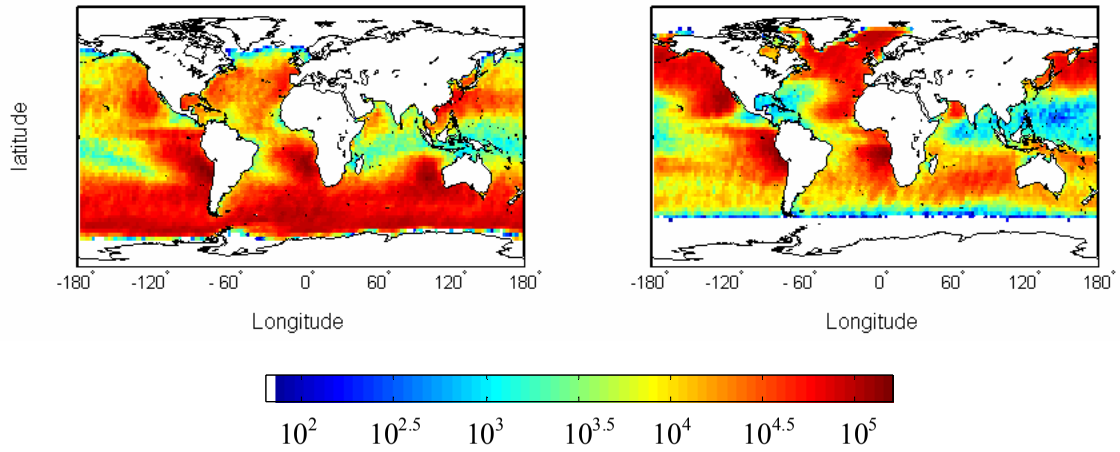

Figure 4.5. *The total number of domains corresponding to the geophysical distribution of the metric passing rates shown in Figures 4.2-4.4 for (a) January and (b) July.*

The metric PDFs presented here are derived from 7MRC cloudy domains (Section 3.3). Applying 7MRC tends to exclude more spatially homogenous clouds as shown in Figure 4.6, where the cloud spatial heterogeneity, H_σ, is defined as in *Liang et al.* [2009]:

$$H_\sigma = \frac{\sigma}{R}$$

where R and σ are the 3 × 3 domain's mean and standard deviation, respectively, for NIR BRF from the 275 m pixels from MISR (near-identical results are had from MODIS). In Chapter 3, we have demonstrated that this skewness produces minor impact for the regional dataset by using a H_σ-bin technique. For our global dataset, as shown in Figure 4.7, the derived metric PDFs for all fully cloudy water domains by using the same H_σ-bin technique and those for the 7MRC domains are nearly identical for all three metrics in both January and July. Table 4.1 also shows that the differences in the metric passing rates at the 5% and 10% thresholds are within 2% in both January and July.

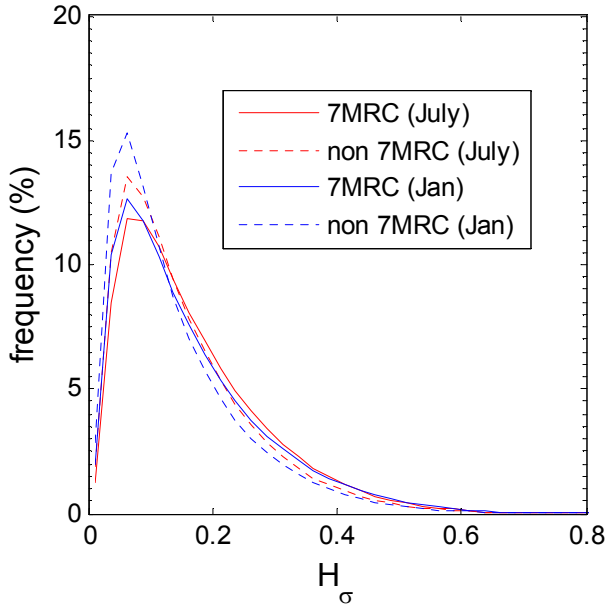

Figure 4.6. *Probability distribution functions of H_σ for the fully cloudy water domains that meet the 7-MISR-camera registration criterion (7MRC) and that fail 7MRC (non-7MRC) for January and July.*

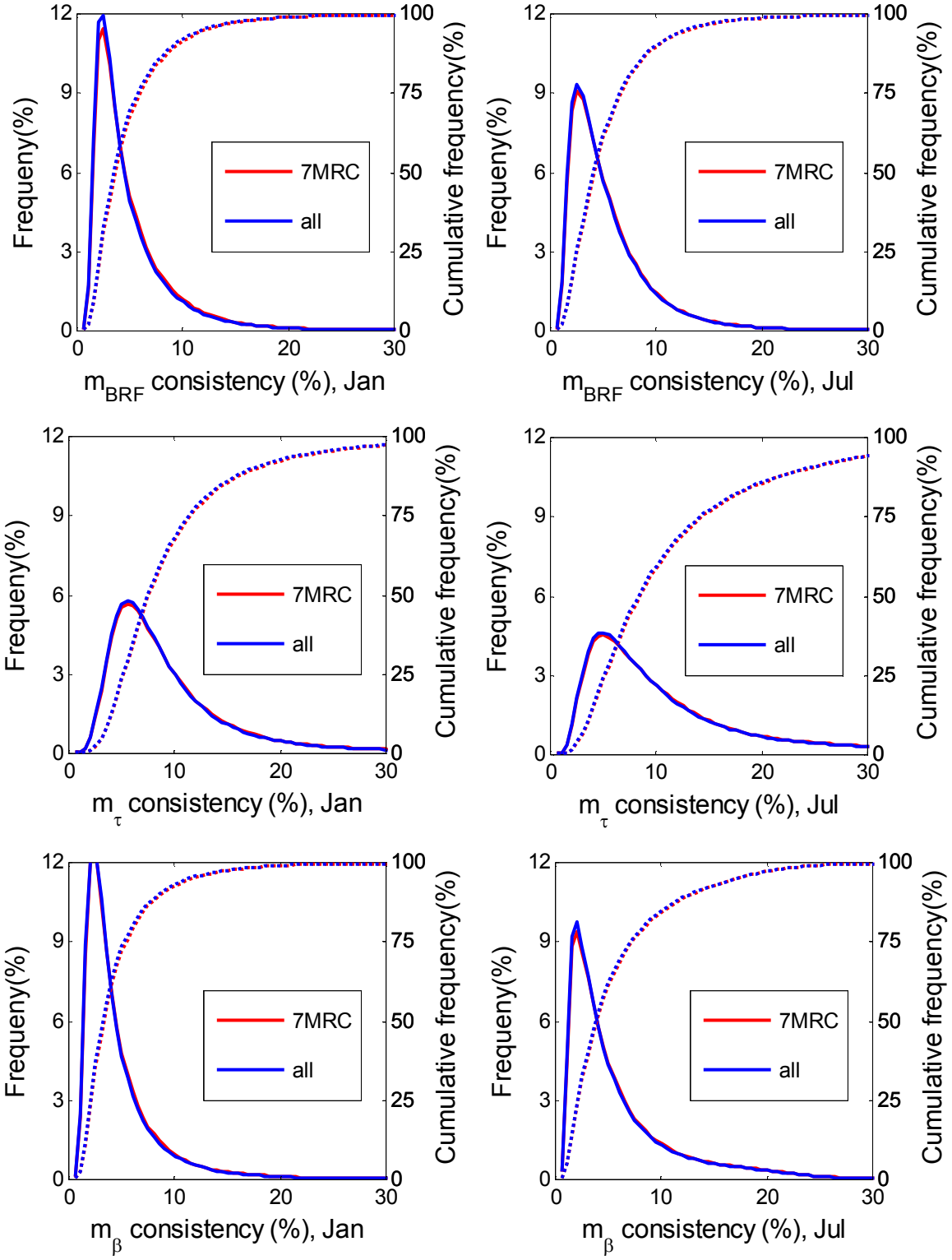

Figure 4.7. *Probability distribution functions of view-angle consistency metrics m_{BRF}, m_{τ}, and m_{β} for 7MRC qualified fully cloudy water domains and that of all fully cloudy water domains for (left column) January and (right column) July.*

Table 4.1. View-angle consistency passing rates of m_{BRF}, m_τ, and m_β for 7MRC qualified fully cloudy water domains and all fully cloudy water domains for 5% and 10% consistency thresholds in January and July.

month	Passing rate threshold	dataset	Passing rate (%)		
			m_{BRF}	m_τ	m_β
January	5%	7MRC	67.6	23.0	72.0
		All	69.4	23.5	73.5
	10%	7MRC	91.7	67.8	92.9
		All	92.3	68.7	93.4
July	5%	7MRC	61.0	23.7	61.3
		All	62.1	24.4	62.4
	10%	7MRC	90.0	58.9	84.6
		All	90.4	59.9	85.0

The connection of angular consistency with the cloud spatial heterogeneity is explored. The distribution of mean H_σ are shown in Figure 4.8. Note that at mid- to high latitudes, clouds have smaller H_σ values (more homogeneous clouds) in the summer hemisphere. A comparison of Figure 4.2, 4.3, 4.4, and 4.8 clearly reveals that larger angular consistency metrics are associated with larger values of H_σ; hence larger deviations from plane-plane occur for larger cloud heterogeneity. This is quantified in Figure 4.9 for m_{BRF}, m_τ and m_β, which show the 2-D distribution between angular consistency metrics and H_σ. As the cloud becomes more spatially heterogeneous within the 3×3 domain (i.e., as H_σ increases), the mode and spread of angular consistency metrics becomes larger. Note that in July, there are clouds that are very spatially homogeneous (H_σ<~0.02) with large view-angle consistency metric values. We investigated this further and found that it occurs only in several days of the data and in

limited regions. It occurs when a layer of smoke overlies cloud. An example is shown in Figure 4.10, where some cloudy pixels overlaid by smoke are flagged by MODIS as water clouds. The smoke reduces BRF spatial variations (very small H_σ), but causes angular inconsistencies (large m_{BRF}) because the scattering properties of a smoke+cloud scene is different from that of the water cloud assumed in the MODIS cloud optical property retrieval algorithm.

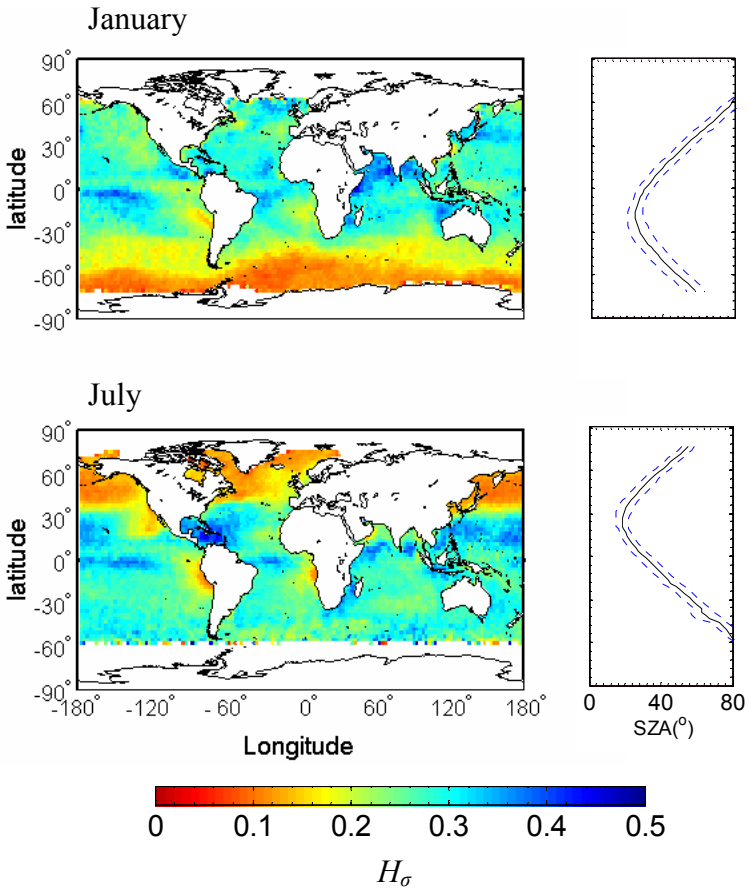

Figure 4.8. *(upper panel) Spatial heterogeneity mean H_σ (left) and mean solar zenith angle (SZA) as a function of latitude (enveloped by the maximum and minimum SZA) (right) for January. (lower panel) Same as upper panel but for July.*

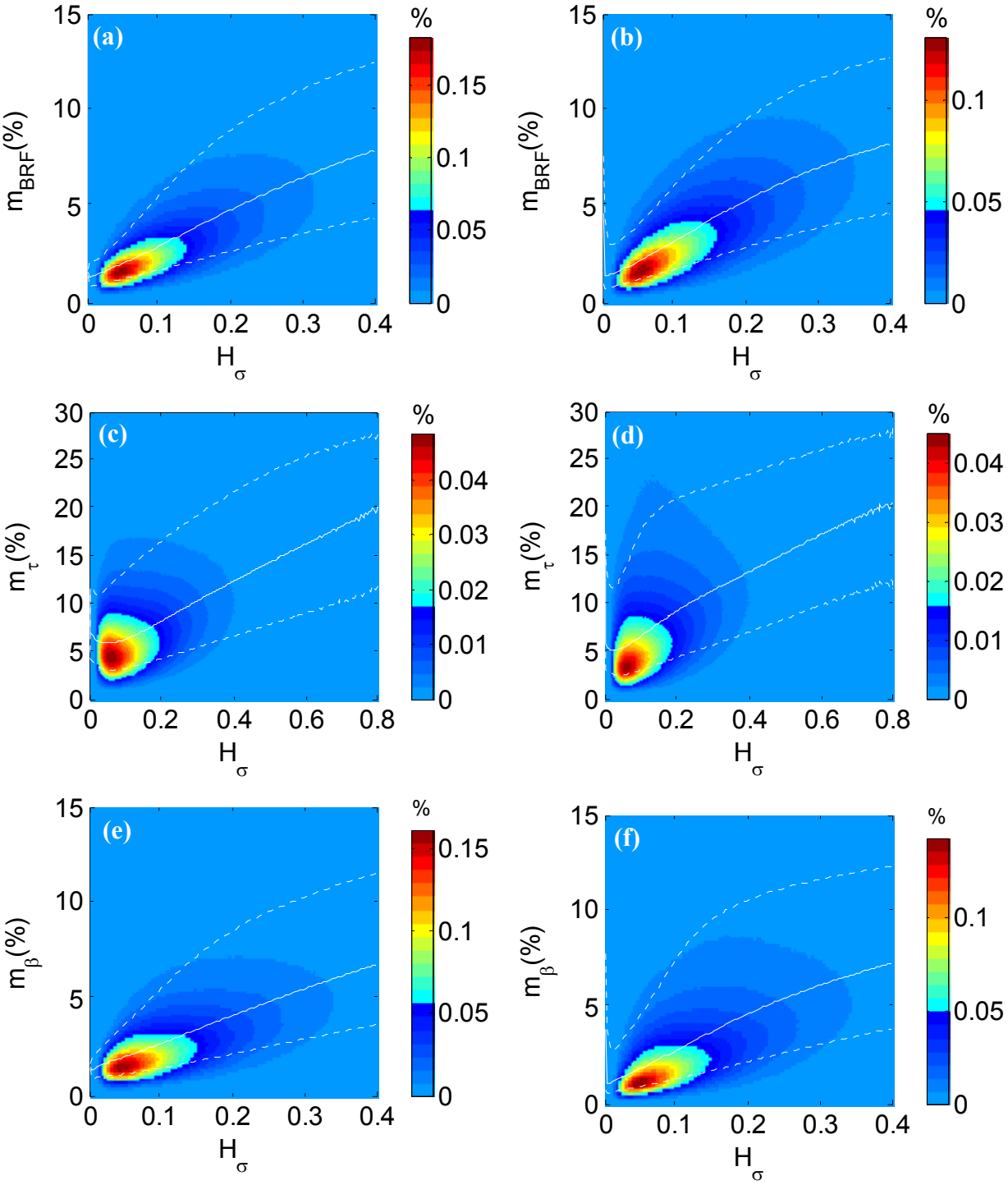

Figure 4.9. *Two-dimensional frequency distributions of H_σ versus m_{BRF} (a) and (b), m_τ (c) and (d), and m_β (e) and (f) in January (left column) and July (right column). Also plotted are the median (solid thick line), 10th and 90th percentile (dotted lines) of the angular consistency metrics computed over H_σ bin intervals of 0.004.*

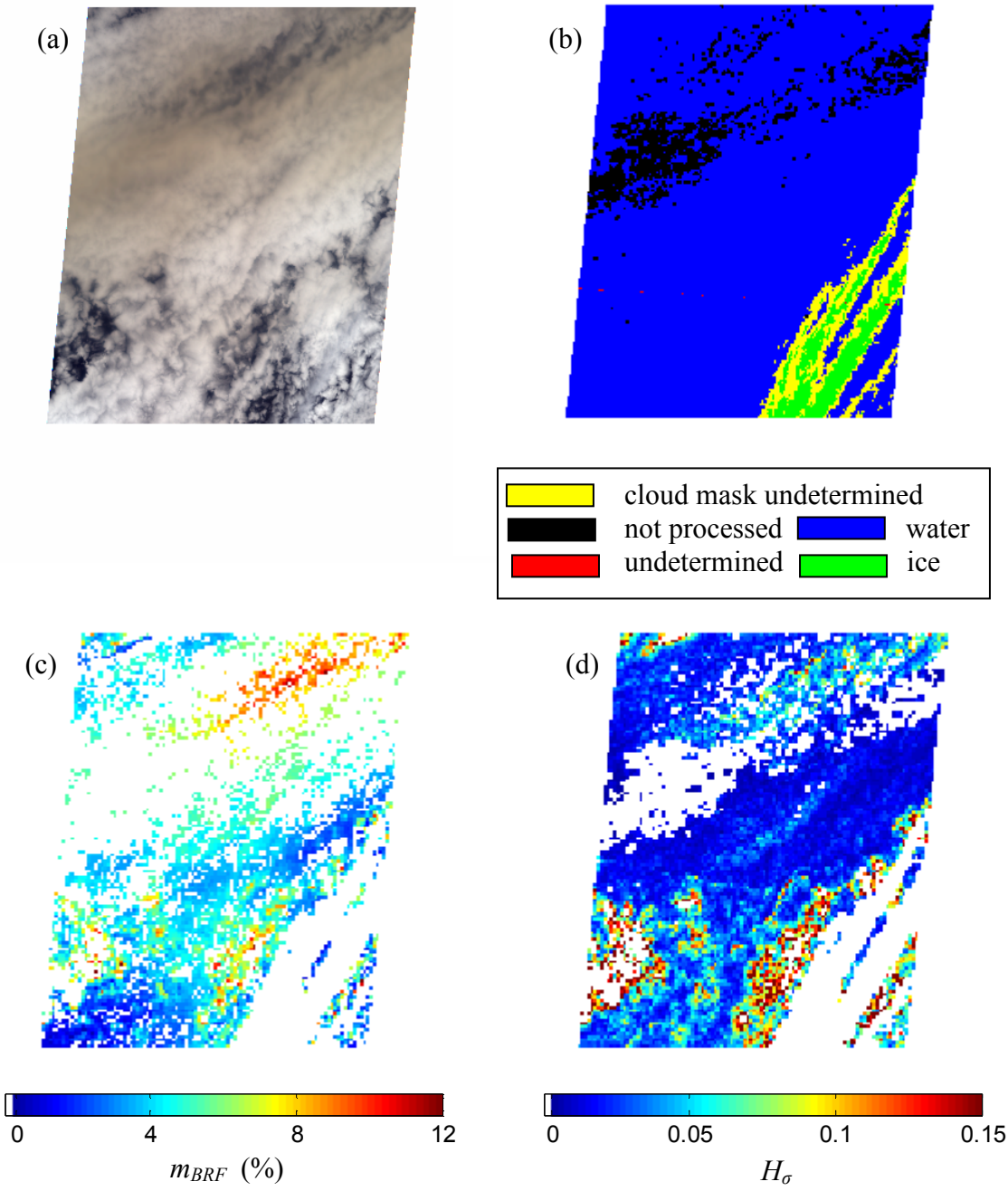

Figure 4.10. *An example of smoke overlaying cloud. (a) RGB image of the scene, (b) MODIS-derived cloud phase, (c) BRF view-angle consistency metric m_{BRF}, and (d) spatial heterogeneity H_σ. Data were collected on 24 July 2004 for Path 076, Orbit 024182, MISR blocks 56-58.*

Analysis of Figure 4.9 reveals that when $H_\sigma < 0.048$ (12.3% of domains meet this criterion for m_{BRF} and m_β and 11.7% for m_τ), m_{BRF} and m_β are <5% and $m_\tau < 15\%$ almost all of the time (with the passing rate of 99.0% for m_{BRF} and m_β and 96.6% for m_τ). For the 10% most spatially homogeneous domains, $m_{BRF} < 5.1\%$, $m_\tau < 19.8\%$, and $m_\beta < 5.1\%$ almost all of the time. For the 10% most spatially heterogeneous domains, m_{BRF}, m_τ, and m_β are < 5% for ~ 22.6%, 3.1%, and 34.9% of the time and < 10% for ~ 80.2%, 30.2%, and 86.2% of the time, respectively. Figures 4.11 also shows the 2-D distribution between the angular consistency metrics and H_σ stratified by SZA. Note that a linear fit through the 2-D distributions provides a fit that is largely insensitive to the SZA. One reason lies in that H_σ is also a function of SZA. Clouds appear smoother under high Sun due to a net horizontal transport of radiation from thicker regions to thinner regions of the cloud [*Zuidema and Evans,* 1998]; whereas they tend to appear more heterogeneous for low Sun due to cloud-side illumination- and shadowing-induced roughening effects [*Várnai and Marshak*, 2003]. The high scatter of H_σ versus view-angle consistency metrics in Figure 4.11 for SZAs greater than 70° suggests that some of the sampled clouds may be mix-phase clouds classified as water clouds, thereby invalidating the assumption of a pure water cloud used in the MODIS retrieval algorithm. Additionally, given that clouds tend to be more view-angularly consistent when measured from side-scatter directions than from directions close to the plane of incidence [*e.g., Kato and Marshak,* 2009; *Section 5.6*] and given that MISR observes clouds close to the side-scatter direction at low latitudes and close to the plane of incidence at high-latitude (see relative azimuth angle in Figure 4.2), clouds are measured to be less heterogeneous in terms of view-angle consistency at low latitudes as compared to that at high-latitudes.

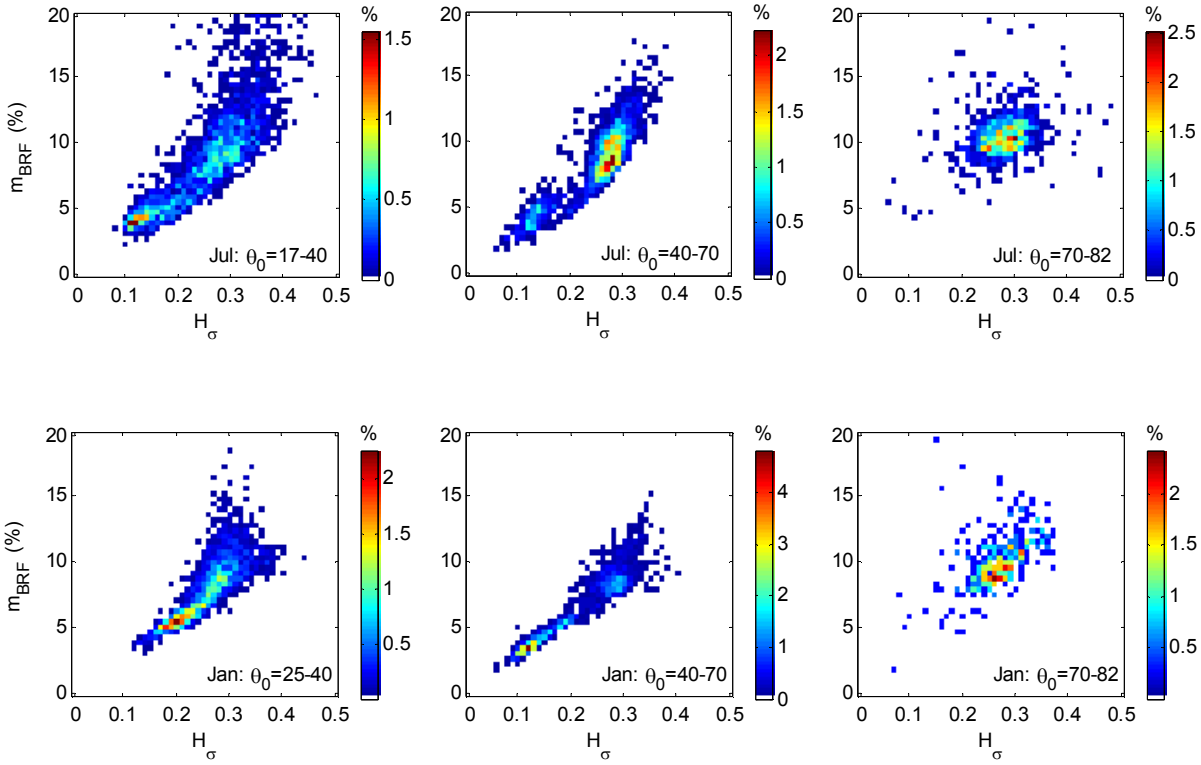

Figure 4.11. *Two-dimensional probability distribution function of gridded-mean H_σ versus gridded-mean m_{BRF} for three solar zenith angle intervals for January (upper panel) and July (lower panel).*

The relationship between the view-angle consistency metrics and the cloud spatial heterogeneity metric allows us to use H_σ to identify pixels that meet any specified requirement for the cloud to be considered plane-parallel. Examples may include (1) requiring 99% of the retrievals to be angularly consistent in BRF to within 5% of their plane-parallel value (i.e., $m_{BRF} < 5\%$), suggests performing retrievals only where $H_\sigma < 0.056$ — 14.4% of domains met this criterion; (2) requiring $m_\tau < 15\%$ for 96.0% of the retrievals suggests performing retrievals only where $H_\sigma < 0.072$ — 22.1% of the domains

met this criteria; and (3) requiring $m_\beta < 5\%$ for 99% of the retrievals suggests performing retrievals only where $H_\sigma < 0.056$ — 14.4% of the domains met this criteria. Since the relationship between H_σ and the angular consistency metrics is largely insensitive to SZA, we can apply H_σ to the historic record of MODIS (on the Terra and Aqua platforms) and other MODIS-like instruments. Placing strict criteria for plane-parallel clouds (e.g., requiring 99% of the retrievals to be angular consistent in BRF to within 5% of their plane-parallel value) allows greater confidence in the microphysical retrievals and their estimate of uncertainty as reported in the MODIS product [*Platnick, et al.,* 2005]. Strict criteria are also required for emerging multi-angle techniques for retrieving cloud microphysical properties that are based on the plane-parallel assumption [*McFarlane et al.,* 2005].

4.4 Relationship with Other Existing Global Cloud Property Climatologies

Because the degree of the observed view-angle consistency relative to plane-parallel indicates the extent to which cloud microphysical properties are reliably retrieved with the plane-parallel assumption, the view-angle consistency also indicates the reliability of other existing scientific results that were derived with the plane-parallel assumption. Two examples are discussed bellow.

The first example is on the cloud radiative susceptibility to the perturbation of the cloud droplet number concentration [*Twomey, 1974*]. This was examined by *Platnick and Oreopoulos* [2008] and *Oreopoulos and Platnick* [2008] on a global scale by calculating the sensitivity of cloud albedo to a change in the cloud droplet number concentration using the MODIS derived climatologies of cloud optical thickness and effective radii.

Comparison between our global map of the view-angle consistency metrics (Figures 4.2-4.4) and the global distribution of the cloud radiative susceptibilities (Figure 4a and 4b of *Oreopoulos and Platnick* [2008], reproduced as Figure 4.12 in this thesis) clearly shows that they are well correlated for SZA <~60º: regions dominated by marine stratiform clouds tend to be associated with low absolute susceptibility values (sensitivity of cloud albedo to a change in the absolute cloud droplet number concentration) and high relative susceptibility values (sensitivity of cloud albedo to a change in the relative cloud droplet number concentration), where clouds are more angularly consistent; the opposite is true for regions dominated by marine cumuliform clouds. For larger SZAs (at high latitudes), both absolute and relative susceptibilities are low and clouds are less view-angular consistent. However, the mechanisms behind these SZA dependences are different. While low values of susceptibility largely originate from the saturated cloud albedo with large [*Platnick and Oreopoulos*, 2008] (that is, a change in cloud droplet concentration could not make any significant difference in cloud albedo change), view-angular consistency dependence on SZA is largely caused by the increased 3-D radiative transfer effects under low Sun. It implies that under low Sun, uncertainties associated with 1-D cloud optical retrievals due to 3-D radiative transfer effects has less of an impact on assessing the cloud albedo susceptibility. However, everywhere else where poor view-angle consistencies exists (e.g., regions dominated by marine cumulus), our confidence in the derived susceptibility are low.

The second example is on using operationally retrieved cloud optical properties to evaluate 1-D radiative transfer calculations in the Global Climate Models (GCMs) where only the grid mean cloud optical properties are available. For example, *Oreopoulos and*

Cahalan [2005] analyzed the spatial heterogeneity of cloud optical thickness at 1º×1º scale based on the MODIS-retrieved cloud optical thicknesses, where such information can be directly used for parameterizing radiative transfer calculations in GCMs. More directly, *Oreopoulos et al.* [2007] analyzed plane-parallel albedo biases of liquid water clouds, also at 1º×1º scale, based on MODIS-retrieved cloud optical thickness and effective radii. Comparing these regional distributions to our regional distributions of the view-angle consistency metrics, large spatially heterogeneous values (or, large cloud albedo bias values), which are measured at regional scales, tend to be associated with large view-angle consistency metrics, which are measured locally; the opposite is true for spatially homogeneous clouds. That is, clouds that are locally heterogeneous are also heterogeneous at regional scale.

Based on these two examples, our results put into question on whether the results from these studies are heavily influenced by the lack of applicability of the plane-parallel assumption over a large fraction of the ocean. However, a thorough analysis on this issue requires a cloud field with known optical properties, which is rarely available, and impossible over the global scale. In the "future work" section of Chapter 6, we propose a synergetic method of using CloudSat observations [*Stephens*, 2002] with the Aqua MODIS observations to estimate the 1-D cloud optical property retrievals without knowing a prior cloud truth.

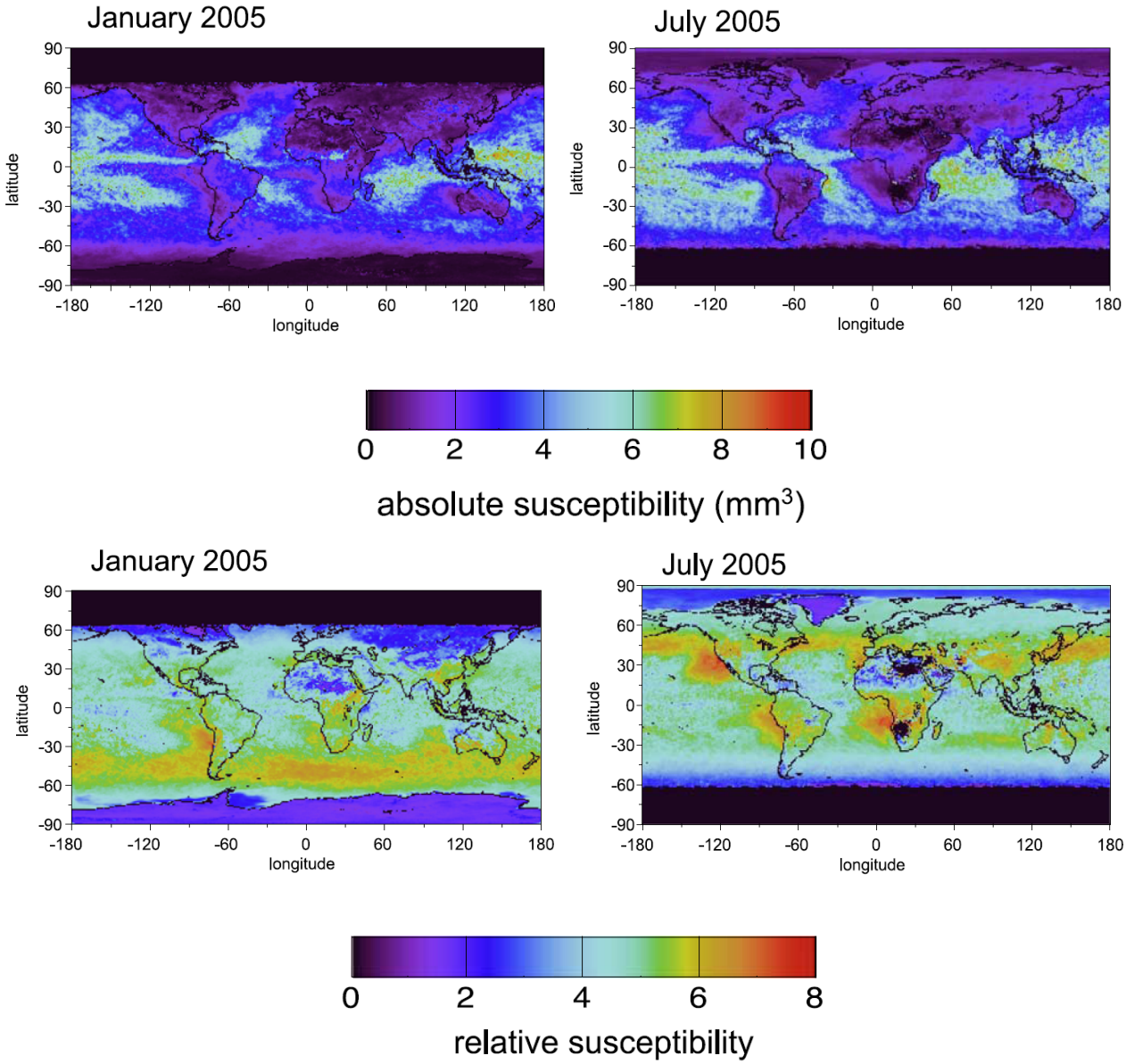

Figure 4.12. *Monthly averages of cloud albedo absolute susceptibility in January (upper left) and in July (upper right) and relative susceptibility in January (bottom left) and in July (bottom right), reproduced from Oreopoulos and Platnick [2008] (Reproduced by permission of American Geophysical union).*

4.5 Implications

The power and utility to identify which pixels have clouds that are plane-parallel is also met with some humility. By any reasonable criterion for the valid use of the plane parallel assumption, only a small fraction of clouds meet the criterion, and those that do tend to lie only within the stratiform regions of the world during times when SZAs are < 60°. Since the spatial and temporal dependence of the invalid use of the plane-parallel assumption is not random, care must be taken when drawing any scientific conclusion from these datasets. This humility also translates into calculations of solar radiative fluxes within models used to make environmental and climate predictions. Even if these models accurately simulate the 3-D distribution of clouds, application of the plane-parallel assumption still would remain questionable over a large portion of the globe and fraction of time. We point to *Barker et al.* [2003] for some understanding that the errors in solar radiative fluxes (hence heating rates) can be unacceptably large.

Given that our ability to accurately compute the interaction of the radiation field with clouds is of great importance in environmental research and the small fraction of clouds that are found to be valid for the application of the plane-parallel assumption to within any reasonable definition, we call to the community for a much more concentrated effort to develop the next generation of operationally viable remote sensing techniques to fully realize the 3-D radiative transfer nature of the problem, and for global models to push towards 3-D radiative transfer to account for the 3-D structure of clouds. The current state-of-the-art in 3-D radiative transfer in dealing with these issues is given in *Marshak and Davis* [*2005*], which suggests that while headways have been made over the past 40 years, we still have a long way to go.

CHAPTER 5:VIEW-ANGLE DEPENDENCE OF CLOUD OPTICAL THICKNESS

In the previous chapter, a global perspective on the applicability of the plane-parallel assumption through view-angle consistency is presented and reveals that a large fraction of oceanic water clouds are not valid by any reasonable criterion. In this chapter, the view-angle dependent biases in retrieved optical thickness caused by evoking the plane-parallel assumption is examined. This chapter is compiled from an article in preparation for submission to *Journal of Geophysical Research* titled "*A global analysis on the view-angle dependence of plane-parallel oceanic water cloud optical thickness using data synergy from MISR and MODIS"*. The detailed descriptions of the data fusion method is described in Chapter 2. The descriptions of data and instruments are retained in this chapter to make this chapter self-contained and true to the article that is in preparation.

5.1 Introduction

Cloud optical thickness (τ) is a key variable required in climate research [e.g., *Schiffer and Rossow,* 1985]. It is routinely retrieved from satellite-measured radiance by assuming the clouds and the imposed radiative boundary conditions to be horizontally homogeneous. This assumption, often referred to as the plane-parallel assumption, reduces the radiative transfer from three dimensions (3-D) to one dimension (1-D; the vertical direction), thus making the inversion of τ from satellite-measured radiances

tangible given other assumptions (e.g., the vertical homogeneity of the cloud layer). Since τ is defined as the volume extinction coefficient integrated over the geometric depth of the cloud, its value at a particular location and time should be independent of solar and view geometries under which retrievals are conducted. Numerous studies, however, have shown that satellite-retrieved τ do carry systematic errors that depend on solar and view geometries, thus limiting the utility of satellite-retrieved τ in studying the energy and water cycles within our climate system. These systematic errors have been traced to two key issues, namely, the nonlinear relationship between τ and radiance applied to an area average radiance measured within a satellite instantaneous field-of-view (IFOV) over which clouds are horizontally heterogeneous [e.g., *Harshvardhan and Randall*, 1985*; Marshak et al*., 2006; *Zinner and Mayer*, 2006], and 3-D radiative transfer effects arising from the horizontal heterogeneity of clouds [*e.g., Davies*, 1978; *Welch and Wielicki* 1984; *Kobayashi,* 1993; *Barker* 1994; *Loeb and Davies,* 1996, 1997; *Loeb and Coakley,* 1998; *Várnai and Marshak*, 2003; *Kato et al.,* 2006; *Várnai and Marshak*, 2007]. The following three points summarize the key findings on this issue:

(1) When the satellite retrieval of τ is performed at nadir for overhead Sun, 2-D and 3-D Monte Carlo radiative transfer simulations through horizontally heterogeneous cloud fields have shown that the retrieved τ will be lower than the truth [*e.g., Kobayashi,* 1993; *Zuidema and Evans,* 1998; *Kato et al.,* 2006; *Kato and Marshak*, 2009]. The underestimation was mainly attributed to the horizontal leakage of radiation from cloud-sides, in addition to the nonlinear relationship between τ and radiance whenever such relationship is of a concave shape.

(2) Such τ underestimation can be reduced to some extent when the satellite retrieval of τ is performed at nadir for moderately oblique Sun, but an overestimation in τ could happen for very oblique Sun. This is based on satellite observations [*e.g., Loeb and Davies,* 1996, 1997; *Loeb and Coakley,* 1998] and confirmed by 2-D and 3-D Monte Carlo radiative transfer model simulations [*e.g., Zuidema and Evans,* 1998; *Várnai and Davies,* 1999; *Kato et al.,* 2006], which have shown that τ increases with increasing solar zenith angle (SZA). It occurs largely because cloud-sides (in the case of clouds with a flat top and τ varying in the horizontal direction, it is the boundary of clouds with larger τ-value) have a greater opportunity to intercept more solar radiation for larger SZAs, leading to greater radiance leaving cloud-top [*Loeb et. al.,* 1997] and a reduction of horizontal leakage of radiation from cloud-sides relative to overhead Sun [*Fu et al.,* 2000].

(3) More complicated is when the satellite retrieval of τ is performed using an oblique view under oblique Sun. Using observations of marine stratus from Advanced Very High Resolution Radiometer (AVHRR) observations, *Loeb and Coakley* [1998] reported that τ decreases with increasing view-angle by more than 40% relative to nadir in forward-scatter directions (i.e., for relative azimuth angles between solar and viewing directions within 0 to 90°) for SZA>~50°, while in backscatter directions (i.e., for relative azimuth angles between solar and viewing directions within 90° to 180°) τ increases marginally with view-angle. These observed behaviors were later supported by 3-D radiative transfer simulations [*e.g. Loeb et al.,* 1998; *Kato and Marshak,* 2009]. In contrast, *Várnai and Marshak* [2007] used Moderate Resolution Imaging Spectroradiometer (MODIS) observations and showed that τ increases with viewing

obliquity in both forward-scatter and backscatter directions: τ can be more than 40% higher at VZA=60° compared to VZA=0° when SZA>60°. The authors suggested that the likely reasons for the increasing of τ with view-angle lie in 3-D radiative transfer effects and the viewing of cloud-sides with relative azimuth angle ranging from 60° to 70° (110° to 120°) in forward-scatter (backscatter) direction, and pointed out that similar behaviors were found in model simulations [*e.g., Davies,* 1984; *Bréon,* 1992; *Kobayashi*, 1993]. Adding to these contrasting results were 3-D radiative transfer simulations by *Kato et al.* [2006], showing that the scene-averaged τ decreases in both forward-scatter and backscatter directions for all azimuth angles; no explanation was given for this behavior.

These contrasting results clearly suggest that the retrieved-τ with the plane-parallel assumption for real clouds is a complex function of sun-view geometry that is not fully understood. We also tend to lack a global perspective since most observational studies were performed only in specific regions. For example, *Loeb and Davies* [1996] examined SZA dependence of τ with 1-yr ERBS observations over ocean between 30ºS and 30ºN, and *Loeb and Coakley* [1998] examined VZA dependence of τ with one month of AVHRR observations of marine stratus over the coasts off California, Peru, and Angola. Only recently, did *Várnai and Marshak* [2007] examine the VZA dependence of τ with 1-yr global observations from MODIS.

Common to all these observational studies is the use of wide-swath scanning instruments, resulting in a narrow range of relative azimuth angles and only one view-angle observing a given location within the instrument swath. Examining the sun-view bias of retrieved-τ with these instruments requires some assumptions: (1) clouds are diurnally, seasonally or latitudinally invariant, depending on the orbital configuration,

when examining the solar-angle dependence of τ, (2) clouds are latitudinally invariant when examining the view-angle dependence of τ retrieved from a sun-synchronous orbit, and (3) clouds analyzed in different viewing directions are statistically consistent with respect to cloudy scene identification and the size of ground instantaneous field-of-view (GIFOV). We will discuss these three assumptions in greater detail in Section 5.2.

In this study, we overcome many of these assumptions, as detailed in Section 5.2, with near-simultaneous, multiple-angle observations of clouds from the Multiangle Imaging SpectroRadiometer (MISR) along with fused observations from MODIS. We present an analysis of SZA-binned view-angle dependence of 1-D retrieved τ over the globe based on 8 years of oceanic water cloud observations for the months of January and July, providing ample sampling and seasonal characterization. Our analysis corroborates many of the observed behaviour of 1-D retrieved τ measurements with sun-view geometry found amongst those studies, and explains the reasons behind some of the contrasting results found in previous studies. The near-simultaneous views of the same scene from MISR, which allows for stratification of the data by cloud optical thickness and spatial heterogeneity, and the extension to a greater range of sun-view geometries reveal a greater complexity yet to be observed or examined.

The outline of this chapter is as follows. Section 5.2 discusses three assumptions for global studies of sun-view dependence of 1-D retrieved-τ with wide-swath scanning satellite instruments and how MISR observations overcome many of these assumptions. Section 5.3 describes the data and instruments used in our study. The methodology is given in Section 5.4 and Section 5.5 gives the analysis of the SZA-binned view-angle dependence of τ. A summary and discussion are given in Section 5.6.

5.2 Assumptions

5.2.1 Solar Zenith Angle Dependence

The assumptions used in examining the SZA dependence of 1-D retrieved τ from a given direction depend on the orbit of the satellite. With a sun-synchronized satellite, the SZAs sampled at a particular location is narrow over the course of a month, but can be quite large over the course of a year, as demonstrated in Figure 5.1a for local noon sampling at 30°S. If we set out to determine the SZA dependence of τ retrieved at nadir at a particular location on 30°S, we could fit a line to a scatter plot of retrieved τ versus SZA. However, in so doing we assume that the clouds are seasonally invariant, that is, following Figure 5.1a, the true cloud properties in February (SZA ~ 10°) are statistically the same as in May (SZA ~ 40°). If cloud properties do depend on season, then it becomes impossible to decouple SZA effects on 1-D retrieved τ from the true underlying changes in the cloud properties with season. Alternatively, we could fit a line to a scatter plot of retrieved τ versus SZA for a given day by including data over a wide range of latitudes. However, in so doing we assume that clouds are latitudinally invariant. Unfortunately, further annual or zonal averaging does still require clouds to be latitudinally invariant; the observations of τ at a particular SZA are sampled over the course of a year only over a certain range of latitudes. For example, as shown in Figure 5.1b for noon sampling, observations of τ with SZA = 15° can only be found between 35°N and 35°S, whereas observations of τ with SZA = 60° can only be found within 30°S -80°S and 30°N-80°N. If cloud properties do depend on latitude, then it becomes impossible to decouple SZA effects on 1-D retrieved τ from the true underlying changes

in the cloud properties with latitude. Since cloud properties do depend on latitude and season, we cannot determine the SZA dependence of τ retrieved from an instrument in a sun-synchronous orbit. Since the MISR and MODIS instruments used in our study (Section 5.3) are on the Terra satellite platform, which is in a sun-synchronous orbit, we make no attempt at assessing the 1-D retrieved τ dependence on SZA.

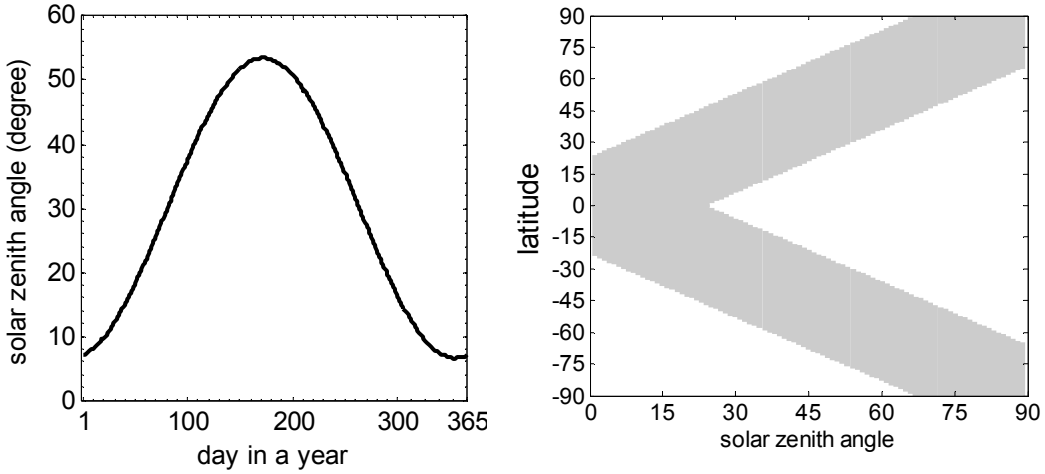

Figure 5.1. *(a) Solar zenith angle in a year for 30°S latitude at 12:00 PM local time. (b) Latitude range (gray-shaded area) as a function of solar zenith angle over a year for 12:00PM local time. For example, observations with SZA=15° can only be found within ~±35° during a year.*

An instrument in a sun-precessing orbit can observe clouds at various local times (hence various SZAs) over the same region, typically over a one to three month period. Cloud property invariance over this time period is required for assessing the 1-D retrieved τ dependence on SZA over a region. Also, required is diurnal invariance. Strictly speaking, obtaining a true τ dependence on SZA is made possible as long as clouds are evenly sampled in location, season and time of day for all SZAs; otherwise, the natural latitudinal, seasonal and diurnal variations are coupled with τ-SZA. In doing

so, the obtained τ-SZA is not particular for a specified location, season or local time, but for the combination of them. In addition, an examination of τ-SZA over the full range of SZA is only possible at low latitudes, since small SZAs would be missing from the analysis over high latitudes. *Loeb and Davies* [1996] took these issues into consideration when deriving the SZA dependence of τ from the Earth Radiation Budget Satellite (ERBS).

5.2.2 Viewing Zenith Angle Dependence

Sun-synchronous, wide-swath scanning instruments, such as MODIS and AVHRR, have been used to examine the VZA dependence of 1-D retrieved τ [*Loeb and Coakley,* 1998; *Várnai and Marshak*, 2007]. The wide swath of these instruments provides a moderate range in VZA across the scan that is approximately perpendicular to the orbital direction. To avoid the dependence of 1-D retrieved τ on SZA, τ-VZA relationships are derived by binning the retrieved τ and associating them to VZA within narrow SZA bins. It has thus far gone unnoticed that such an approach for establishing a τ-VZA relationship also assumes cloud properties to be latitudinally invariant. For example, Figure 5.2 shows the geographical distribution of VZA and SZA of one daytime orbit from MODIS. We see that a given SZA bin can span a fairly wide range of latitudes (e.g., a SZA=56°-60° bin spans 22.5°S to 33°S; a SZA=18°-26° bin spans 7.5°N to 45°N). Thus comparing retrieved τ for different VZA within a SZA bin is to also compare retrieved τ over different latitudes. Thus, τ-VZA obtained in this way is distorted by natural cloud latitudinal variations rather than solely indicating a SZA-binned τ-VZA relationship.

The latitudinal invariant assumption can be avoided for instruments in a sun-precessing orbit, like ERBS, by restricting the analysis of τ-VZA at a particular latitude and within a given SZA bin. This is achieved by collecting retrievals for one VZA from orbits with one equator-crossing time and for another VZA from orbits with another equator-crossing time when SZAs are the same. However, this may take a long time to achieve significant sampling for the analysis, thus requiring cloud property invariance over the long time scale.

In this study, we avoid the seasonal and latitudinal cloud property invariance assumptions by using data from MISR to examine the SZA-binned τ-VZA relationships. This is possible because we can observe the same cloud from multiple viewing directions within minutes of each other (Section 5.3), thus all under the same SZA. This also allows us to bin the data by the observed nadir cloud properties, such as optical thickness and horizontal spatial heterogeneity (Section 5.4).

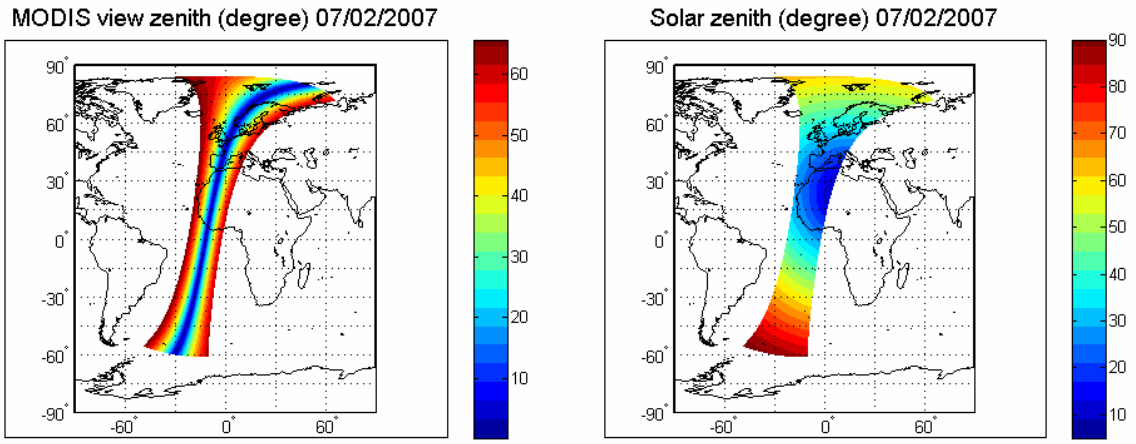

Figure 5.2. *(a) MODIS view zenith angle and (b) solar zenith angle for daytime observations taken on 07/02/2007 of the Terra path 200, orbit 40092.*

5.2.3 Scene Identification and GIFOV Expansion with Viewing Zenith Angle

In developing τ-VZA relationships, comparing τ for cloudy scenes from one view to that from another view implicitly requires that the two sets of cloudy scenes are the same. One of the limitations in using wide-swath scanning instruments lies in that cloudy scenes identified across multiple view-angles may not be consistent in their properties. For example, a scene that is classified as partly cloudy at nadir may be classified as fully cloudy in an oblique view [e.g., *Minnis,* 1989; *Zhao and Di Girolamo,* 2004]. Even our sensitivity limit in detecting thin clouds depends on view angle [*e.g., Zhao and Di Girolamo,* 2004]. These problems are exasperated by the expansion of the GIFOV with viewing obliquity that occur for wide-swath scanning instruments. For example, pixels in ERBS expand from ~1500 km^2 in near-nadir directions to ~ 82500 km^2 at the limb [*Loeb and Davies,* 1996, 1997], 1-km^2-pixels derived from 250m-pixels in MODIS expand from ~1 km^2 in near-nadir directions to ~ 2.4 km^2 for VZA=55º based on the expansion factor of 2.01 in the along-track direction and 4.83 in the cross-track direction [*Nishihama et al.,* 1997], and the Global Area Coverage pixels of AVHRR expand from ~4.4 km^2 in near-nadir directions to ~52.8 km^2 for VZA=~68° [*Loeb and Coakley, 1998*]. An additional complication is that the 1-D retrieved τ is also a function of the size of the pixel's GIFOV when clouds are not plane-parallel. For example, several studies [e.g., *Zuidema and Evans*, 1998; *Várnai and Marshak,* 2001] have shown that the retrieved-τ decreases as the pixel size increases from several hundred meters to several tens of kilometers.

These problems, however, are minimal in our study. In this study, the cloudy scenes for analysis in multiple-views are solely classified based on the nadir view. The multiple views from MISR are registered to the nadir view so that cloudy scenes are consistent for multiple-views. In addition, the size of a MISR pixel's GIFOV expands very little with view-angle due to instrument design. As shown in *Zhao and Di Girolamo* [2004], the GIFOV expands from 1.1 km × 1.1 km at nadir to 1.1 km × 1.53 km at its most oblique view (70.5º), where the expansion only takes place in the along-track orbital direction.

5.3 Data and Instruments

MISR, onboard the Terra satellite platform, provides nine views of the same scene on the Earth within seven minutes from its multi-camera pushbroom design. Details of the instrument and instrument performance are described in *Diner et al.* [1998]. In brief, one camera views at nadir (nominal VZA of 0°) and is designated AN. Four cameras, designated AF, BF, CF and DF, point forward along the orbital track at VZAs of 26.1°, 45.6°, 60.0° and 70.5°, respectively. Four other cameras, designated AA, BA, CA, and DA, point aft along the orbital track at VZAs of 26.1°, 45.6°, 60.0° and 70.5°, respectively. Radiances are measured in 4 narrow-band spectral channels (446 nm, 556 nm, 667 nm, 866 nm), with a ground sampling resolution varying from 275 m to 1.1 km, depending on the channel and camera. Sampling is done over a swath of ~ 400 km.

Version 24 of the MISR 866 nm radiances are converted to the bidirectional reflectance factors (BRFs) using

$$BRF = \frac{\pi L_{866}}{\cos(SZA) F_0},$$

where L_{866} is the radiance measured by MISR and F_0 is the solar irradiance (as reported in the MISR radiance file) corrected to the Sun-Earth distance at the top of the atmosphere. The sun-view geometries at 17.6 km resolution are linearly interpolated to 1.1 km resolution from Version 13 of the MISR Geometric Parameters product. Only clouds over ocean are considered, where ocean is identified based on Version 24 of the MISR Ancillary Geographic Product (AGP). The AGP file also provides the latitude and longitude for each 1.1 km Space-oblique Mercator (SOM) grid on the World Geodetic System 1984 ellipsoid surface. Clouds over sea-ice are excluded based on the sea-ice flag in Version 3 of the MISR Terrestrial Atmosphere and Surface Climatology data.

MODIS [*Barnes et al.* 1998], also onboard Terra, measures radiance in 36 spectral channels, ranging in wavelength from 0.4 μm to 14.4 μm over a swath of ~2300 km. The ground sampling resolution ranges from 250 m to 1 km in the near-nadir directions, depending on the spectral channel. The central portion of the MODIS swath completely overlaps with the MISR swath. The effective radii (r_e) of the cloud drop size distribution and τ are retrieved through daytime multi-spectral reflected solar radiances [*Platnick et. al.,* 2003]. Only water clouds were considered based on the cloud phase flag (MOD06 product). Brightness temperature at the cloud-top is calculated from 11 μm thermal emission (MOD02 product) to characterize the cloud top height heterogeneity (Section 5.5). Latitude and longitude (MOD03 product), in conjunction with MISR latitude and longitude, are used for projecting MODIS data at 1 km resolution to the

MISR SOM grid at 1.1 km resolution (Section 5.4). All MODIS products used in this study are from Collection 5 data.

Terra is in a sun-synchronous orbit with an equator-crossing time of ~10:30 AM LST. As such, the range of SZA and solar azimuth angle observed at a particular location on Earth by MISR and MODIS are narrow and fixed. We use MISR and MODIS data collected over the globe in January and July between 2001 and 2008 in order to sample the boundaries of this range, as well as to capture seasonal differences in cloud cover.

5.4 Methodology

Given a cloudy scene and its observations from MISR and MODIS, we require data fusion between the cloud optical properties retrieved from MODIS and the BRF measurements from MISR. This is achieved by registering the cloudy scene in multiple images of MISR and MODIS with the method described in full in *Liang et al.* [2009]. In brief, to minimize the registration errors, registration is performed on each individual cloudy domain consisting of 3×3 1.1-km pixels, rather than at the single 1.1-km pixel-level. MODIS products, such as τ, r_e and cloud phase, are first projected on the MISR SOM grid at 1.1 km resolution. If all 1.1-km pixels in a 3×3 pixel domain within a MISR AN-camera image have valid MODIS τ and r_e retrievals and are flagged as water phase, then the domain is registered in the MISR oblique camera images to obtain its MISR BRF measurements. However, it is more difficult to reliably register a cloudy domain in the more oblique camera images, largely because the texture of clouds change with viewing obliquity. We apply the registration quality control procedure of *Liang et al.* [2009] to all nine MISR cameras. This results in ~48.2% (51.4%) of all fully cloudy

domains, flagged as water phase, in the months of January (July), to be registered as a complete set of all nine cameras. It is these domains that we include in our analysis, thus our results are conditional upon this sampling.

As in *Liang et al.* [2009], τ is retrieved with MISR-measured 866 nm BRF and MODIS-retrieved r_e with the same 1-D radiative transfer model used to construct the look-up tables for the standard (MOD06) MODIS cloud microphysical retrievals [*King et al.,* 1997; *Platnick et al*., 2003]. All assumptions between the MODIS standard cloud microphysical retrieval algorithm and the one used here are identical (e.g., a modified gamma distribution is assumed for the cloud drop size distribution and the ocean surface is assumed to be Lambertian with a BRF = 0.05). To reduce the uncertainties arising from retrieved τ that are nearly saturated, we further exclude a cloudy pixel from all nine views if its retrieved-τ in any camera-view is greater than 100.

We bin the data into a series of narrow zonal bands with a 2.5°-width to characterize the view-angle dependence of τ from one latitude to another. Such narrow-latitude bins also lead to a narrow SZA range for one-month-long observations. Taking the observations in July as an example, the difference between the largest and smallest SZA as a function of latitude ranges from 2.7° to 13.5°, depending on the latitude bin, and within 10° for most latitude bins. Figures 5.3 and 5.4 show example characteristics of the azimuth angle of MISR cameras at particular locations and time. Figure 5.3 gives the typical azimuth ranges of the Sun and MISR cameras observed across the MISR swath at three representative latitudes. At high latitudes, MISR views clouds in directions close to the plane of incidence in both forward-scatter and backscatter directions; at low latitudes, it views clouds in directions close to the normal of the plane of incidence (i.e., side-

scatter). These changes in azimuth angle are coupled with smaller SZAs over low latitudes and larger SZAs over high latitudes. Also note that the range of MISR azimuth angles become narrower for more oblique cameras, and that the more oblique cameras completely lies within the less oblique camera in azimuth angle range (except the AN camera). The arrows indicate the direction in which the azimuth angle changes across the MISR swath from the western side to the eastern side for the four forward cameras and four aftward cameras, the AN camera and the Sun. Also, over high latitudes in the northern hemisphere, all cameras pointing forward along the orbital track take observations in the backscatter directions and all cameras pointing aftward along the orbital track take observations in the forward-scatter direction; the opposite is true over high latitudes in the southern hemisphere. Thus, the data are naturally divided into 10 camera-view bins within each latitude bin: one bin for each of the five MISR cameras (AN-camera, A-, B-, C- and D-camera) that measure forward-scattered radiance, and one for each of the five MISR cameras (AN-camera, A-, B-, C- and D-camera) that measure backscattered radiance. Figure 5.4 shows the range of relative azimuth angle (RAZ) between viewing and solar direction for each MISR camera-view, as a function of latitude, in the forward-scatter and backscatter directions in January and July. It also shows that RAZ becomes narrower for larger viewing obliquity.

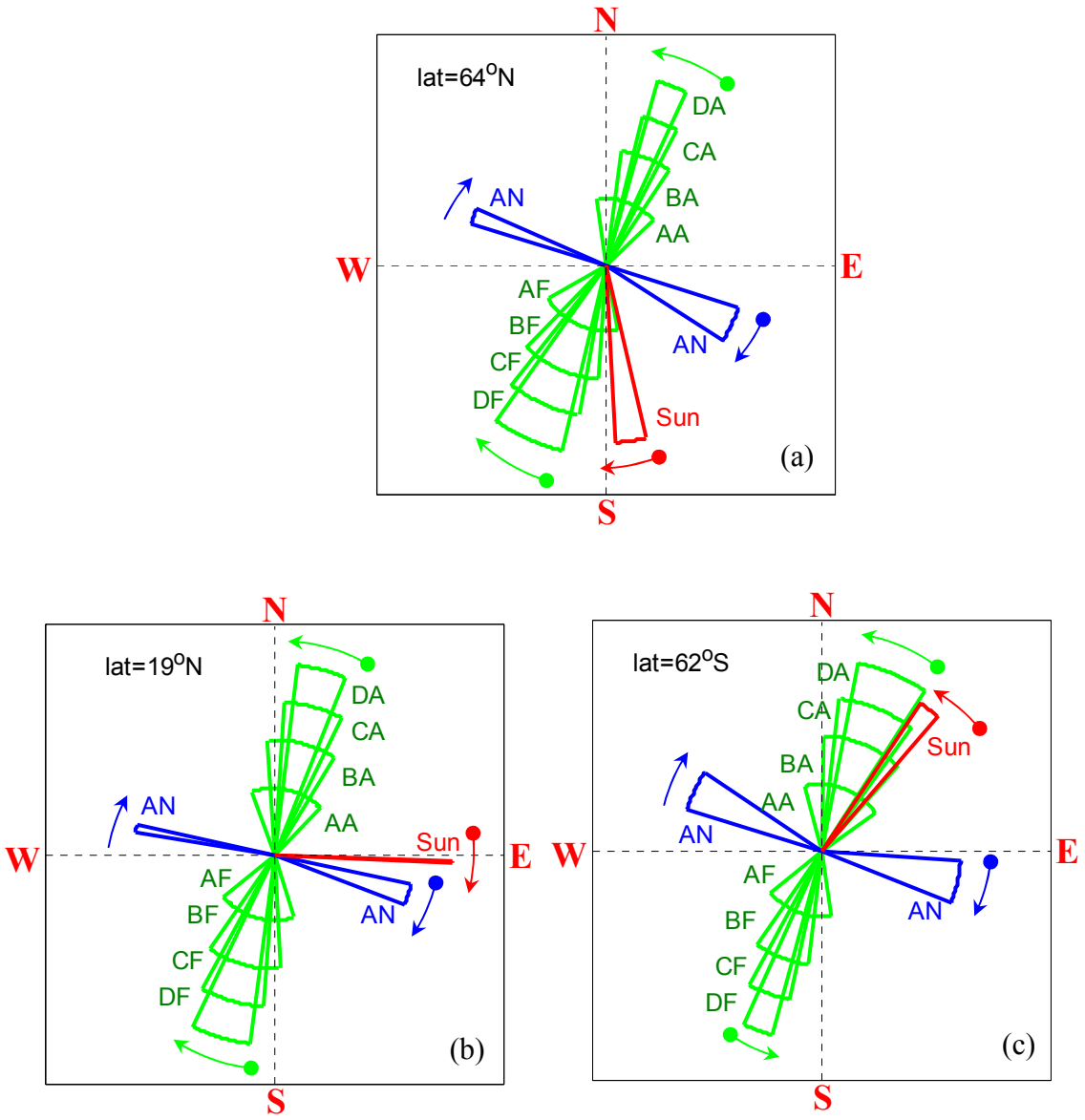

Figure 5.3. *Typical azimuth angle range of the Sun and MISR cameras for observations taken across MISR orbital swath over three latitudes, (a) latitude=64°N, (b) latitude=19°N, and (c) latitude=62°S. The azimuth angle range is depicted by the length of circumference, for example, the azimuth angle for the DA camera in latitude=62°S ranges from 10° to 34° as measured from the north. For the oblique cameras, the radial length reflects the magnitude of the VZA. Examples are taken from MISR orbit 13940, collected on August 01, 2002.*

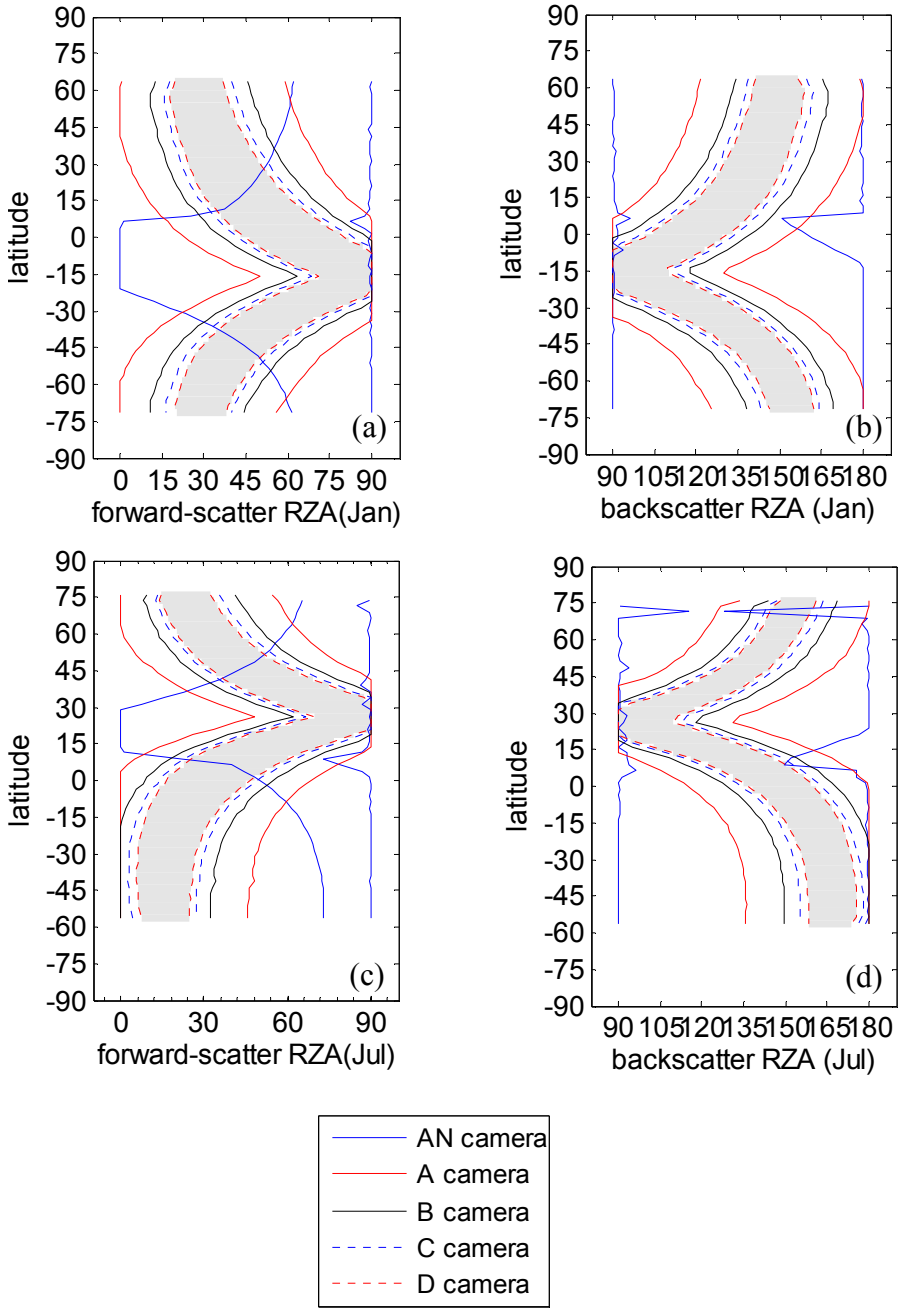

Figure 5.4. *Maximum and minimum relative azimuth angles (RAZ) for MISR cameras as a function of latitude. The ranges of RAZ of the D-camera are shaded. Panels are for RAZ (a) in the forward-scatter direction in January, (b) in the backscatter direction in January, (c) in the forward-scatter direction in July, and (d) in the backscatter direction in July.*

Based on the sampling characteristics of MISR, we tested two sampling criteria regarding RAZ. One criterion is to ensure the sampling in all oblique camera-views being within the same RAZ range. It is achieved by including a cloud observation in an oblique camera-view into our analysis if its RAZ value is within the RAZ range of the D-camera in the forward-scatter and back-scatter directions; however, sampling in this way is not even across oblique camera-views. Alternatively, to sample cloudy pixels equally in all oblique camera-views, we retain the cloudy pixel in our analysis if it is observed in all oblique camera-views within the RAZ range of the D-camera in the forward-scatter and backscatter directions; thus, the RAZ sampling range is reduced compared to the first criterion. By comparing the statistical results obtained with the two strategies, only minor changes are noticed (shown in Figures 5.5-5.7). Therefore, we only discuss the statistical results obtained with the second criterion in the remainder of this chapter. The RAZ criterion, however, is not applied for the AN-camera, because the AN-camera observes clouds in a completely different azimuth angle range compared to the oblique cameras (as shown in Figures 5.3 and 5.4). Fortunately, the retrieved τ is not very sensitive to RAZ in the near-nadir directions of the AN camera. In order to maintain consistent cloud properties over the AN-camera and all forward or aftward cameras, we keep only those cloudy pixels in the AN camera if the RAZ criterion is met for all forward or aftward oblique cameras. Thus, we have an equal sample of retrieved τ for the AN-camera and all forward or aftward cameras over a narrow range of RAZ for a given latitude bin for a given month.

Each latitude bin contains *n* samples of retrieved τ for each MISR camera, from which the mean τ are computed and designated τ^{c}_{mean} for each camera *c*. The biases of mean τ in an oblique camera-view relative to nadir are calculated as follows:

$$\delta^{c}_{mean} = \frac{\tau^{c}_{mean} - \tau^{AN}_{mean}}{\tau^{AN}_{mean}} \times 100\%,$$

where τ^{AN}_{mean} is the mean τ of the AN camera in the forward-scatter (backscatter) direction when computing δ^{c}_{mean} for oblique cameras in the forward-scatter (backscatter) direction. Because the distribution of τ in a latitude-and-camera-view-bin is not necessarily a normal distribution (and indeed, it is not), the relative bias in median τ, δ^{c}_{median}, is given as:

$$\delta^{c}_{median} = \frac{\tau^{c}_{median} - \tau^{AN}_{median}}{\tau^{AN}_{median}} \times 100\%.$$

To examine how the dispersion of τ-distribution changes with view-angle, we calculate the median absolute deviation of the distribution,

$$\varepsilon^{c}_{median} = median\left(\left|\tau^{c}_{i} - \tau^{c}_{median}\right|\right),$$

where τ^{c}_{i} is the individual cloudy pixel τ-value for the MISR camera-view *c* in a latitude bin.

5.5 Results

Figures 5.5 and 5.6 show the VZA dependence of $\tau^{c}_{mean}, \tau^{c}_{median}, \delta^{c}_{mean}, \delta^{c}_{median}$, ε^{c}_{median} and n^{c} along with τ^{AN}_{mean} and τ^{AN}_{median}, all as a function of latitude for January and July. SZA and D-camera-RAZ as a function of latitude are also shown for convenience. As

expected, τ-values in the median are smaller than in mean, because the distribution of τ is skewed towards smaller values. Note that both the mean and median of τ from the MISR AN-camera increases from low latitudes to high latitudes. As discussed in Section 5.2.1, we cannot decouple the SZA bias on our 1-D retrieved τ from latitudinal variations in true τ. Figure 5.7 shows the VZA dependence of τ^c_{mean}, τ^c_{median}, δ^c_{mean} and δ^c_{median} for January and July, but derived with applying the equal RAZ range criteria for all oblique camera-views (Section 5.4). As shown, the statistical results shown in Figure 5.7 are nearly identical as in Figures 5.5-5.6.

5.5.1 Viewing Zenith Angle Dependence of Cloud Optical Thickness under High Sun

Figure 5.5 and 5.6 show some consistencies with earlier observational studies [*Loeb and Coakley*, *1998; Várnai and Marshak*, *2007*] under high Sun conditions. For example, τ shows low sensitivity to VZA over the equators and mid-latitudes where the Sun is high and clouds are viewed in side-scatter directions. The values of δ^c_{mean} and δ^c_{median} are generally within ±10% between 10N° and 52.5°S (SZA=~25°-40°; mean RAZ ranging from 37°-81° in forward-scatter directions and from 99°-145° in backscatter directions) in January and between 2.5°N and 67.5°N (SZA=~18°-46°; mean RAZ ranging from 28°-80° in forward-scatter directions and from 100°-150° in backscatter directions) in July, for VZAs up to 60° (i.e., not including the D-cameras). The low sensitivity to VZA is also shown in the nearly uniform ε^c_{median}-value with VZA. The impact of VZA on the retrieved τ under high Sun becomes more pronounced when clouds

are viewed in the rather oblique viewing directions of the D-cameras. In January, τ is positively biased relative to nadir for SZA=25°-40° by as much as 13% in the forward-scatter direction and 19% in the backscatter direction; in July, τ is positively biased relative to nadir for SZA=18°-46° by 16% in both the forward-scatter and backscatter directions.

To explain this behavior, consider 3-D radiative transfer effects, i.e., shadowing, illumination, channeling and photon-leakage effects as defined by *Várnai and Marshak* [2003]. Studies [*Zuidema and Evans,* 1998*; Várnai and Marshak,* 2003] have suggested that the two roughening effects (shadowing and illumination) are stronger for lower Sun and the two smoothing effects (channeling and photon-leakage) modify the cloud radiance field effectively at all SZAs. Thus, under high Sun, the cloud field is likely smoothed more by the two smoothing effects and less affected by the two weak roughening effects. That is, the cloud is more plane-parallel-like so that the 1-D retrieved τ should depend less on VZA. In addition, viewing from a near-side-scattering direction further leads the 1-D retrieved τ to depend less on VZA, because both shadowed and illuminated cloud-sides lie within the IFOV and their effects cancel each other to some extent. At the very oblique views of the D-cameras, a large fraction of the top of cloud-sides (which are optically closer to the cloud-tops) and less cloudy-gaps (which are optically thinner than the cloud-tops) are seen within the IFOV. The clouds, therefore, appear thicker. This also leads to smoother looking clouds, thus reducing the negative bias in τ due to the non-linear relationship between τ and radiance applied to heterogeneous clouds. Further discussion on these points is given in Section 5.5.3.

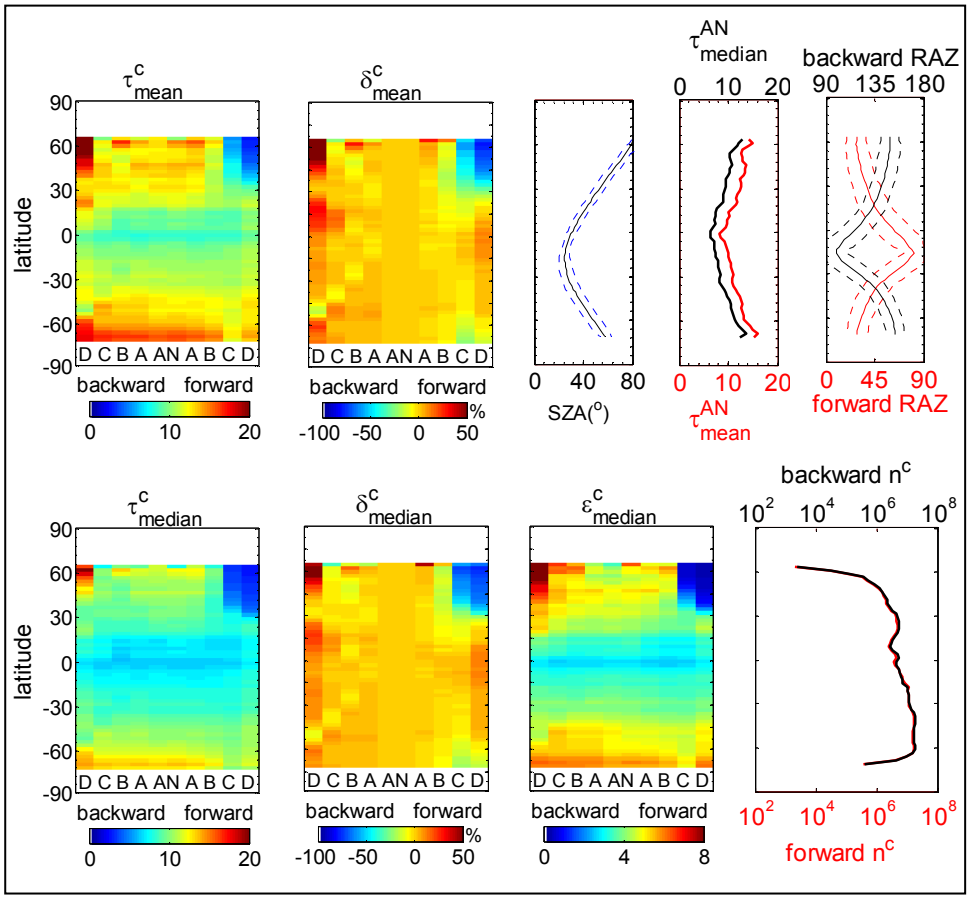

Figure 5.5. *Upper panel from left to right: (1) view-angle dependence of mean cloud optical thickness (τ^{c}_{mean}), (2) view-angle dependence of cloud optical thickness relative bias (δ^{c}_{mean}), (3) mean solar zenith angle (SZA, enveloped by the maximum and minimum), (4) mean and median cloud optical thickness for the MISR AN-camera, denoted as τ^{AN}_{mean} and τ^{AN}_{median}, and (5) mean relative azimuth angle (RAZ) for the MISR D-cameras (enveloped by the maximum and minimum). Bottom panel from left to right: (1) view-angle dependence of median cloud optical thickness τ^{c}_{median}, (2) view-angle dependence of cloud optical thickness relative bias (δ^{c}_{median}), (3) view-angle dependence of cloud optical thickness median absolute deviation (ε^{c}_{median}), and (4) the number of samples (n^{c}) for the forward-scatter directions and backscatter directions. All plots are for January and have latitude as their vertical axis. Plots having view-angle dependence on the horizontal axis are labeled using MISR camera design notation.*

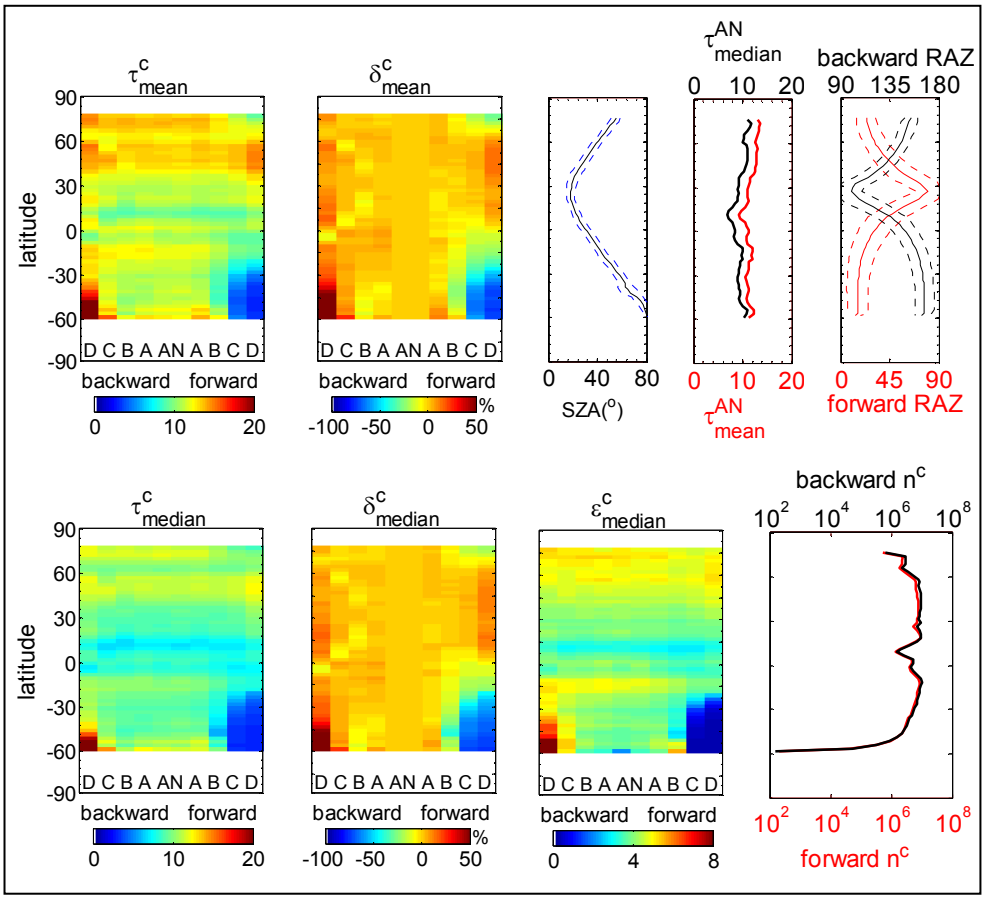

Figure 5.6. *Same as Figure5. 5, but for July.*

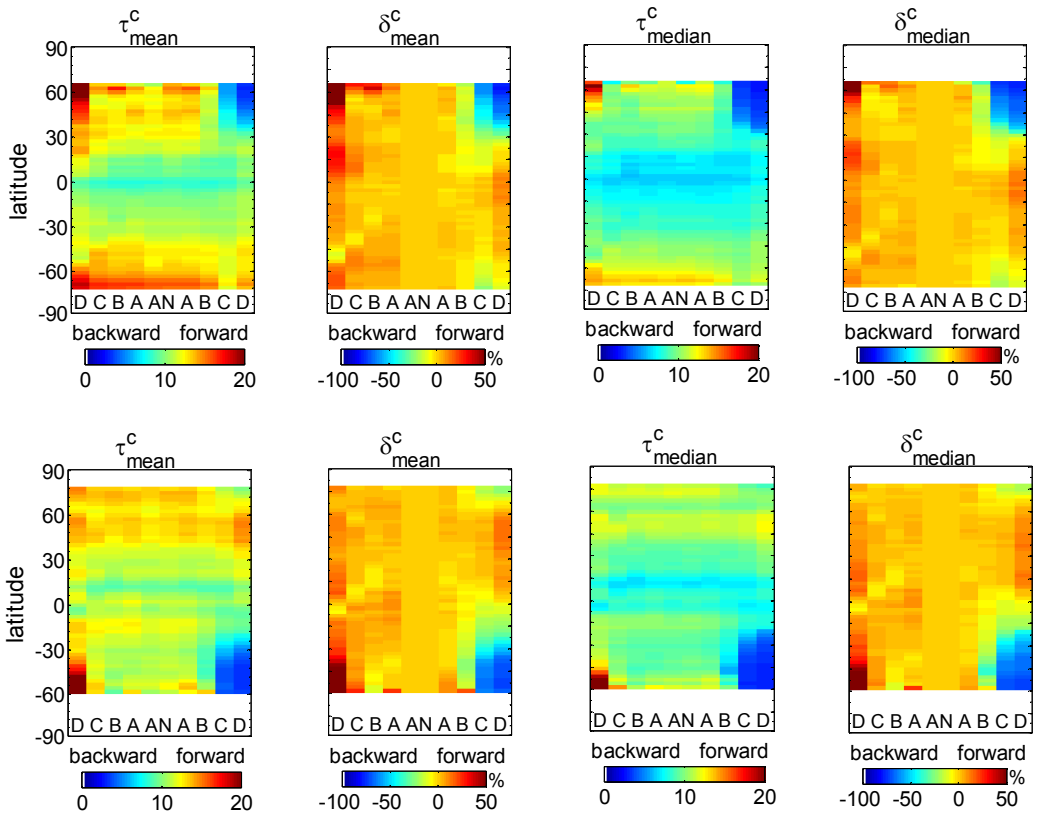

Figure 5.7. *Upper panel from left to right: (1) view-angle dependence of mean cloud optical thickness (τ^{c}_{mean}), (2) view-angle dependence of cloud optical thickness relative bias (δ^{c}_{mean}), (3) view-angle dependence of median cloud optical thickness τ^{c}_{median}, (4) view-angle dependence of cloud optical thickness relative bias (δ^{c}_{median}) for January. Bottom panel from left to right: Same as Upper panel but for July.*

5.5.2 Viewing Zenith Angle Dependence of Cloud Optical Thickness under Oblique Sun

Some observations [e.g., *Loeb and Coakley,* 1998] and model simulations [*e.g., Loeb et al.,* 1998*; Kato and Marshak,* 2009] have shown that under oblique Sun, τ decreases (increases) in the forward-scatter (backscatter) directions and the forward-scatter-decrease in τ is more pronounced than the backscatter-increase in τ when clouds are viewed close to the plane of incidence. These τ-VZA relationships do occur in parts of Figures 5.5 and 5.6. In Section 5.5.4, we make quantitative comparison of our results with that derived from the AVHRR observations in *Loeb and Coakley* [1998] with the same SZA and location. If we use a 10% negative bias (relative to nadir) in the mean τ for VZA=60° in the forward-scatter direction as a threshold to identify the regions with these τ-VZA behaviors, they are found north of 20°N (mean SZA ranging from 40° to 80°) and south of 55°S (mean SZA ranging from 45° to 58°) in January, and north of 70°N (mean SZA ranging from 51° to 55°) and south of equator (mean SZA ranging from 29° to 81°) in July. Quantitatively, for example, In July, at latitude=47.5°S-50°S, where SZA=75° (cosine of the SZA, μ_0=0.17-0.34), τ is biased low in the mean (median) by 73% (70%) from nadir to a VZA=70.5° in the forward-scatter directions; τ is substantially biased high in the backscatter directions only for VZA=70.5°, where it is biased high by 83% (62%). At VZA=45.6°, typical VZA of geostationary satellites observing clouds at high latitudes, the forward-scatter-decrease in τ in the mean (median) is as low as 20% (40%), while the backscatter-increase in τ is not pronounced.

There are other interesting features in Figures 5.5 and 5.6. In the winter hemisphere over latitudes greater than 45°, where the Sun is quite oblique (SZA>68° in January and SZA>73° in July), τ slightly increases and then deceases as VZA increases in the forward-scatter direction, with a δ^{c}_{mean}-peak value ranging from 1% to 28% (1% to 11%) in January (July). We will show that such δ^{c}_{mean}-peaks are more evident for optical thinner clouds (Section 5.5.5) and for clouds with heterogeneous cloud-tops (Section 5.5.6).

5.5.3 Understanding Viewing Zenith Angle Dependence of Cloud Optical Thickness under Oblique Sun

Because the τ dependence on VZA is most pronounced under low Sun (Section 5.5.2), in this section, we summarize three major aspects needed for understanding these VZA dependences based on knowledge gained in past studies and explain some of these τ-VZA relationships with a cloud having a simple cloud-top geometry. These three aspects are described as follows:

(1) Among the four 3-D radiative transfer effects (illumination, shadowing, channeling, and photon leakage), the two roughening effects, illumination and shadowing, strengthen the dependence of τ on VZA, whereas the two smoothing effects, channeling and photon leakage, weaken the dependence by smoothing the cloud radiative field [*Várnai and Marshak,* 2003]. Owing to the two roughening effects, cloud-sides can be classified as either illuminated or shadowed.

(2) The fraction of cloud-sides viewed by a satellite is a function of VZA [e.g., *Zhao and Di Girolamo,* 2004];

(3) When the sub-pixel cloud heterogeneity exists, the deviation of the 1-D retrieved τ for an oblique viewing direction compared to nadir is subject to concavity changes with view-angle in the nonlinear relationship between radiance and τ. If 3-D radiative transfer effects are negligible, then clouds can be well represented by the independent column assumption [*Cahalan et al.,* 1994]. As illustrated in Figure 5.8, for a pixel consisting of two equal-size sub-pixel clouds with τ-values of τ_1 and τ_2, the retrieved optical thickness at nadir, $\tau_{retrieval}^{nadir}$, is less than the truth, $\tau_{true} = (\tau_1 + \tau_2)/2$, owing to the concave non-linear relationship between BRF and τ. Following a similar argument, comparing the retrieved τ-value for an oblique viewing direction ($\tau_{retrieval}^{oblique}$) and that for nadir ($\tau_{retrieval}^{nadir}$), we expect $\tau_{retrieval}^{oblique} < \tau_{retrieval}^{nadir}$ if the radiance-τ for the oblique viewing direction is more concave than nadir; the opposite is true if it is less concave or even more convex.

With these three aspects in mind, we use a cloud with a simple geometry, as shown in Figure 5.9a, to help understand the behavior of τ-VZA. First of all, the radiance of what we observe in an instrument's instantaneous field-of-view (IFOV) is always a result of a radiance competition. Under oblique Sun, in the backscatter direction (Figure 5.9b), more brighter cloud-sides (part-A) and less shadowed cloud-sides (part-B) are seen within the IFOV relative to nadir, which enhances the observed radiances. The enhanced radiance, therefore, leads to a larger retrieved τ with increasing VZA (hereafter, we refer to these τ-enhancements as positive radiation effects (PREs)). However, the increase in radiance is weakened with increasing RAZ by some negative radiation effects (NREs) originating from the increased viewing of the shadowed part-C and the decreased viewing of the illuminated part-D. With the observed radiances, following 1-D radiative transfer

theory (radiance-τ 1-D relationship), the increase in τ is weakened because of a more concave radiance-τ relationship in more oblique viewing directions. On the other hand, τ can be effectively increased when a large radiance is observed, whereby a small radiance increase leads to a large increase in τ because of the asymptotic nature of the radiance-τ relationship. As for the dispersion of the τ-distribution, inferring τ from larger radiance in more oblique viewing directions brings us closer to the asymptotic range of radiance-τ relationship, effectively stretching the τ-distribution towards larger τ-values, and thus resulting in a larger ε^{c}_{median}-value.

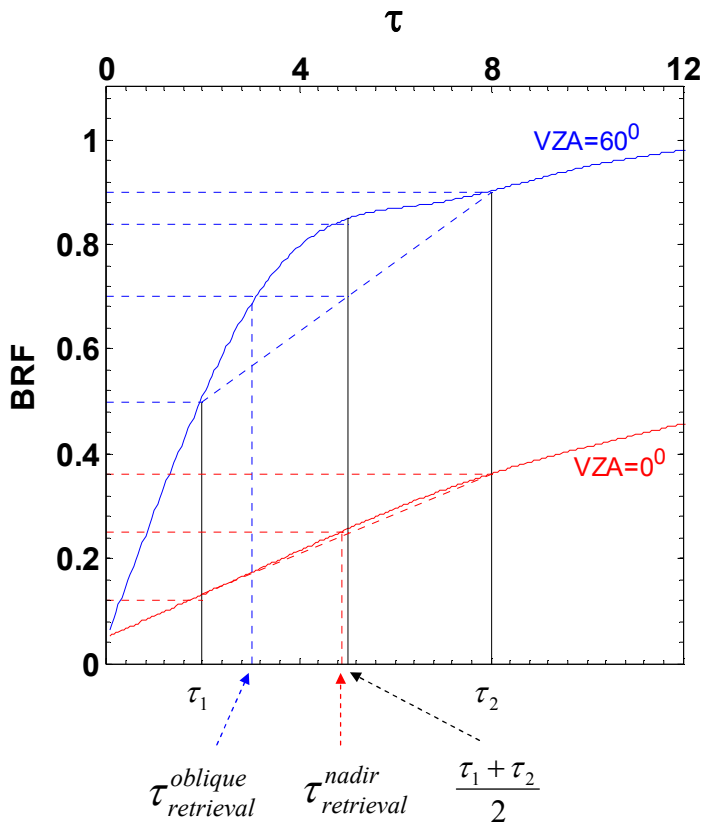

Figure 5.8. *Bidirectional reflectance factor (BRF) of MODIS 866 nm spectral channel as a function of cloud optical thickness for view zenith angle (VZA) = 0° (blue solid line) and 60° (red solid line) with solar zenith angle = 60°, relative azimuth angle between sun and view = 30°, cloud droplet effective radius = 8 μm and surface albedo = 0.05.*

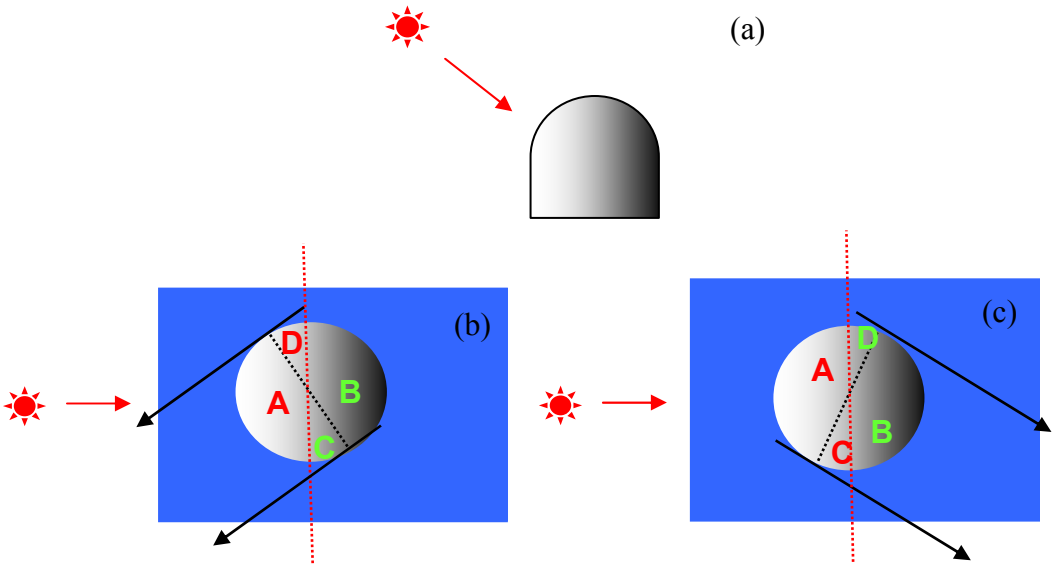

Figure 5.9. *(a) Side view of a cloud with a simple geometry. (b) Top-down view of cloud in the backscatter direction. (c) Top-down view of cloud in the forward-scatter direction.*

Similarly, in more forward-scatter directions (Figure 5.9c), more shadowed part-B and less illuminated part-A are seen within the IFOV, which reduces the observed radiance. The reduction in radiance is compensated by PREs originating from the increased viewing of illuminated part-C and decreased viewing of shadowed part-D with increasing VZA. Again, following 1-D radiative transfer theory, τ is further decreased because of the more concave radiance-τ relationship in more oblique viewing directions. As for the dispersion in the τ-distribution, inferring τ with smaller radiance in oblique forward-scatter directions is pushed away from the asymptotic range of the τ-radiance

relationship. Since 1-D retrieved τ in more oblique viewing directions is more negatively biased relative to nadir for thicker clouds as compared to the thinner clouds (Section 5.5.5), the retrieved τ-values are confined within a narrower τ-range, resulting in a narrower τ-distribution (hence smaller ε^{c}_{median}-value). The above explanation also fits the observations from AVHRR [*Loeb and Coakley,* 1998] and many 3-D model simulations [*e.g., Loeb et al.,* 1998*; Kato and Marshak,* 2009].

When the retrieval is conducted under very oblique Sun, some extra factors need to be taken into account to interpret the observed τ-VZA relationship. When clouds are viewed in the forward-scatter near-nadir direction, the PRE of the increased part-C is strong because cloud-sides can catch sunlights effectively for very oblique Sun. Along with the PRE of the decreased part-D, the total amount of PREs may overpass the NREs (deceased part-A and increased part-B), resulting in a not-necessary-smaller τ-value. When approaching more oblique VZA in the forward-scatter directions, the enhancement in τ can eventually be overpassed by NREs, resulting in a smaller τ. This may explain the δ^{c}_{mean}-peaks in Figures 5.5 and 5.6, Figure 5.12 in Section5.5.5 of τ-VZA for optically thin clouds, and Figure 5.15 in Section 5.5.6 for heterogeneous clouds. Thus, such an "undermined forward-scatter-direction negative bias" can be traced back to the strong radiation enhancement under very low Sun and viewing clouds in a direction not in the plane of incidence.

Furthermore, our explanation seems able to interpret two τ-VZA relationship found in *Várnai and Marshak* [2007] and *Kobayashi* [1993]. With the MODIS observations, *Várnai and Marshak* [2007] found that the MODIS retrieved τ increases with viewing obliquity in the forward-scatter direction with RAZ=60º-70º when

SZA>60º; a 3-D model simulation on the reflected radiance for SZA=80° by *Kobayashi* [1993] showed that a BRF-peak appears at moderately oblique VZAs when RAZ >~30° in the forward-scatter direction and a continuously increase in BRF with viewing obliquity when RAZ approaches 90º. According to this simulation, under very oblique Sun, the retrieved τ should decrease with VZA when RAZ is small, and as RAZ increases, there is a critical RAZ where a peak in τ appears at certain VZA; when RAZ further increases, τ will consistently increase with VZA.

5.5.4 Comparison with the AVHRR Observations

We can compare the derived τ-VZAs from our MISR dataset in July to that from the AVHRR observations [*Loeb and Coakley*, 1998] for the same regions dominated by marine stratus with the same SZA condition. Three relevant cases in Figure 13 of *Loeb and Coakley* [1998] are compared to our MISR observations (Figure 5.10). They are for the observations off the coasts of Peru (5°S-30°S and 70°W-95°W) and Angola (5°S-20°S and 5°W-15°E) for cosine of SZA, μ_0 ,within 0.6-0.7 and 0.7-0.8. Qualitatively, both the MISR and AVHRR observations show the same τ-VZA trends in the forward-scatter directions, but with τ decreasing slower with VZA for MISR compared to AVHRR. In the back-scatter direction, for μ_0 =0.6-0.7, there is little change in τ with VZA for MISR, whereas τ increases with viewing obliquity for the AVHRR.

Many reasons can be attributed to these differences. However, to quantitatively identify how much of each would contribute to the differences is not a trivial task. Some possible reasons are: (1) the difference in RAZ in the two datasets (unfortunately, they were not reported in the AVHRR analysis); (2) the difference in time the observations

were sampled (the MISR analysis is valid for ~10:30 AM in July for observations taken between 2001 and 2008 and the AVHRR analysis is valid for observations from ~2:00 to 5:00 PM in June and May in 1994 and 1995); (3) the difference in the techniques for τ retrieval; (4) the latitudinal variation in true τ buried in the τ-VZA analysis with AVHRR, but not in MISR (Section 5.2.2); and (5) the difference in the consistency in cloudy scene identification across multiple view-angles and pixel size expansion as a function of VZA (Section 5.2.3).

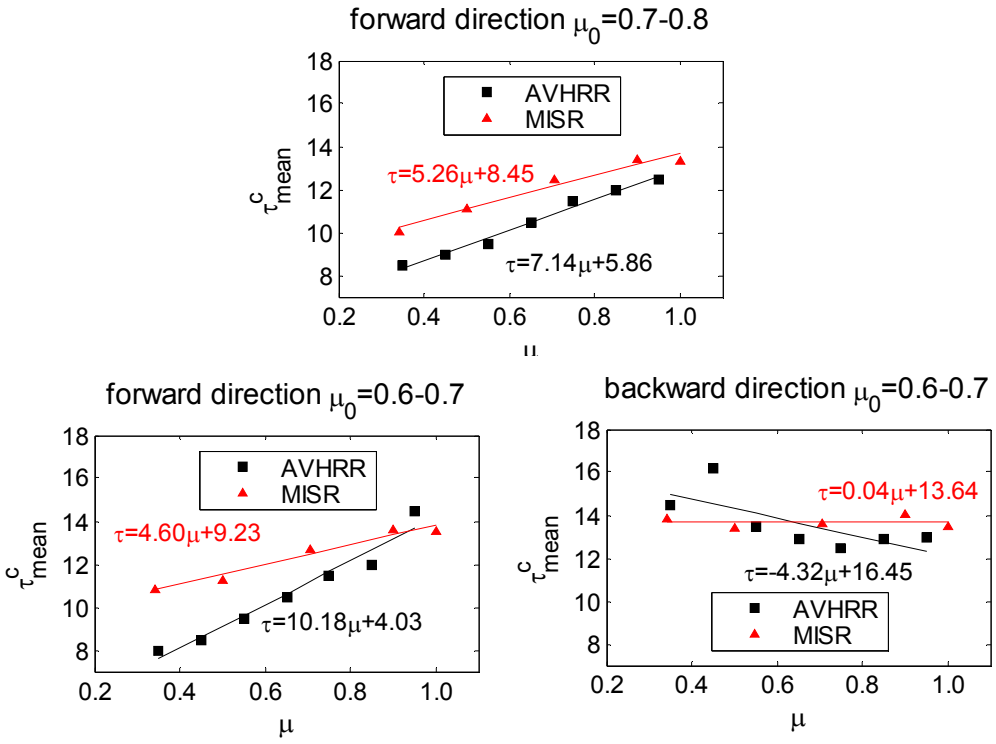

Figure 5.10. *Mean cloud optical thicknesses (τ^{c}_{mean}) as a function of cosine of view zenith angle (μ) derived from the MISR observations are compared to that from AVHRR observations (reproduced from Figure 13 of Loeb and Coakley [1998]) for marine stratus clouds off the coasts of Peru [5°S-30°S and 70°W-95°W] and Angola [5°S-20°S and 15°W-15°E] (a) for the cosine of solar zenith angle μ_0=0.7-0.8 in the forward-scatter direction, (b) for μ_0=0.6-0.7 in the forward-scatter direction, and (c) for μ_0=0.7-0.6 in the backscatter direction.*

In the remainder of this section, we further analyze how the inconsistency in cloudy scene identification may impact the τ-VZA analysis with the AVHRR observations. Since they are intrinsic shortcomings of wide-swath, single-view scanning instruments, not limited to AVHRR, understanding their impacts on derived τ-VZA relationship may help us better interpret and utilize the results derived from those instruments.

We stratify the MISR data for the marine stratus regions, for μ_0=0.6-0.7, into a series of τ^{AN} bins (Figure 5.11) and compare our analysis to Figure 15 in *Loeb and Coakley* [1998], where τ-VZA analysis were stratified into three τ percentile bins of equal width in both forward-scatter and backscatter directions. With a single-view instrument, the percentile-bin approach is the only logical way to stratify data by scene-type when performing a τ-VZA analysis. In contrast, with the multi-angle observations from MISR, it is very convenient to stratify the data based on the nadir observation, because the multi-angle observations for a cloudy element are registered to the nadir observation. Figure 5.11 shows τ-VZA for clouds stratified into a series τ^{AN}–bins. Except the τ^{AN}=0-2 bin (we will discuss this case in Section 5.5.5), τ deceases in the forward-scatter direction with viewing obliquity and is more pronounced for thicker clouds as compared to thinner clouds, which is consistent with the AVHRR analysis. In the backscatter direction, the AVHRR analysis showed that τ slightly increases in the backscatter direction for the thickest-cloud bin and decreases for the moderate- and thinnest-cloud bins with VZA, while our stratification of the MISR data shows that, except the τ^{AN}=0-2 bin, τ is nearly uniform for all VZAs. We attribute the difference between MISR and AVHRR to the inconsistency in cloudy scene identification across multiple view-angles in addition to the

pixel expansion with viewing obliquity (Section 5.2.3). With a wide-swath, single-view scanning instrument like AVHRR, we hypothesize that some truly partially cloudy scenes, as would be classified at nadir, were identified as fully cloudy scenes at oblique VZA, causing the backscatter-direction decrease in τ for the moderate and thinnest cloud bins. In the AVHRR analysis, the spatial coherence method (SCM) identifies spatially smooth scenes in brightness temperature (measured by ~11 μm radiance) with the lowest brightness temperatures identified as fully cloudy scenes. However, the ability of SCM to identifying fully cloudy scenes may depend on view-angle. A partially cloudy scene identified by SCM at nadir may be identified as a fully cloudy scene at larger VZA. This is because at the larger VZA, the colder cloud-sides replace the warmer clear gaps between clouds, leading to the smaller spatial variation in brightness temperature. Including the partially cloudy scene into the analysis skews the retrieved-τ toward smaller values and it should be more pronounced for the thinner clouds than the thicker clouds. In contrast, this problem is minimal in our MISR analysis, as discussed in Section 5.2.3. The decrease in τ for large VZA caused by the inclusion of partially cloud scene and pixel size expansion should also impact the τ-VZA relationship in the forward-scatter direction, but it is buried in the decrease in τ with VZA caused by 3-D radiative transfer effects and other factors, e.g., RAZ, time in which clouds are sampled, retrieval technique and the latitudinal variations in true τ. Also note that this mainly affects the thinner clouds, which may not impact the slopes of τ-VZA when averaged over all clouds.

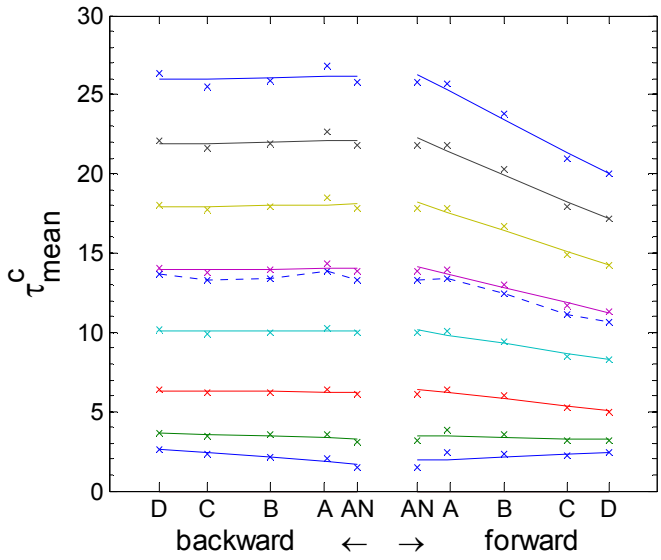

Figure 5.11. *Mean cloud optical thickness (τ^c_{mean}) as a function of MISR camera-view in July for regions off the coasts of Peru [5°S-30°S and 70°W-95°W] and Angola [5°S-20°S and 5°W-15°E] stratified by the MISR nadir cloud optical thickness, τ^{AN}. The τ^{AN}-bins of 0-2, 2-4, 4-8, 8-12, 12-16, 16-20, 20-24 and 24-28 are shown in solid line from the bottom to the top. Dash line is τ^c_{mean} over the optical thickness ranging from 0 to 100. Plots are for cosines of the solar zenith angles ranging from 0.6 to 0.7.*

5.5.5 Impact of Cloud Thickness

To analyze the impact of cloud optical thickness on τ-VZA, we stratified our data into a series of cloud optical thickness bins based on the nadir τ-value, τ^{AN}. Figure 5.12 shows the VZA dependence of δ^c_{mean} as a function of latitude in July for clouds binned into four τ^{AN}-bins: 2-4, 4-8, 8-12 and 24-28. As shown, the impact of cloud optical thickness on τ-VZA tends to be weaker for high Sun compared to low Sun, especially for thicker clouds, which is consistent with *Loeb and Coakley* [1998]. However, under low Sun, the thicker clouds have the more pronounced τ-VZA-biases. Under very low Sun,

δ^c_{mean} peaks in the forward-scatter slightly oblique viewing direction, and tends to be more pronounced for the thinner clouds as compared to the thicker clouds. Taking a closer look at thinner clouds, Figure 5.13 gives τ^c_{mean} and δ^c_{mean} for cloudy pixels with τ^{AN} < 2. This figure shows that τ-VZA behaves differently as compared to Figures 5.5 and 5.6, where clouds are averaged over the τ-value range from 0 to 100. Figure 5.13 shows that for SZA<30°, δ^c_{mean} is small (~25%) for VZA≤45° in both forward-scatter and backscatter directions, and it is even negative in July with δ^c_{mean} reaching -10%. For SZA>30°, δ^c_{mean} is positive in all oblique directions, ranging from 50% to 170%. It is even positive for large SZAs at high latitudes, rather than negative as in Figures 5.5 and 5.6. Also different than Figures 5.5 and 5.6, the peaks in τ for oblique VZA≤45° at high latitudes under very low Sun (SZA>67° in January and SZA>70° in July) are more pronounced, with a δ^c_{mean}-peak value by more than 50% in both January and July.

To explain the behavior of τ with VZA found in Figure 5.13, we need to consider the sunglint effect to better understand these features, in addition to 3-D radiative transfer effects and cloud-side viewing. In the MODIS algorithm for retrieving cloud optical properties, the ocean surface is assumed to be a Lambert reflector, whereby the scattered radiance from the ocean surface is constant in all upwelling directions. In reality, however, direct illumination from the sun results in sunglint that is generally confined to within a 40° cone about the specular direction. For low values of retrieved τ^{AN}, the pixel is either covered by an optical thin layer of cloud, filled with broken cloud, or both. Thus, under high Sun, the satellite can collect surface leaving radiances around the specular direction through thin cloud layers or clear gaps between clouds.

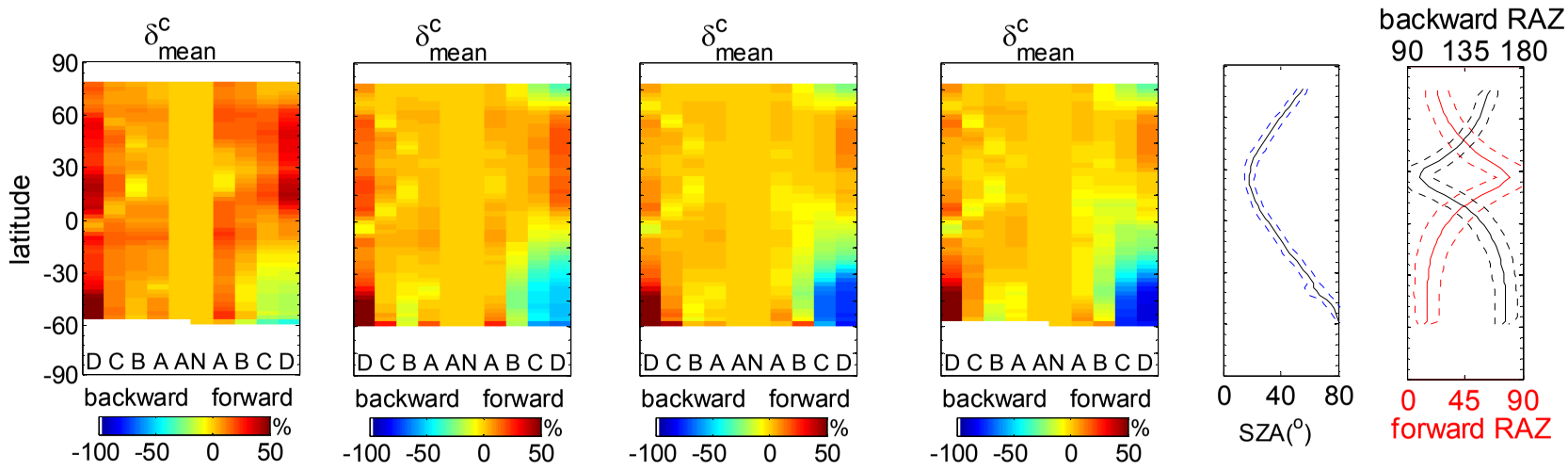

Figure 5.12. *View-angular biases of cloud optical thickness (δ^{c}_{mean}) for four cloud optical thickness bins: 2-4, 4-8, 12-16 and 24-28 are shown from left to right. Clouds are binned based on MISR nadir cloud optical thickness, τ^{AN}, from July. SZA as a function of latitude is shown in the second to right plot and azimuth angle range of D-Camera as a function of latitude is shown in the far right plot.*

Under high Sun, sunglint exists in the near-nadir directions, leading to a larger retrieved τ-value. As the view-angle approaches larger values, sunglint effect weakens and results in less τ enhancement. However, following the argument given in Section 5.5.1, for large VZAs, the increased viewing of cloud-sides within the IFOV largely contributes to the positive τ-biases, since illumination and shadowing effects are weak as a result of the limited vertical extent of thin clouds. This effect may even be stronger for broken clouds, whereby, the much darker ocean surface that are visible in the near nadir directions are not seen in large oblique VZAs within the IFOV.

Under low Sun, given the limited vertical extent of the thin clouds, even the shadowed cloud-sides may potentially be brighter than the darker clear gaps between clouds and the ocean surface. Thus, along with the sunglint effect at low Sun, the increased viewing of cloud-sides with VZA leads to a large τ-values at oblique VZA. However, under very low Sun, shadowing effects become stronger. Following the discussion in Section 5.5.3, the very-oblique-Sun-induced enhancement in radiation dominates the shadowing-effect-induced reduction in radiation at small oblique VZA, which results in a larger τ-value at small oblique VZAs. When observing cloud towards more oblique VZA, the shadowing effect becomes stronger and a decrease in τ is expected.

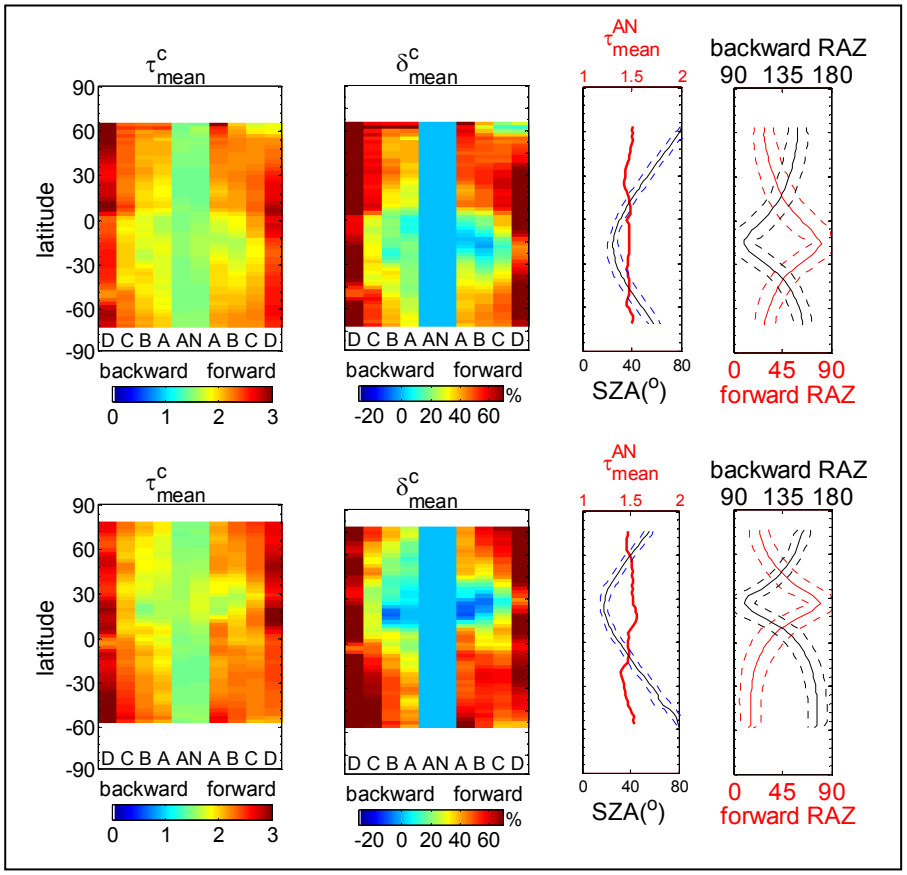

Figure 5.13. *VZA dependence of cloud optical thickness for clouds with MISR nadir cloud optical thickness less than 2 in January (top row) and in July (bottom row). Left to right: (1) mean cloud optical thickness (τ^{c}_{mean}) versus MISR camera-view, (2) cloud optical thickness relative bias δ^{c}_{mean} versus MISR camera-view, (3) solar zenith angle (SZA, enveloped by the maximum and minimum) and mean cloud optical thickness for the MISR AN-camera (τ^{AN}_{mean}), and (4) relative azimuth angle (RAZ) for the MISR D-cameras (RAZ, enveloped by the maximum and minimum), all as a function of latitude.*

5.5.6 Impact of Cloud Heterogeneity

Numerous studies have shown that heterogeneities at the cloud-top play a dominant role on the angular anisotropy of the radiation field [*e.g., Loeb et. al.,* 1998*; Várnai and Davies,* 1999*; Várnai,* 2000]. As marine stratus and marine cumulus

represent two extremes in cloud-top heterogeneities, it is interesting to compare their τ-VZAs. Figure 5.14 shows τ-VZA relationships for two areas within the same latitude bin (25N° to 27.5°N; so that the SZA and RAZ impacts are eliminated) dominated by marine stratus and marine cumulus, respectively. The area dominated by marine stratus over the Pacific lies between 117.5°W to 132.5°W and the area dominated by marine cumulus over the Atlantic lies between 65°W to 97.5°W. As expected, clouds are much more view-angularly consistent in τ over the region dominated by marine stratus as compared to that dominated by marine cumulus.

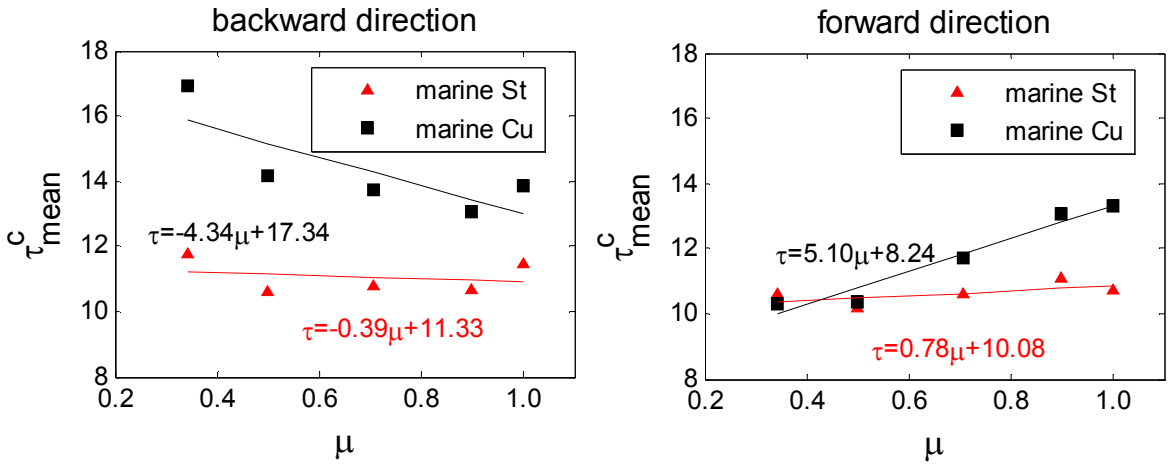

Figure 5.14. *Comparison of mean cloud optical thickness (τ^{c}_{mean}) as a function of cosine of view zenith angle (μ) for a region (bound by 117.5°W to 132.5°W and 25N° to 27.5°N) dominated by marine stratus over the Pacific and a region (bound by 65°W to 97.5°W and 25N° to 27.5°N) dominated by marine cumulus over the Atlantic in the (a) backscatter direction and (b) forward-scatter direction. Data was taken in January with SZA=45°-54°.*

Furthermore, we can examine the impact of cloud heterogeneity on τ-VZA relationships through two heterogeneity parameters that characterize the cloud top local heterogeneity. The first is the brightness temperature difference at the cloud-top, defined as the maximum brightness temperature difference within a 3×3 1.1-km-pixel domain, as suggested by *Várnai and Marshak* [2007]:

$$\Delta T = T_{\max} - T_{\min},$$

where T_{max} and T_{min} are the maximum and the minimum brightness temperatures calculated from MODIS 11 μm radiance at 1 km resolution. The second is the BRF variation at the cloud-top, as in *Liang et al.* [2009]:

$$H_{\sigma} = \frac{\sigma}{\overline{R}},$$

where $\overline{R}$ is the 3×3 1.1-km-pixel domain's mean BRF with a standard deviation of σ, which are calculated from the 275-m resolution 866 nm BRF of the MISR AN-camera. While ΔT measures external cloud-top geometry variations at the pixel scale (except for very thin clouds), H_{σ} is sensitive to both external cloud top geometry variations and cloud internal variations at the sub-pixel scale (275 m). Also, H_{σ} is—and ΔT is not—affected by the solar angle.

To reduce the impact of cloud optical thickness variations on τ-VZA, we confine the examination to clouds within the $\tau^{AN} = 4-8$ bin. Figure 5.15 gives δ^{c}_{mean} as a function of VZA for a series of ΔT and H_{σ} intervals. Two latitude bins in July are shown: the 15°-

17.5°S latitude bin represents a case for moderately oblique Sun with SZA=41°-48° (Figures 5.15a and 5.15c) and the 50°-52.5°S latitude bin represents a case for very oblique Sun with SZA=74°-81° (Figures 5.15b and 5.15d). These figures clearly show that under moderately oblique Sun, the view-angular biases of τ are larger for more heterogeneous clouds. Under very oblique Sun, while there are no apparent relationships between the degree of heterogeneity and τ-biases in the backscatter direction that spans all view angles, the decrease of τ with viewing obliquity in the forward-scatter direction is less pronounced for more heterogeneity clouds. It suggests that those "enhancement" mechanisms in τ for very low Sun and in the forward-scatter direction (Section 5.5.3) take place only when the clouds are bumpy.

Assuming a 6C°/km vertical temperature gradient, for ΔT=0-0.1C° bin (in Figure 5.15a), the cloud top height changing from one pixel to another at 1 km resolution varies from 0 to 17 m. Although it seems rather small, τ-view-angular-biases are still evident in the forward-scatter direction and δ^{c}_{mean} can be as low as -14% (-72%) at VZA=70° for SZA=41°-48° (74°-81°). It suggests that (1) cloud internal variations in the vertical direction may be at play and (2) variations in brightness temperatures measured at the "coarser" 1 km resolution is unable to resolve large variations in cloud top height geometry at the smaller scale. Indeed, studies [*e.g., Loeb et al.,* 1998*; Zuidema and Evans,* 1998*; Iwabuchi and Hayasaka,* 2002*; Kato et al.,* 2006] have suggested that 3-D radiative transfer effects is important when cloud-top height variation is on a order of ~20 to 40 m measured at a horizontal resolution ~50 m.

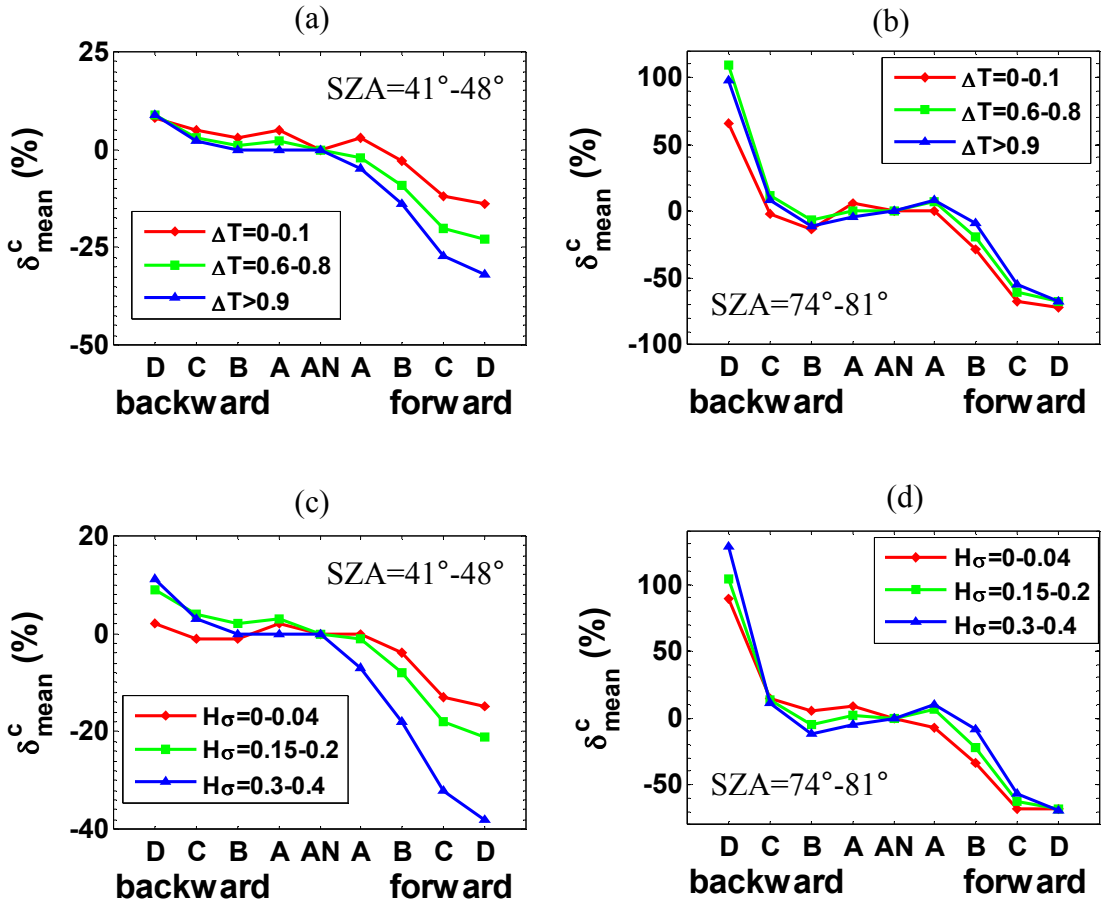

Figure 5.15. *View-angular mean cloud optical thickness bias (δ^{c}_{mean}) as a function of MISR camera-view for a series of brightness temperature variation (ΔT) bins and BRF variation bins (see the text for the definitions of ΔT and H_{σ}). Plots are for clouds with optical thickness values for the MISR AN-camera ranging from 8 to 12 in July. (a) and (c) are for the 15°-17.5°S latitude bin with SZA=41°-48°. (b) and (d) are for the 50°-52.5°S latitude bin with SZA=74°-81°.*

5.6 Summary and Discussion

This study has examined the viewing zenith angle (VZA) dependence of satellite remotely sensed cloud optical thickness (τ) retrieved with the plane-parallel assumption under various solar zenith angles (SZAs) and relative azimuth angles (RAZs). We fused the multiple-angle observations from MISR with the observations from MODIS at cloud-tops for the months of January and July between 2001 and 2008 for oceanic water clouds only. With the unique near-simultaneous multi-angle observations from MISR, we are able to overcome many shortcomings found in previous observational studies on τ-VZA relationships derived from wide-swath, single-view scanning instruments. Unlike previous studies, we are able to exclude cloud seasonal and latitudinal invariant assumptions, eliminate inconsistency in cloudy scene identification across multiple view-angles and minimize the impact of the pixel expansion with viewing obliquity on retrievals.

Our analysis qualitatively confirmed many τ-VZA relationships found in two major observational studies (*Loeb and Coakley* [1998] with the AVHRR observations and *Várnai and Marshak* [2007] with the MODIS observations). For example, in January, our results showed that, under high Sun (SZA< 40° in January), the 1-D retrieved τ is not very sensitive to VZA changes up to VZA=60°. Under low Sun (SZA>45°), the 1-D retrieved τ decreases faster in the forward-scatter direction and increases slower or shows less sensitive to VZA in the backscatter directions when VZA<60°. However, quantitative comparisons are harder to interpret, given the great complexities that plane-parallel retrieved τ depends on, and the different sampling characteristics of the various

dataset. Our results showed that, under oblique Sun, for example, in July at latitude=47.5°S-50°S (SZA=75°), τ is biased low relative to nadir in the mean (median) by 73% (70%) at a VZA=70.5° in the forward-scatter directions; and τ is substantially biased high in the backscatter directions only for VZA=70.5°, with a bias as high as 83% (62%). At VZA=45.6°, the typical VZA of geostationary satellites observing clouds at high latitudes, although the backscatter-direction increase in τ is not pronounced, the forward-scatter-direction decrease in τ is inescapable, with a bias in mean (median) as low as -20% (-40%).

Examining our data out to a larger SZA (SZA>68° in January and SZA>73° in July) and up to VZA=70.5°, and stratifying the analysis by nadir-τ and cloud spatial heterogeneity, revealed additional complexities not observed before. Under high Sun (SZA<40° in both January and July), τ is biased higher than nadir in both forward-scatter and backscatter directions when VZA=70°. Under very low Sun (SZA >68° in January and SZA >73° in July), in the forward-scatter direction, optically thinner clouds and heterogeneous clouds are less negatively biased or even positively biased at small VZAs. This is in contrast to the optically thicker clouds and less heterogeneous clouds, resulting in a slight peak in τ at VZA=26º when averaged over all clouds. While τ increases with VZA by as much as 40% for VZA=60º in both forward-scatter and backscatter directions across the wide-swath of MODIS [*Várnai and Marshak*, 2007], our observed τ-VZA demonstrates that τ-VZA are strongly dependent on relative azimuth angle (RAZ), which when taken into account, explains the differences in τ-VZA amongst various studies.

Stratifying the data by nadir-τ also revealed additional 3-D and non-3-D radiative transfer effects that determine the behavior of τ-VZA relationships. We showcased two

examples. The first one examined τ-VZA relationship for clouds with nadir-τ < 2. The unusual τ behaviors are likely attributed to the combined effects of sunglint radiation enhancement in the near nadir directions and increased viewing of cloud-sides at more oblique VZAs. The second one compared our observed τ-VZAs to that obtained from the AVHRR observations of *Loeb and Coakley* [1998] for regions dominated by marine stratus. Differences in τ-VZA are found for optically moderate to thinner clouds, which is likely attributed to the inconsistency in cloudy scene identification and pixel size expansion with viewing obliquity in the AVHRR analysis. Note that the two shortcomings are not limited to AVHRR, but rather ubiquitous for all wide-swath, single-view scanning instruments.

To understand the complexity in which plane-parallel retrieved τ depends on sun-view geometry requires careful consideration of (1) the various 3-D radiative transfer pathways, including illumination, shadowing, channeling and photon-leakage [*Várnai and Marshak,* 2003], (2) the increased viewing of more cloud-sides with viewing obliquity, (3) RAZ between sun and view, (4) the change in concavity of the radiance-τ non-linear relationship with view-angle, and (5) other 3-D and non-3-D radiative transfer effects, for example, sunglint, inconsistency in cloudy scene identification and pixel size expansion. We considered all of these factors when attributing explanations to the various τ-VZA relationships observed in Section 5.5. However, these are only hypotheses. We recommend 3-D radiative transfer model simulations on realistically representative cloud fields with an adequately characterized cloud-top geometry to further test these hypotheses.

As shown in this section, τ-biases associated with sun-view geometry for real clouds can be very large. Unfortunately, no efforts have been made to correct these biases in any of the major operational retrievals and their subsequent climatologies, thus limiting the scientific usefulness of these datasets. Although our analysis with MISR multi-angle observations eliminates some limitations found in wide-swath, single-view scanning instruments in examining τ-VZA relationships, correcting the VZA dependences in other satellites, such as geostationary satellites, should be restricted to similar sun-view geometries at the same resolution over the same region at roughly the same local time as that of MISR.

Finally, given the great complexities that plane-parallel retrieved τ depends on, we call to the research community to develop new retrieval paradigms for cloud microphysical properties that can properly account for the 3-D radiative transfer found in nature.

CHAPTER 6:SUMMARY AND FUTURE WORK

6.1 Summary

The one-dimensional (1-D) radiative transfer theory, often referred to as the plane-parallel assumption, is commonly used for solving radiative transfer problems in remote sensing applications and in weather and climate models. To remotely retrieve cloud optical properties from passive satellite imagery and for fast calculations of radiative transfer through the cloudy atmosphere, the plane-parallel assumption simplifies the problems from 3-D to 1-D: cloud microphysical properties are homogeneous in the horizontal direction out to infinity. This extreme simplification, however, is contradictory to what we would observe in the real world: clouds are heterogeneous in both horizontal and vertical directions over a wide range of time and space scales [e.g., *Rossow and Cairns,* 1995]. Since the early 70's, the problematic application of the plane-parallel assumption has been investigated from both observations and model simulations and much knowledge has been gained, but we continued to lack the knowledge of the magnitude of the problem on the globe scale. The study presented in this thesis has shed light on this issue.

For the first time, this study (1) has examined the occurrence and to what degree the plane-parallel assumption is valid for any reasonable criterion for real clouds by examining the angular anisotropy in the upwelling radiation observed by the Multiangle Imaging SpectroRadiometer (MISR) and has explored a simple way to identify such valid conditions, and (2) has analyzed the viewing zenith angle

(VZA) dependence of 1-D retrieved cloud optical thickness (τ) from multi-angle observations by MISR. The study was performed based on the fusion of cloud datasets from MISR and the Moderate Resolution Imaging Spectroradiometer (MDOIS), which represents the first attempt to fuse cloud data from these two instruments on the Terra satellite platform since its launch on December 18, 1999. The fused data provided this study a unique and unprecedentedly reliable dataset by overcoming many technical challenges to accomplish the defined objectives. Global observations over eight years in the months of January and July were collected in order to provide ample sampling for statistically robust results. The major conclusions from this thesis are summarized below with original contributions highlighted.

6.1.1 Plane-parallel Nature of Oceanic Water Clouds

For the first time, the degree to which the plane-parallel is valid for oceanic water clouds was quantified globally via cloud radiative view-angle consistency captured by multi-angle observations from MISR. This is on the basis that if the plane-parallel assumption is not valid for a cloud, the plane-parallel simulated bidirectional reflectance factor (BRFs) are substantially different from the observed BRFs at multiple view-angles and an appreciable large variation in the plane-parallel retrieved τ and spherical albedos across multiple view-angles exist. Three metrics, namely, BRF, cloud optical thickness and spherical albedo metrics, were developed to quantify these discrepancies and variations. Such self-consistency examinations are possible owing to the unique capability of the nearly-simultaneous multi-angle observations made by MISR.

The examination was first conducted with a regional cloud dataset over an area in the northeastern Pacific to test the viability of our approach. A suite of algorithms were developed to produce a joint product from MODIS and MISR observations, where observations of a cloud element include τ, effective radii (r_e) of the cloud drop size distribution and cloud thermodynamic phase retrieved by MODIS, multi-angle radiances (converted to BRFs) from MISR, as well as other complementary information. All these information was registered at cloud top. Strict registration criteria were imposed to ensure each registered cloud element are reliably registered, which led to only a subset of data available for analysis. We demonstrated that such a subset is sufficient for deriving a statistically representative result for all cloudy domains in obtaining the occurrences of cloud being plane-parallel for a prescribed confidence level. This was also tested with the global dataset and no apparent bias was found.

For the first time, the probability distribution functions of view-angle consistency relative to plane-parallel in the upwelling radiation were derived from globally representative observations of oceanic water clouds. Results revealed that clouds are angularly consistent in BRF, cloud optical thickness and cloud spherical albedo to within 5% of their plane-parallel value 67.6%, 23.0%, and 72.0% of the time, respectively, for January and 61.0%, 23.7%, and 61.3% of the time, respectively, for July. For metric values < 10%, the angular consistency rates increase to 91.7%, 67.8%, and 92.9% for January and 90.0%, 58.9%, and 84.6% for July in BRF, optical thickness and spherical albedo, respectively.

We also derived the regional distributions over the globe of the frequency in which clouds are view-angularly consistent in these metrics relative to plane-

parallel. Global maps of cloud view-angle consistency occurrences showed large spatial variability and solar zenith angle (SZA) dependence, with stratiform regions being more plane-parallel like than cumuliform regions and stratiform regions being less plane-parallel-like only when SZA is greater than 60º. These maps also clearly showed that a substantial fraction of oceanic water clouds are not valid for the application of the plane parallel assumption by any reasonable criterion, thus lowering our confidence in the application of the plane-parallel assumption in remote sensing for cloud optical properties and climate modeling for radiative transfer calculations.

We related the cloud view-angle consistency in the upwelling radiation to the cloud spatial heterogeneity (H_σ), allowing us to identify, with a prescribed confidence level, which MODIS microphysical retrieval and associated retrieval uncertainty within the MISR swath meet the plane-parallel assumption to within any desired range in view-angle consistency. For example, requiring 96% of the MODIS retrievals to be angularly consistent in τ to within 15% (i.e., optical thickness metric value < 15%) suggests performing retrievals only where $H_\sigma < 0.072$; 22.1% of the cloud observations met this criterion.

The global analysis of the applicability of the plane-parallel assumption is also useful for evaluating existing scientific results that heavily rely on the accurate retrievals of cloud microphysical properties derived with the plane-parallel assumption. For example, a very good correlation was found between our global distribution of view-angle consistency to a global distribution of cloud albedo plane-parallel bias [*Oreopoulos et al.*, 2007], to a global distribution of τ spatial heterogeneity [*Oreopoulos and Cahalan,* 2005] and to a global distribution of cloud albedo susceptibility to droplet number

concentration [*Platnick and Oreopoulos,* 2008*; Oreopoulos and Platnick,* 2008], all based on plane-parallel retrieved τ and r_e derived over grids with a size comparable to that of global climate models. Based on these examples, our results put into question on whether the results from these studies are heavily influenced by the lack of applicability of the plane-parallel assumption over a large fraction of the ocean.

In all current operational retrievals of cloud optical properties by passive remote sensing of reflected shortwave radiation, no retrievals or their uncertainties have accounted for 3-D radiative transfer effects. For example, the retrieval uncertainty of cloud optical property with MODIS only accounted for impacts of radiance calibration, surface spectral albedos, and atmospheric corrections in the plane-parallel retrieval [*Platnick et al.,* 2005]. We still lack a direct estimation of the absolute biases in cloud optical properties and in radiative fluxes for real clouds when 3-D radiative transfer effects are not accounted for. Based on our current global analysis of cloud radiative view-angle consistencies and their relationship to the local cloud spatial heterogeneity (H_σ), it is useful and feasible to provide a H_σ-value for each optical property retrieval at the pixel scale for the standard MODIS cloud optical property retrievals. With this information, the users of those MODIS cloud optical property products can make their own decision of how to treat these observations based on the requirement of their studies.

6.1.2 Viewing Zenith Angle Dependence of Oceanic Water Cloud Optical Thickness

In this thesis, we provided the most comprehensive and reliable estimation of the VZA dependence of 1-D retrieved τ under various SZAs. It was made possible by the

unique multiangle observations of clouds from MISR. With the MISR multiangle observations, we were able to overcome many shortcomings in previous observational studies that used wide-swath, single-view scanning instruments. Unlike previous studies, we were able to exclude the cloud latitudinal invariant assumption, eliminate inconsistency in cloudy scene identification across multiple view-angles and minimize the impact of pixel expansion with viewing obliquity on retrievals. The presented behaviors of τ as a function of VZA corroborated many observed results found in previous studies, while revealing additional complexities by examining our data at large SZAs and VZAs and by stratifying the data in cloud optical thickness and spatial heterogeneity. The main findings are summarized as follows:

(1) **Our analysis confirmed many VZA dependence of τ found in two major observational studies (*Loeb and Coakley* [1998] with AVHRR and *Várnai and Marshak* [2007] with MODIS) and characterized the τ dependence on view-angle regionally.** For example, in January, our results showed that, under high Sun (SZA< 40° in January), the 1-D retrieved τ is not very sensitive to VZA changes up to VZA=60°. Under low Sun (SZA>45°), the 1-D retrieved τ decreases faster in the forward-scatter direction and increases slower or shows less sensitive to VZA in the backscatter directions when VZA<60°. However, quantitative comparisons are harder to interpret, given many variables that the bias in plane-parallel retrieved τ depends on, and the different sampling characteristics of the various dataset. Our results showed that, under oblique Sun, for example, in July at latitude=47.5°S-50°S (SZA=75°), τ is biased low relative to nadir in the mean (median) by 73% (70%) at a VZA=70.5° in the forward-scatter directions; and τ is substantially biased high in the backscatter directions only for

VZA=70.5°, with a bias as high as 83% (62%). At VZA=45.6°, the typical VZA of geostationary satellites observing clouds at high latitudes, although the backscatter-direction increase in τ is not pronounced, the forward-scatter-direction decrease in τ is inescapable, with a bias in mean (median) as low as -20% (-40%).

(2**) Examining our data for the larger SZAs and VZAs and stratifying the data by nadir-τ and cloud spatial heterogeneity revealed additional complexities not observed before.** Under high Sun (SZA<40° in both January and July), τ is biased higher than nadir in both forward-scatter and backscatter directions when VZA=70.5°. Under very low Sun (SZA >68° in January and SZA >73° in July), in the forward-scatter direction, optically thinner clouds and heterogeneous clouds are less negatively biased or even positively biased at small VZAs, which is in contrast to the optically thicker clouds and less heterogeneous clouds, resulting in a slight peak in τ at VZA=26º when averaged over all clouds. While τ increases with VZA by as much as 40% for VZA=60º in both forward-scatter and backscatter directions across the wide-swath of MODIS [*Várnai and Marshak*, 2007], our observed τ-VZA demonstrates that τ-VZA are dependent on relative azimuth angle (RAZ), which when taken into account, explains the differences in τ-VZA amongst various studies.

(3) **In addition, stratifying data by nadir τ revealed additional 3-D and non 3-D radiative transfer effects that determine the behavior of τ with sun-view geometry.** Globally, for SZA<30°, while τ for optically thinner clouds (nadir τ < 2) is nearly unchanged or negatively biased slightly in moderate oblique view-angles (VZA=26°-45°) in both forward-scatter and backscatter directions, they are positively biased for all oblique VZAs when SZA>30°. This is different from how optically thick

clouds behave with VZA. The combined effects of sunglint radiation enhancement in the near nadir directions and increased viewing of cloud-sides at more oblique view-angles explains these behaviors. Regionally, in comparison to the AVHRR observations over regions dominated by marine stratus off the coasts of Peru and Angola [*Loeb and Coakley,* 1998], stratifying our data by nadir-τ identified weaknesses of using wide-swath, single-view scanning instruments for the analysis of τ-VZA. Our results showed that τ changes little or increases with VZA in backscatter directions, whereas AVHRR-observed τ decreases for optically thin and moderately thin clouds. The differences can be attributed to the inconsistency in cloudy scene identification and pixel ground instantaneous field-of-view (GIFOV) expansion in AVHRR, both as a function of view-angle.

(4) **A comprehensive physical picture was given of how sun-view geometry, in both zenith and azimuth angles, affects τ retrievals with the plane-parallel assumption for clouds with substantially heterogeneous cloud-tops.** To fully understand the complex dependence of 1-D retrieved τ on sun-view geometry, we need to at least take into account the following aspects: (1) Among the four 3-D radiative transfer effects (illumination, shadowing, channeling and photon leakage), illumination effect leads to larger 1-D retrieved τ-values and shadowing effect leads to small 1-D retrieved τ-values, strengthening the dependence of τ on VZA; whereas the two smoothing effects, channeling and photon leakage, weaken the dependence by smoothing the cloud radiative field [*Várnai and Marshak,* 2003]. (2) The viewing of more cloud-sides within the instantaneous filed-of-view of the satellite instruments increases with viewing obliquity. Viewing more illuminated cloud-sides leads to a larger retrieved τ-value and viewing

more shadowed cloud-sides leads to a smaller retrieved τ-value; that is, their impacts on the retrieved τ-value compete against each other. (3) The fraction of the IFOV viewing shadowed and illuminated cloud-sides are also a function of RAZ, with viewing more (less) shadowed (illuminated) cloud-sides in more forward-scatter directions; the opposite is true in more backscatter directions, (4) The concavity of the non-linear relationship between radiance and τ is a function of sun-viewing geometry. Given a SZA and RAZ, a radiance changing with τ more concavely as VZA increases leads to a smaller retrieved τ-value; the opposite is true if radiance changes with τ more convexly as VZA increases. (5) Other non-3-D radiative transfer effects also affect the retrieved τ-value. For example, sunglint has an enhancement effect on the retrieved τ-value, whereas including more partially cloud-covered scenes at larger VZAs and retrieving at a coarser resolution reduce the retrieved τ-value.

Our results have shown large systematic errors with VZA that are regionally dependent. Such biases exist in all major operational retrievals. Unfortunately, no efforts have been made to correct these biases in major operational retrievals, undermining the scientific usefulness of these datasets. Although our analysis with MISR multi-angle observations eliminated some limitations found in wide-swath, single-view scanning instruments in examining the view-angle dependence of τ, correcting these dependences in other satellites, such as geostationary satellites, should be restricted to similar sun-viewing geometries at the same resolution over the same region at roughly same local time as that of MISR. By doing so, the influence on the climatological records can be assessed properly thereafter.

6.2 Future Work

Given the results presented in this thesis, three major issues are identified and worth addressing in the future, touching on topics from further understanding of the dependence of τ on sun-view geometries, to removing τ biases, and to devising a new *τ*-retrieval paradigm.

6.2.1 Further Understanding of Sun-view Geometry Dependence of Cloud Optical Thickness

Having recognized the importance of adequately characterizing the cloud-top geometry for quantifying 3-D radiative transfer effects in the oblique sun-viewing geometries based on the analysis presented in Chapter 5, enhancing our understanding of retrieval behavior with sun-view geometry will require a series of improved 3-D radiative transfer model simulations. Such model simulations need to handle detailed cloud-top geometry at a fine scale and in full 3-D space, while carefully accounting for the IFOV of a simulated instrument. The most sophisticated description of cloud top heterogeneity is usually through statistics of the cloudy scene, such as standard deviation of cloud-top height [*e.g., Loeb et al,* 1998*; Kato et al,* 2006]. Additional descriptions of cloud top geometry are needed to quantitatively resolve the radiation competition as a function of view-angle between the enhancement by illuminated cloud-sides and the reduction by shadowed cloud-sides, although some attempts have been made [*Várnai and Marshak,* 2003]. Such simulations are necessary to verify our understandings of the complex τ-VZA relationships extracted from the observations.

Not only do 3-D radiative transfer effects play a role in 1-D τ retrieval, but also, non-3-D radiative transfer effects. For example, retrieval scale is an important factor to consider. Studies have shown that the retrieved τ is considerably biased negatively when the retrievals are conducted at a coarser resolution [*e.g., Marshak,* 1995*; Várnai and Marshak,* 2001*; Zinner and Mayer,* 2006]. Although their results were drawn from retrievals in the near-nadir directions, the conclusion should stay true in other view-angles. However, the questions is: "how much?" The answer to this question is necessary to help evaluate and interpret the retrieval biases as a function of view-angle with any wide-swath single-view instrument, where the retrievals are performed at nadir under a smaller scale and the retrievals in oblique view-angles at a much larger scale.

6.2.2 Estimating Cloud Optical Property Retrieval Biases

The view-angle consistency in the radiation field relative to plane-parallel shown in this thesis represents the first step toward understanding the valid use of the plane-parallel assumption from regional to global scales. We showed that a large fraction of oceanic water clouds are not valid for the application of the plane-parallel assumption and that the spatial and temporal dependence of the invalid use of the plane-parallel assumption is not random. However, it did not tell us directly the absolute biases in 1-D retrieved cloud optical properties. It would be extremely useful to relate the retrieval biases to the radiative view-angle consistency metrics and the spatial heterogeneity, so that the applicability of the plane-parallel assumption over the globe can be evaluated on the basis of more tangible terms (i.e., the absolute biases in cloud optical properties, such as τ, r_e, liquid water path and cloud albedo). The global biases can be assessed thereafter.

One possible solution to this problem is through model simulations, by which the relationship between retrieval bias and the metrics can be constructed. However, a globally representative cloud dataset with known optical properties is still unknown. Even though cloud properties can be generated with cloud resolving models [*e.g., Stevens et al.,* 1999], stochastic cloud models [e.g., *Barker and Davies* 1992], or constructed from observations, such as cloud radar [*Zuidema and Evans,* 1998] and satellite [*Seiz and Davies,* 2006*; Zinner et al.,* 2006], it is a daunting task to tackle, simply because of the enormous computational demands.

Alternatively, we can address this issue observationally if a coincident third party measurement of cloud optical properties exists globally and such a measurement is not a function of 3-D and non-3-D radiative transfer effects. Such a solution is possible with cloud observations from the "A-train" satellite constellation. It is a group of six satellites flying in formation within minutes of each other led by Aqua and followed by five other satellites [*Stephens et al.,* 2002]. Among the six satellites, the cloud structure and composition derived from active remote sensing at 94 GHz by CloudSat [*Stephens et al.,* 2002] can potentially be used to evaluate τ biases of Aqua MODIS that takes measurements ~ 1 minute earlier. Two approaches of how to use the new cloud information, directly and indirectly, are discussed below.

The direct approach, as implied, is to compare cloud properties measured from CloudSat directly to that from Aqua MODIS and the relationship between the cloud spatial heterogeneity parameter, H_σ, derived from Aqua MODIS and the retrieval biases can be established. One concern, however, is that it heavily relies on the absolute accuracy of the CloudSat retrieval. Its validation, unfortunately, remains not available.

In contrast, an indirect approach does not require the absolutely retrieval accuracy from CloudSat. Rather, as proposed here, it only requires that the CloudSat-inferred τ has a monotonic relationship with the true value. Based on the assumption that CloudSat-inferred τ is not a function of 3-D and non-3-D radiative transfer effects as we have discussed in this thesis, for clouds within a narrow CloudSat-τ range, both the homogeneous clouds (with a small H_σ-value) and the heterogeneous clouds (with a large H_σ-value) have the same mean CloudSat-τ value that corresponds to a same true τ-value. As the true τ-value can be well approximated by the coincident MODIS τ retrievals performed on the homogenous clouds defined by H_σ in this narrow CloudSat-τ bin, the τ biases for the heterogeneous clouds can therefore be estimated by the departures from that "truth". Applying this approach over the globe yields grid means of τ- and r_e- biases, with the following pattern expected: a positive (negative) bias in τ-value tends to associate with a negative (positive) bias in r_e-value. This is because the larger the τ-value, the larger the radiance in the shortwave, non-absorbing channel used in the retrieval (in the MODIS case over ocean, it is 866 nm spectral channel [*King et al.,* 1997]), whereas for the larger r_e-value, the smaller radiance in the shortwave absorbing channel used in the retrieval (in the MODIS case over ocean, it is 2.13 μm spectral channel [*King et al.,* 1997]). For example, a pixel largely containing shadowed cloud-sides tends to reflect less 866 nm radiance and less 2.13 μm radiance, leading to a smaller retrieved τ-value and a larger r_e-value.

6.2.3 New Cloud Optical Thickness Retrieval Paradigm

We have shown that τ is a strong function of sun-viewing geometry, especially under large SZAs and VZAs (Chapter 5), and the plane-parallel assumption is not suitable for a large fraction of water clouds over a large fraction of ocean (Chapter 4). In addition, for successfully detecting climate trends, the retrieved accuracy of τ is required to be within 10% [*Ohring et al.*, 2005] and such a goal has yet to be met with the current retrieval techniques. The accurate retrieval of cloud optical thickness can only be made possible when 3-D radiative transfer effects found in nature are fully realized. Given that none of the current operational retrieval algorithm is able to do so, a new retrieval paradigm is urgently needed to ultimately meet the climate research demands.

Some attempts have been made and the techniques used can be loosely classified into two types: neural network techniques [*e.g., Cornet et al.,* 2004*; Evans et al.,* 2008*; Gabriel et al.,* 2009] and 3-D radiative transfer iteration techniques [*e.g., Marchand and Ackerman,* 2004*; Zinner et al.,* 2006]. The attraction of the neural network retrieval technique is the computational speed. One implementation of this technique has emerged by *Evans et al.* [2008], who examined the value of multi-angle radiance measurements for retrieve τ. Two critical improvements, however, can be performed to further evaluate its value for τ retrievals: (1) registering the multi-angle radiances of a cloud at the cloud-top to well represent the cloud angular anisotropy in upwelling radiation, rather than at a constant height somewhere below the cloud-top, and (2) feeding additional multi-angle constraints to the neural network to better capture 3-D radiative transfer in clouds. For example, such additional constraints can be the radiances from neighboring pixels of the target cloudy pixel, since 3-D radiative transfer effects are by no means spatially local.

However, it is impossible to develop a training set for the global application of this technique; it requires a known cloud property field over the globe to begin with. On the other hand, the 3-D-radiative transfer iteration technique retrieves τ by beginning with an estimate of cloud property field, followed by iterating 3-D radiative transfer calculations and adjusting cloud optical properties between iterations; the iteration is terminated once a convergence criterion is met. The observations of clouds from MISR are therefore the natural constraints from multiple view-angles and can be used to devise a powerful radiance criterion based the convergence of the observed and simulated radiances from all available view-angles in each iteration. Clearly, one of the major drawbacks of this technique is the enormous demand on computational resources. With the advancements in modern computational technologies, applying this retrieval technique operationally over the globe may be practical in the future.

REFERENCES

Barker, H. W. (1994), Solar radiative transfer for wind-sheared cumulus cloud fields. *J. Atmos. Sci.,* **51,** 1141–1156.

Barker, H. W. (1996), A parameterization for computing grid-averaged solar fluxes for inhomogeneous marine boundary layer clouds. Part I: Methodology and homogeneous biases, *J. Atmos. Sci.,* **53**, 2289–2302.

Barker, H. W. (2000), Indirect aerosol forcing by homogeneous and inhomogeneous clouds, *J. Clim.,* **13**, 4042 – 4049.

Barker, H.W., et al. (2003), Assessing 1D atmospheric solar radiative transfer models: interpretation and handling of unresolved clouds, *J. Clim*., ***16***, 2676-2699.

Barker, H. W., and J. A. Davies (1992), Solar radiative fluxes for stochastic, scale-invariant broken cloud fields, *J. Atmos. Sci.,* **49,** 1115–1126.

Barnes, W. L., T. S. Pagano, and V. V. Salomonson (1998), Pre-launch characteristics of MODIS on EOS-AM1, *IEEE Trans. Geosci. Remote Sens.,* **36**, 1088– 1100.

Bréon, F. M. (1992), Reflectance of broken cloud fields: Simulation and parameterization, *J. Atmos. Sci.,* **49,** 1221–1232.

Cahalan, R. F., W. Ridgway, W. J. Wiscombe, S. Golmer, and Harshvardan (1994), Independent pixel and Monte Carlo estimates of stratocumulus albedo, *J. Atmos. Sci.,* **51**, 3776– 3790.

Cess, R. D., et al. (1989), Interpretation of cloud-climate feedback as produced by 14 atmospheric general circulation models, *Science*, **245**, 513–516.

Charlson, R. J., S. E. Schwartz, J. M. Hales, R. D. Cess, J. A. Coakley Jr., J. E. Hansen, and D. J. Hofmann (1992), Climate forcing by anthropogenic aerosols, *Science,* **255**, 423– 430.

Cole, J. N. S., H. W. Barker, W. O'Hirok, E. E. Clothiaux, M. F. Khairoutdinov, and D. A. Randall (2005), Atmospheric radiative transfer through global arrays of 2D clouds, *Geophys. Res. Lett.,* **32**, L19817, doi:10.1029/2005GL023329.

Colman, R. (2003), A comparison of climate feedbacks in GCMs, *Climate Dyn*., **20**, 865-873.

Cornet, C., H. Isaka, B. Guillemet, and F. Szczap (2004), Neural network retrieval of cloud parameters of inhomogeneous clouds from multispectral and multiscale radiance data: Feasibility study, *J. Geophys. Res.,* **109**, D12203, doi:10.1029/2003JD004186.*Geosci. Remote Sens.,* **40**, 1532–1540.

Davies, R. (1978), The effect of finite geometry on the three-dimensional transfer of solar irradiance in clouds, *J. Atmos. Sci.,* **35**, 1712-1725, 1978.

Davies, R. (1984), Reflected solar radiances from broken cloud scenes and the interpretation of scanner measurements, *J. Geophys. Res.,* **89,** 1259 –1266.

Di Girolamo, L., T. Várnai, and R. Davies (1998), Apparent breakdown of reciprocity in reflected solar radiances, *J. Geophys. Res.,* **103,** 8795–8803.

Diner, D. J., et al. (1998), Multiangle Imaging SpectroRadiometer (MISR) description and experiment overview, *IEEE Trans. Geosci. Remote Sens.*, **36**, 1072– 1087.

Diner, D. J. et al. (1999), MISR Level 2 Cloud Detection and Classification. MISR Algorithm Theoretical Basis Documents, ATBD-MISR-07. NASA JPL, available at http://eospso.gsfc.nasa.gov/atbd/misrtables.html.

Evans, K.F., A. Marshak, and T. Várnai (2008), The Potential for Improved Boundary Layer Cloud Optical Depth Retrievals from the Multiple Directions of MISR, *J. Atmos. Sci.,* **65**, 3179–3196.

Fu, Q., M.C. Cribb, H.W. Barker, S.K. Krueger, and A. Grossman (2000), Cloud geometry effects on atmospheric solar absorption, *J. Atmos. Sci.***, 57**, 1156–1168.

Gabriel, P., H. W. Barker, D. O'Brien, N. Ferlay, and G. L. Stephens (2009), Statistical approaches to error identification for plane-parallel retrievals of optical and microphysical properties of three-dimensional clouds: Bayesian inference, *J. Geophys. Res.,* **114,** D06207, doi:10.1029/2008JD011005.

Genkova, I., and R. Davies (2003), Spatial heterogeneity of reflected radiance from globally distributed clouds, *Geophys. Res. Lett.*, **30**(21), 2096, doi:10.1029/2003GL018194.

Hahn, C.J., and S.G. Warren(1999), Extended Edited Cloud Reports from Ships and Land Stations over the Globe, 1952-1996. *Numerical Data package NDP-026C,* Carbon Dioxide Information Analysis Center (CDIAC), Department of Energy, Oak Ridge, Tennessee.

Harshvardhan, and D.A. Randall (1985), Comments on "The parameterization of radiation for numerical weather prediction and climate models", *Mon. Wea. Rev.*, **113**, 1832–1833.

Horváth, A., and R. Davies (2004), Anisotropy of water reflectance: A comparison of measurements and 1D theory, *Geophys. Res. Lett*., **31** (1), doi:10.1029/2003GL018386.

Jovanovic, V. M., S. Lewicki, M. Smyth, J. Zong, and Robert Korechoff (1999), Level 1 Georectification and registration algorithm theoretical basis, *JPL Tech. Doc,* D-11532, Rev. D., Jet Propulsion Laboratory, California Institute of Technology, Pasadena, CA.

Kato, S., L. M. Hinkelman, and A. Cheng (2006), Estimate of satellite-derived cloud optical thickness and effective radius errors and their effect on computed domain-averaged irradiances, *J. Geophys. Res*., **111,** D17201, doi:10.1029/2005JD006668.

Kato, S., and A. Marshak (2009), Solar zenith and viewing geometry-dependent errors in satellite retrieved cloud optical thickness: Marine stratocumulus case, *J. Geophys. Res*., **114,** D01202, oi:10.1029/2008JD010579.

King, M. D., S.-C. Tsay, S. E. Platnick, M. Wang, and K. N. Liou (1997), Cloud retrieval algorithms for MODIS: Optical thickness, effective particle radius, and thermodynamic phase, *MODIS Algorithm Theoretical Basis Document,* No. ATBD-MOD-05, available at http://modis.gsfc.nasa.gov/data/atbd/.

Kobayashi, T. (1993), Effects due to cloud geometry on biases in the albedo derived from radiance measurements, *J. Clim.,* **6,** 120– 128.

Liang, L., L. Di Girolamo, and S. Platnick (2009), View-angle consistency in reflectance, optical thickness and spherical albedo of marine water-clouds over the northeastern Pacific through MISR-MODIS fusion, *Geophys. Res. Lett.,* **36,** L09811, doi:10.1029/2008GL037124.

Loeb, N. G., and R. Davies (1996), Observational evidence of plane parallel model biases: The apparent dependence of cloud optical depth on solar zenith angle, *J, Geophys. Res.,* **101,** 1621-1634.

Loeb, N. G., and R. Davies (1997), Angular dependence of observed reflectances: A comparison with plane parallel theory, *J. Geophys. Res.,* **102**, 6865–6881.

Loeb, N. G., and J. A. Coakley Jr. (1998), Inference of marine stratus cloud optical depths from satellite measurements: does 1D theory apply? *J. Clim.,***11,** 215–233.

Loeb, N. G., T. Varnai, and R. Davies (1997), Effect of cloud inhomogeneities on the solar zenith angle dependence of nadir reflectance*, J. Geophys. Res.,* **102**, 9387–9395.

Loeb, N. G., T. Várnai, and D. M. Winker (1998), Influence of subpixel-scale cloud-top structure on reflectances from overcast stratiform cloud layers, *J. Atmos. Sci***., 55**, 2966-2973.

Lyapustin, A., Y. Wang, R. Kahn, J. Xiong, A. Ignatov, R. Wolfe, A. Wu, B. Holben, and C. Bruegge (2007), Analysis of MODIS-MISR calibration differences using surface albedo around AERONET sites and cloud reflectance, *Remote Sens. Environ., **107,** 12-21.*

Minnis, P. (1989), Viewing zenith angle dependence of cloudiness determined from coincident GOES East and GOES West data, *J. Geophys. Res.,* **94**, 2303–2320.

Marchand, R., and T. Ackerman (2004), Evaluation of radiometric measurements from the NASA Multiangle Imaging Spectroradiometer (MISR): Two- and three-dimensional radiative transfer modeling of an inhomogeneous stratocumulus cloud deck, *J. Geophys. Res.,* **109**, D18208, doi:10.1029/2004JD004710.

Marshak, A., A. Davis, W. Wiscombe, and R. Cahalan, 1995a: Radiative smoothing in fractal clouds, *J. Geophys. Res.,* **100,** 26 247–26 261.

Marshak, A., and A. Davis Eds. (2005), *3D Radiative Transfer in Cloudy Atmospheres,* Springer, New York.

Marshak, A., S. Platnick, T. Várnai, G. Wen, and R. F. Cahalan (2006), Impact of three-dimensional radiative effects on satellite retrievals of cloud droplet sizes, *J. Geophys. Res.,* **111**, D09207, doi:10.1029/2005JD006686.

McFarlane, S., R. Marchand, and T. Ackerman (2005), Retrieval of cloud phase and crystal habit from Multiangle Imaging Spectroradiometer (MISR) and Moderate Resolution Imaging Spectroradiometer (MODIS) data*, J. Geophys. Res.,* **110**, D14201, doi:10.1029/2004JD004831.

Muller, J-P., A. Mandanayake, C. Moroney, R. Davies, D. Diner, S. Paradise (2002), MISR Stereoscopic Image Matchers: Techniques and Results, *IEEE Trans. Geosci. Remote Sens.*, **40,** 1547-1559.

Nishihama, M., R. Wolfe, D. Solomon, F. Patt, J. Blanchette, A. Fleig, and E. Masuoka (1997), MODIS level 1A Earth Location, *MODIS Algorithm Theoretical Basis Document, V3*, available at http://modis.gsfc.nasa.gov/data/atbd/.

O'Hirok W., and C. Gautier (1998), A three-dimensional radiative transfer model to investigate the solar radiation within a cloudy atmosphere. Part I: Spatial effects, *J. Atmos. Sci.,* **55**, 2162–2179.

Ohring, G., B. A. Wielicki, R. Spencer, B. Emery, R. Datla (2005), Satellite Instrument Calibration for Measuring Global Climate Change: Report of a Workshop, *Bull. Amer. Met. Soc*., **86**, 1303-1313.

Oreopoulos, L. and Cahalan, R. F. (2005). Cloud inhomogeneity from MODIS, *J. Clim.*, **18**, 5,110– 5,124.

Oreopoulos, L., R. Cahalan, and S. Platnick (2007), The plane-parallel albedo bias of liquid clouds from MODIS observations, *J. Clim.*, **20**, 5114–5125.

Oreopoulos, L., and S. Platnick (2008), Radiative susceptibility of cloudy atmospheres to droplet number perturbations: 2. Global analysis from MODIS, *J. Geophys. Res.,* **113**, D14S21, doi:10.1029/2007JD009655.

Platnick, S., M. D., King, S. A., Ackerman, W. P. Menzel, B. A. Baum, J. C. Riedi, and R. A., Frey (2003), The MODIS cloud products: algorithms and examples from Terra, *IEEE Trans. Geosci. Remote Sens.*, **41** (2), 459 – 473.

Platnick, S., R. Pincus, B. Wind, M. D. King, M. Gray, and P. Hubanks (2005), An initial analysis of the pixel-level uncertainties in global MODIS cloud optical thickness and effective particle size retrievals, *SPIE Proc.,* **5652**(2), 1 – 12.

Platnick, S., and L. Oreopoulos (2008), Radiative susceptibility of cloudy atmospheres to droplet number perturbations: 1. Theoretical analysis and examples from MODIS, *J. Geophys. Res.,* **113,** D14S20, doi:10.1029/2007JD009654.

Potter, G. L., and R. D. Cess (2004), Testing the impact of clouds on the radiation budgets of 19 atmospheric general circulation models, *J. Geophys. Res*., **109**, D02106, doi:10.1029/2003JD004018.

Ramanathan, V., R. D. Cess, E. F. Harrison, P. Minnis, B. R. Barkstrom, E. Ahmad, and D. Hartmann (1989), Cloud-radiative forcing and climate:Results from the Earth Radiation Budget Experiment*, Science,* **243.**

Rossow, W.B., B. Cairns (1995), Monitoring changes of clouds, *Clim. Change.* **31**, 305-

347.

Rossow, W. B., and Y.-C. Zhang (1995), Calculation of surface and top of atmosphere radiative fluxes from physical quantities based on ISCCP data sets 2. Validation and first results, *J. Geophys. Res.,* **100**(D1), 1167–1197.

Rossow, W. B., and R. A. Schiffer (1999), Advances in understanding clouds from ISCCP, *Bull. Am. Meteorol. Soc*., ***11*****,** 2261–2288.

Rossow, W. B., C. Delo, and B. Cairns (2002), Implications of the observed mesoscale variations of clouds for the Earth's radiation budget, *J. Clim.,* **15**, 557 – 585.

Schiffer, R.A., and W.B. Rossow, 1985: ISCCP global radiance data set: A new resource for climate research, *Bull. Amer. Meteorol. Soc.*, **66**, 1498-1505, doi:10.1175/1520-0477(1985)066<1498:IGRDSA>2.0.CO;2.

Seiz, G., R. Davies, and A. Grun (2007), Stereo cloud-top height retrieval with ASTER and MISR, *Int. J. Remote Sens.,* **27**(9–10), 1839–1853.

Sellers, P. J., et al. (1997), Modeling the exchanges of energy, water and carbon between continents and the atmosphere, *Science,* **275**, 502– 509.

Stevens, B., C.-H. Moeng, and P. P. Sullivan (1999), Large-eddy simulation of radiatively driven convection: Sensitivities to the representation of small scales, *J. Atmos. Sci.,* **56,** 3963– 3984.

Solomon, S., et al. (2007), *Climate Change 2007: The Physical Science Basis,* Cambridge University Press, 996 pp.

Stephens, G. L., et al. (2002), The CloudSat mission and the A-train: A new dimension of space-based observations of clouds and precipitation, *Bull. Amer. Meteor. Soc***.,** **83,** 1771–1790.

Twomey, S. (1991), Aerosols, clouds, and radiation, *Atmos. Environ.,* **254,**2435– 2442.

U.S. Geological Survey, National Mapping Division (1993), GCTP General Cartographic Transformation Package Software Documentation.

Várnai, T. (2000), Influence of three-dimensional radiative effects on the spatial distribution of shortwave cloud reflection, *J. Atmos. Sci.,* **57**, 216– 229.

Várnai, T., and R. Davies (1999), effects of cloud heterogeneities on shortwave radiation: comparison of cloud-top variability and internal heterogeneity, *J. Atmos. Sci*., **56**, 4206-4224.

Várnai, T., and A. Marshak (2001), Statistical analysis of the uncertainties in cloud optical depth retrievals caused by three-dimensional radiative effects, *J. Atmos. Sci.,* **58**, 1540– 1548.

Várnai, T., and A. Marshak (2003), A method for analyzing how various parts of clouds influence each other's brightness, *J. Geophys. Res.,* **108**(D22), 4706, doi:10.1029/2003JD003561.

Várnai, T., and A. Marshak (2007), view angle dependence of cloud optical thicknesses retrieved by Moderate Resolution Imaging Spectroradiometer (MODIS), *J. Geophys. Res.*, **112,** D06203, doi: 10.1029/2005JD06912.

Wang, X. and J.R. Key (2003), Recent trends in Arctic surface, cloud, and radiation properties from space, *Science,* **299***,* 1725-1728.

Warren, S.G., J. C. Hahn, R Eastman and I. G. Rigor (2006), Climatic atlas of clouds over land and ocean, *http://www.atmos.washington.edu/CloudMap/,* Department of Atmospheric Sciences, University of Washington, Seattle.

Welch, R. M., and B. A. Wielicki (1984), Stratocumulus cloud field reflected fluxes: The effect of cloud shape, *J. Atmos. Sci.,* **41**, 3085–3103.

Zinner, T., and B. Mayer (2006), Remote sensing of stratocumulus clouds: Uncertainties and biases due to inhomogeneity, *J. Geophys. Res.,* **111**, D14209, doi:10.1029/2005JD006955.

Zinner, T., B. Mayer, and M. Schröder (2006), Determination of three dimensional cloud structures from high-resolution radiance data, *J. Geophys. Res.,* **111,** D08204, doi:10.1029/2005JD006062.

Zuidema, P., and K. F. Evans (1998), On the validity of the independent pixel approximation for boundary layer clouds observed during ASTEX, *J. Geophys. Res.,* **103**, 6059–6074.

Zhao, G., and L. Di Girolamo (2004), A cloud fraction versus view angle technique for automatic in-scene evaluation of the MISR cloud mask, *J. Appl. Meteorol.*, **43**, doi:10.1175/1520-0450, 860– 869.

Zhang, Y., W. B. Rossow, A. A. Lacis, V. Oinas, and M. I. Mishchenko (2004), Calculation of radiative fluxes from the surface to top of atmosphere based on ISCCP and other global data sets: Refinements of the radiative transfer model and the input data, *J. Geophys. Res.,* **109**, D19105, doi:10.1029/2003JD004457.

APPENDIX A: CLOUD SPHERICAL ALBEDO CALCULATION

This appendix describes the algorithm for calculating the spectral cloud spherical albedo.

Given that the top-of-atmosphere local albedo or planetary albedo is defined as [*Liou*, 2002]

$$\beta_p(\mu_0) = \frac{m_r}{\mu_0 F_0} = \frac{\int_0^{2\pi}\int_0^1 I\,\mu\,d\,\mu\,d\,\varphi}{\mu_0 F_0} = \frac{1}{\pi}\int_0^{2\pi}\int_0^1 R\,\mu\,d\,\mu\,d\,\varphi\ , \tag{1}$$

the cloud spherical albedo is the solar-angle-weighted mean local albedo, given as:

$$\beta = \frac{\int_0^{2\pi}\int_0^1 \beta_p(\mu_0)\mu_0 d\,\mu_0 d\,\varphi_0}{\int_0^{2\pi}\int_0^1 \mu_0 d\,\mu_0 d\,\varphi_0}, \tag{2}$$

where, m_r is the reflected irradiance (W/m^2), I is the radiance ($W/m^2/sr$), R is the Sun-Earth distance corrected bidirectional reflectance factor, μ_0 and μ are the cosine of and viewing zenith angle, respectively, ϕ is the relative azimuth angle, and F_0 is the solar irradiance (W/m^2). m_r and I are measured at cloud-tops. Equation (2) can be expressed further as

$$\begin{aligned}\beta &= 2\int_0^1 \beta_p(\mu_0)\mu_0 d\mu_0 \\ &= \frac{2}{\pi}\int_0^1\int_0^{2\pi}\int_0^1 R\,\mu\mu_0 d\mu\, d\varphi\, d\mu_0 \\ &= \frac{4}{\pi}\int_0^1\int_0^{\pi}\int_0^1 R\,\mu\mu_0 d\mu\, d\varphi\, d\mu_0\end{aligned} \quad . \tag{3}$$

Note that β is independent of sun-view geometry.

Numerically, the Gaussian quadrature integration method can be used to calculate β from Equation (3). Following this method, the integration between [a, b] for a function $f(x)$ can be approximated by

$$\int_a^b f(x)dx \approx \sum_{i=1}^{n} w_i f(x_i), \tag{4}$$

where, w_i is the weight for $f(x)$ evaluated at x_i. The values of (w_i, x_i) are obtained by calling the algorithm routine *gauleg(x1,x2,x,w,n)* [*Chapter 4, Numerical Receipt in Fortran 77, second edition, by Press et al,* 1992], which returns an array of abscissas, $(x_1, x_2, \ldots, x_n)$ and corresponding weights, $(w_1, w_2, \ldots, w_n)$, for the lower and upper limits of integration, *x1=a* and *x2=b*, and the number of abscissas, *n*. Thus,

$$\beta = \frac{4}{\pi}\int_0^1\int_0^{\pi}\int_0^1 R\,\mu\mu_0 d\mu\, d\varphi\, d\mu_0 = \frac{4}{\pi}\sum_{i=1}^{n}\sum_{j=1}^{m}\sum_{k=1}^{p} w_{\mu i} w_{\mu_0 j} w_{\phi k} R\left(\mu_i, \mu_{0j}, \phi_k\right)\mu_i\mu_{0j}, \tag{5}$$

where, *n, m* and *p* are the number of evaluation points for viewing zenith angle, and relative azimuth angle, respectively. In this study, we set *n*=11, *m*=11 and *p*=20.

The required 866 nm R at the discrete sun-view geometrical bins is calculated from a pair of τ and r_e as follows:

1. A gamma distribution is assumed for the cloud drop size distribution [*Hansen and Travis,* 1974]:

$$n(r) = r^{((1-3*v_{eff})/v_{eff})} e^{-r/(r_e * v_{eff})}, \tag{6}$$

where,

$$r_e = \frac{\int_0^\infty r^3 n(r) dr}{\int_0^\infty r^2 n(r) dr}$$

$$v_{eff} = \frac{1}{G r_e^2} \int_0^\infty (r - r_e)^2 \pi r^2 n(r) dr, \tag{7}$$

$$G = \int_0^\infty \pi r^2 n(r) dr$$

r_e is the effective radius, v_{eff} is the effective variance and G is the geometric cross-section area of particles per unit volume.

2. The phase function of the gamma distribution with r_e and v_{eff} is calculated with the Mie calculation code written by Frank Evans (http://nit.colorado,edu/shdom.html). Modification has been done to the code for handling the gamma distribution. In this study, v_{eff} is set to a constant value v_{eff} =0.1, the same value used in the 1-D radiative transfer model for constructing the MODIS τ-r_e retrieval lookup table.

3. The Legendre coefficients of the phase function is calculated as in Appendix E of *Liou* [2002];

4. DISORT [*Stamnes et al.,* 1988] is used to calculate R at cloud-tops for a cloud over a Lambertian surface with an albedo of 0 as a function of sun-view geometry (μ_0, μ, ϕ) with the τ-value and Legendre coefficients for the cloud drop size gamma distribution with the r_e value. The number of discrete streams is set to 48 to achieve high accuracy.

Because calculating β directly in the way as described above is computationally expensive, it is not feasible to calculate β in this way for a large dataset. In this study, we adopt a lookup-table approach. The offline β for the lookup-table as a function of τ and r_e is calculated with τ-value varying from 0.05 to 120 by 0.05 and r_e-value varying from 1 μm to 120 μm by 1 μm. Thus, given a pair of τ and r_e, β can be inferred from the lookup-table. A polynomial interpolation/extrapolation algorithm is used to infer β with higher accuracy as compared to the faster linear interpolation/extrapolation. The polynomial interpolation/extrapolation algorithm routine can be found in *Chapter 3: Interpolation/extrapolation, Numerical Receipt in Fortran 77, second edition, by Press et al* [1992]. Figure A.1 shows examples of β as a function of τ for four r_e values.

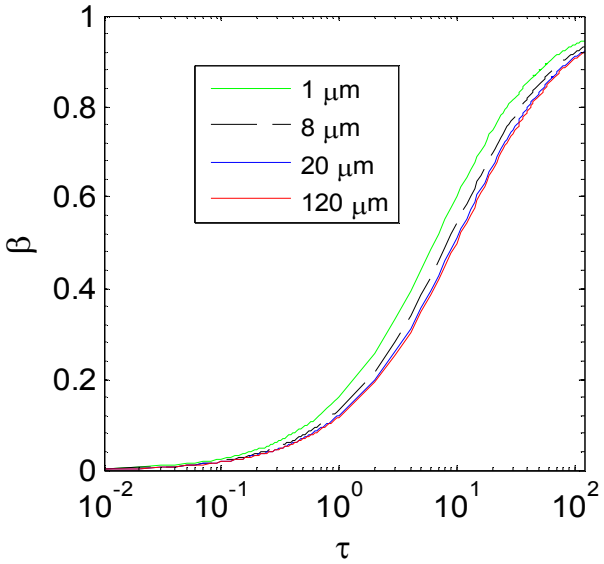

Figure A.1. Plane-parallel spectral cloud spherical albedo (β) at 866 nm as a function of cloud optical thickness (τ) and effective radius (r_e) for four r_e-values of 1 um, 8 um, 20 um and 120 um.

AUTHOR'S BIOGRAPHY

Born in LiangShan, ShanDong Province, China, Lusheng Liang grew up in NingXia Hui Autonomous Region, China. He received his B.S. degree in atmospheric sciences from Nanjing Institute of Meteorology in 1993 and received his M.S. degree in atmospheric sciences from Chinese Academy of Meteorological Sciences in 1999. Before he joined the Department of Atmospheric Sciences of University of Illinois at Urbana-Champaign as a Ph.D. student in 2003, he received a M.S. degree in computer sciences from Southern Polytechnic State University, GA. His Ph. D academic and thesis advisor is Professor Larry Di Girolamo.